MICROGRINDING OF CERAMIC MATERIALS

by

Jie Feng

A dissertation submitted in partial fulfillment
of the requirements for the degree of
Doctor of Philosophy
(Mechanical Engineering)
in The University of Michigan
2010

Doctoral Committee:

Professor Jun Ni, Chair
Professor Yogesh Gianchandani
Professor Xiaoqing Pan
Professor Albert Shih
Associate Professor Bogdan Epureanu

…… to my father, Feng, Jianping and mother, Fan, Zhenmei…….

ACKNOWLEDGEMENTS

It is Professor Jun Ni whom I wish to thank for his guidance and financial support through the course of my graduate studies. Particularly, I appreciate the faith he put in me and my knowledge that made me work enthusiastically hard, if not only, to prove that he did not believe in me in vain. It was through intellectual interactions with him that, now I realize how much, I grew up as an engineer, researcher and a person.

I would like to express my appreciation to Professor Albert Shih for his guidance and help in completing my graduate studies. I would like to thank my dissertation committee members, Prof. Yogesh Gianchandani, Prof. Xiaoqing Pan and Prof. Bogdan Epureanu for their useful comments and guidance.

Especially, I would like to express my appreciation to Dr. Albert Wang, Dr. Bongsuk Kim and Dr. David Stephenson for standing by me in all my attempts in completing my graduate studies and being my perfect role models.

TABLE OF CONTENTS

LIST OF FIGURES

LIST OF TABLES

CHAPTER 1

INTRODUCTION

1.1 Motivation

Micro-components are becoming increasingly important in many advanced industrial fields, because they allow manufacturers to reduce size and weight of their products, facilitate the integration of more functions into the given product size, and help to bridge the gap between macro and nano-world. Ceramic materials are getting more and more popular for micro-components due to their many superior material properties, such as high corrosion resistance, good chemical stability, high hardness and strength. Many engineering ceramics, such as alumina and zirconia, are virtually inert to almost all organic and inorganic chemicals. This makes them ideal materials for many micro-fluidic and medical applications, as they do not interact with, nor contaminate the process media, and chemically stable against most acids and alkalis. In comparison to metals and plastics, ceramic has a much higher hardness and strength. For example, common 99.5% aluminum ceramic is 730% harder than stainless steel. This offers a long-term resistance to both wear and possible cavitations damage. Hence, ceramics are ideally suitable for a wide variety of medical implant applications, from artificial joints to implantable

electronic sensors, stimulators and drug delivery devices. Figure 1-1 shows the wide applications of ceramic materials for miniature components in different areas, including micro-fluidic devices, energy, bio-medical and electronic devices.

(a) Ceramic mini-valves, (MARUWA co., Ltd)

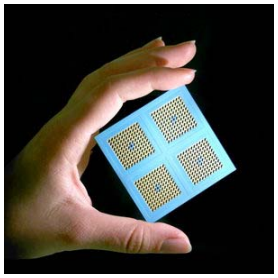

(b) Ceramic micro fuel cell (Fraunhofer IKTS)

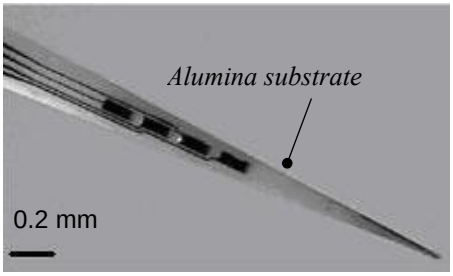

(c) Ceramic neural electrode (Burmeister et al., 2002)

Figure 1-1 Application of ceramic micro-components in different fields

Conventionally, grinding is widely utilized to manufacture ceramic components, as it can provide not only high dimensional accuracy but also superior surface finish. In the past decade, various conventional grinding processes have also been utilized to manufacture ceramic micro-components. As shown in Figure 1-2, Denkena et al. (2004) applied end-grinding to manufacture alumina micro-guideways, and they achieved a 20nm (Ra) surface roughness by applying ultrasonic on the grinding tool. Wu et al. (2006) investigated centerless grinding of micro-shaft (see Figure 1-3), and they successfully solved the vibration issue in clamping micro-components by applying ultrasonic in the workpiece supporter. Ramesh et al. (2004) studied the high speed grinding of micro-grooves with a thin diamond grinding wheel, and they demonstrated that both high material removal rate and superior surface finish (0.1~0.2μm, *Ra*) can be

achieved at same time in grinding ceramic micro-components.

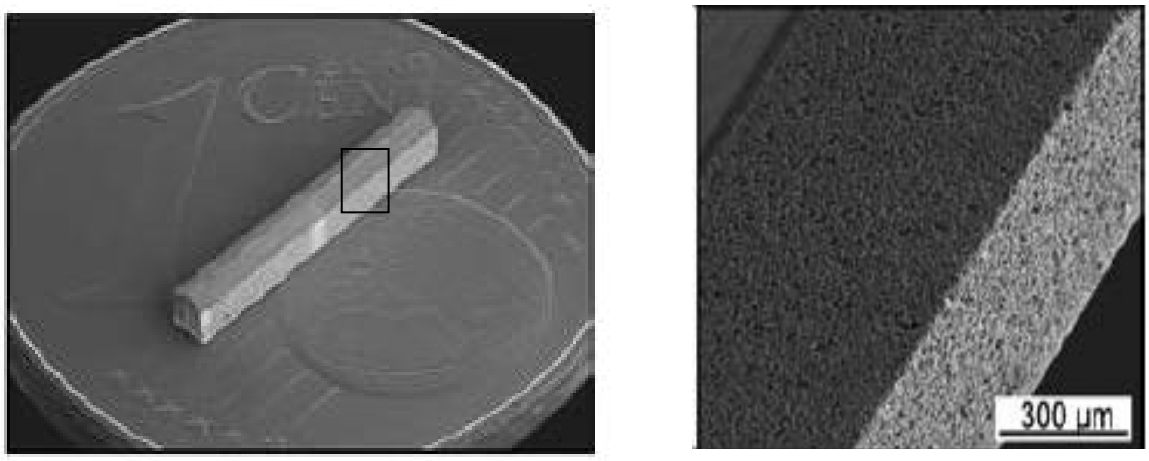

Figure 1-2 Alumina micro-guideways (Denkena et al. 2004)

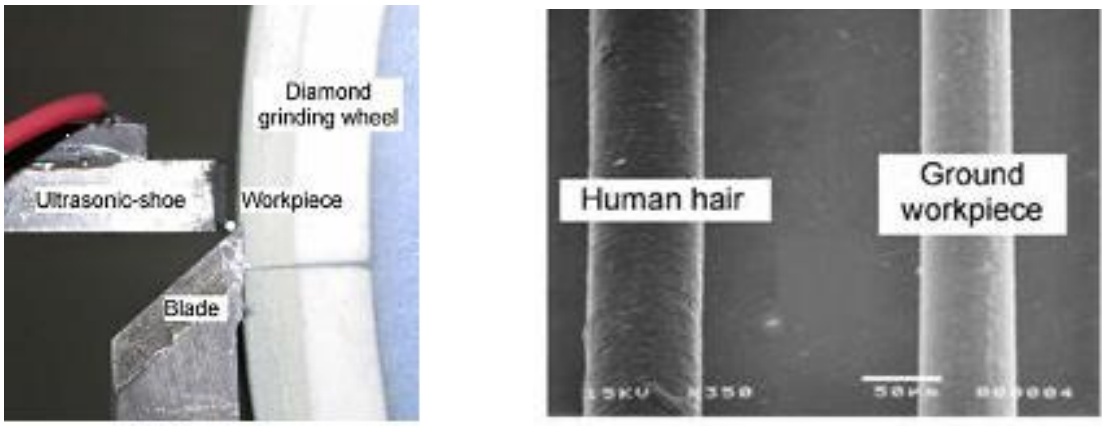

Figure 1-3 Centerless grinding of micro-shaft (Wu et al. 2006)

Although conventional grinding has proven capable of providing high dimension accuracy, high material removal rate and superior surface quality in micro-machining ceramic components, its application is limited to simple micro-features due to the constraint from the large tool size. In order to overcome this challenge, various new

technologies have been proposed to manufacture ceramic micro-components, such as micro-molding, micro-blasting, laser micro-machining, ultrasonic-assisted micro-machining and microgrinding with miniature grinding tools.

Micro-molding is widely used to fabricate bulk shapes of ceramic micro-components, such as micro-valves, micro heat exchangers and micro-catheters. Although this approach is capable of creating ceramic micro-components with complex features, it suffers from the shrinkage and deformation during sintering (Imasu et al., 2006). Subsequent machining is required for manufacturing precision micro-components.

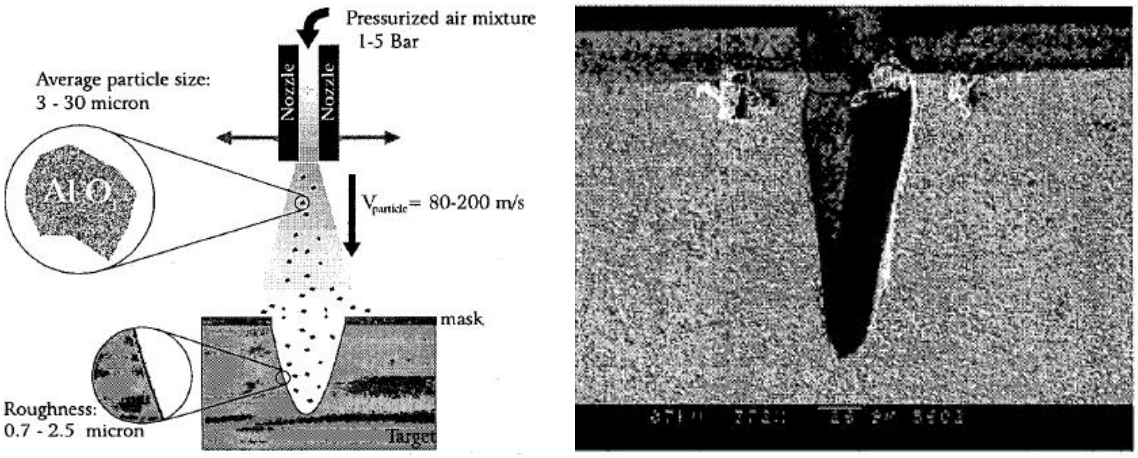

(a) Mechanism of micro-blasting process *(b) Micro-machined glass channels*

Figure 1-4 Micro-blasting of brittle materials (Wensink et al., 2000)

The micro-blasting is an effective way to achieve high material removal rate in micro-machining of ceramic materials (Wensink et al., 2000). By selectively masking the workpiece surface with polymer layers, this process creates micro-geometries by blasting abrasive powders onto the workpiece to achieve material removal, as shown in Figure 1-4.

The major limitation of this approach is the low machining accuracy, since it is difficult to precisely control the shooting direction of the abrasive particles.

The laser micro-machining is also capable of creating complex micro-features on crystal, glass and ceramic materials by applying focused energy impulse (Zeng, et al. 2004). With precision control in the ablation depth (Nikumb et al. 1997), it can achieve high dimensional accuracy in micro-machining. However, as laser micro-machining involves vaporization of ceramic materials during the material removal, it could cause thermal cracking, debris re-deposition and material composition change in the machining process. Hence, it is difficult to achieve high surface quality in laser micro-machining without sacrificing material removal rate (Goller et al., 1997).

To maintain good surface finish at an acceptable material removal rate, the ultrasonic-assisted micro-machining has been developed to manufacture ceramic micro-components (Zhang et al. 2006). As shown in Figure 1-5, this process excites the abrasive partials in the slurry to generate miniature cracks on the ceramic workpiece to achieve material removal. Although it can provide a high material removal rate, due to its fracture dominated material removal mechanism, the ultrasonic-assisted machining tends to create more subsurface damages than grinding (Brinksmeier et al., 1998). This is unacceptable for ceramic micro-components that require high strength and reliability.

To overcome the tool size constrain in conventional grinding, the miniature tool based microgrinding has also been investigated in the past decade. By applying an ultra-high spindle speed (60,000~120,000 rpm), microgrinding has proven capable producing mirror-like surface finish on the micro-molds for manufacturing micro-lens (Chen et al., 2005), as shown in Figure 1-6.

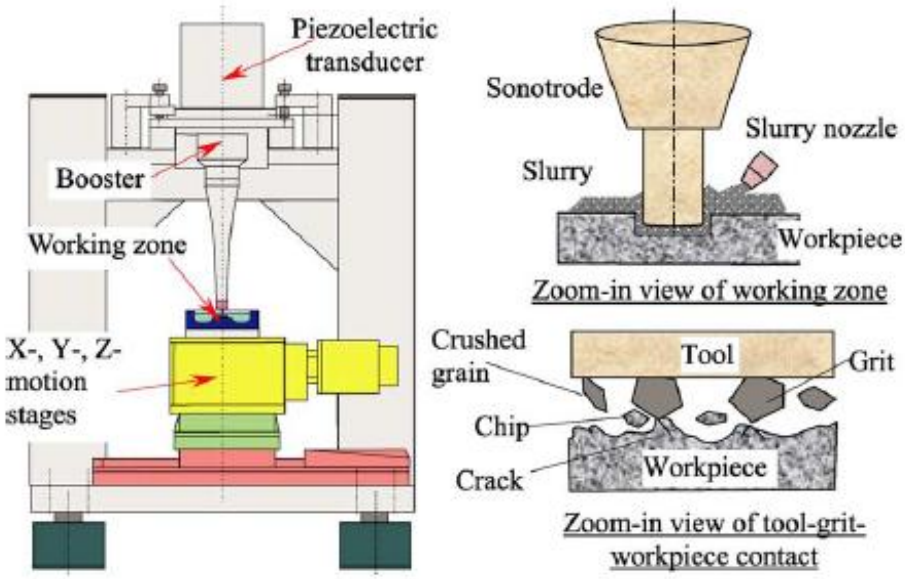

Figure 1-5 Ultrasonic-assisted micro-machining (Zhang et al. 2005)

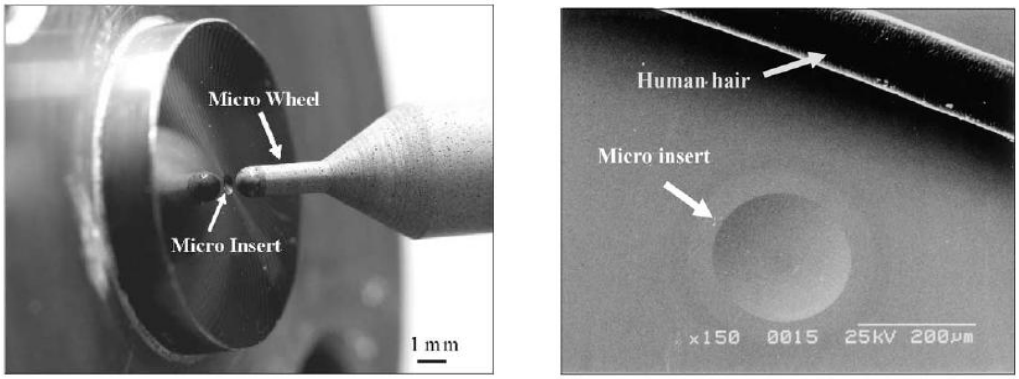

(a) Microgrinding setup *(b) Microground mold insert*

Figure 1-6 Microgrinding of tungsten carbide micro-molds (Chen et al., 2005)

In micro-machining of ceramic dental restorations, the electroplated microgrinding tools were widely used, and it has revolutionized the dental industry in the

past decades by providing rapid machining of various ceramic dental inlays, outlays and bridges with repeatable machining quality. However, in machining high strength engineering ceramic materials, such as alumina and zirconia, the electroplated microgrinding tool will wear out quickly due to diamond pullout, as shown in Figure 1-7. This has hindered the broader applications of microgrinding in industry (Yin et al. 2003, Onikura et al., 2003).

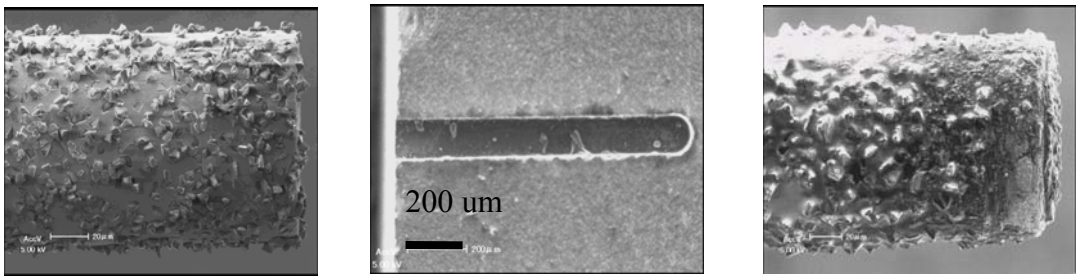

(a) Fresh microgrinding tool *(b) Microground channel* *(c) Tool wear*

Figure 1-7 Microgrinding by the electroplated micro-tool (Onikura et al., 2003)

Given the short tool life in microgrinding of ceramic materials, it is crucial to develop the grinding tool that can last long enough for practical applications. Conventionally, there are four types of grinding tool, based on the different bonding materials, including resin-bonded, electroplated, vitrified bonded and metal-bonded. The resin-bonded grinding tool is relatively soft and less wear resistant. The electroplated grinding tool only has a single layer of diamonds, so its tool life is short in grinding high strength materials. The vitrified bonded grinding tool is more wear resistant, but it is very brittle. Hence, it is difficult to manufacture vitrified bonded microgrinding tool. The

metal-bonded grinding tool is most wear resistance, as it is manufactured by sintering metal powders and diamond abrasive together. Zhang et al. (2000) investigated microgrinding of alumina with the metal-bonded microgrinding tool. It was observed that new diamonds could protrude as the tool wears, and this could significantly improve the tool life in microgrinding. With this advantage, the metal-bonded microgrinding tool is receiving an increasing interest in manufacturing complex micro-feature on high strength ceramic materials, as shown in Figure 1-9.

Therefore, by using the metal-bonded microgrinding tool, short tool life is no long the major concern in micro-machining of ceramic materials. To further promote the application of microgrinding in industrial applications and broaden the knowledge in micro-machining, it is important to find effective ways to predict grinding force for better grinding accuracy, to model the surface generation for better grinding quality and to study the tool wear mechanism for designing proper grinding and tool conditioning process. To achieve these goals, fundamental mechanism studies are needed for microgrinding of ceramic materials including its grinding force modeling, surface generation prediction and tool wear mechanism study.

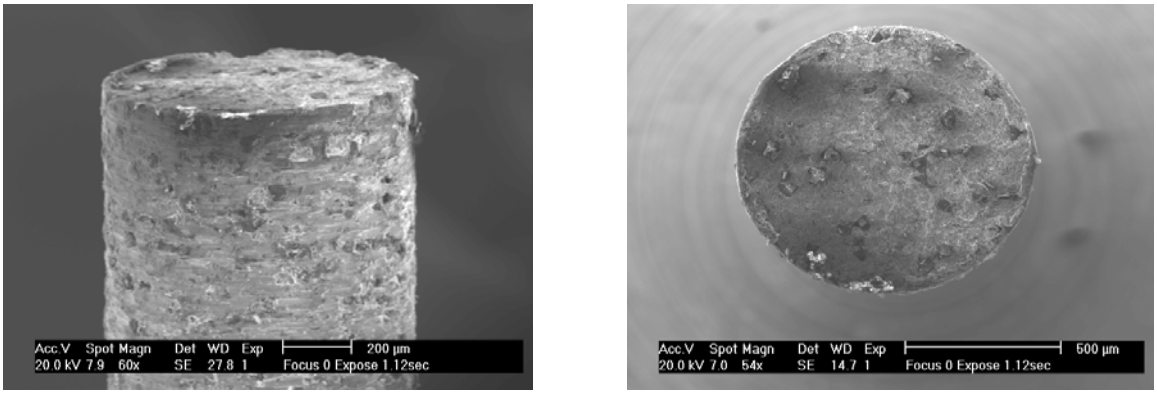

(a) Side view of the tool *(b)Top view of the tool*

Figure 1-8 Sintered metal-bonded microgrinding tool

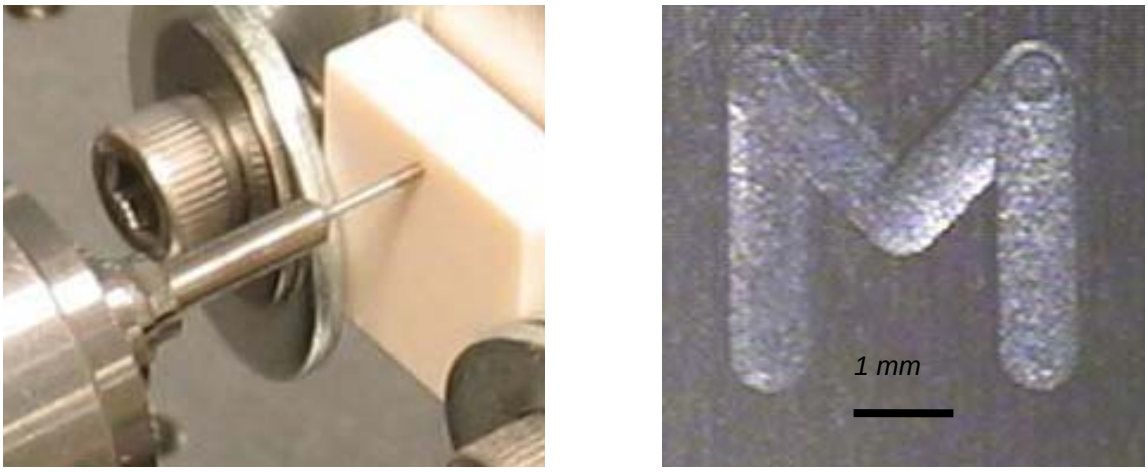

(a) Microgrinding setup *(b) Microground feature on zirconia*

Figure 1-9 Micro-feature machined by the metal-bonded microgrinding tool

1.2 Research Framework and Objectives

The objectives of the proposed research are to understand fundamental issues in microgrinding of ceramic materials with using metal-bonded microgrinding tools, including the grinding force modeling, the surface generation prediction and tool wear

mechanism study. Specific research framework and objectives are discussed in the following.

1.2.1 Force Modeling and Prediction in Microgrinding of Ceramic Materials by Cohesive Zone Based Finite Element Method

The grinding force is always one of the major focuses in the investigation and optimization of a grinding process, as it affects not only tool defection but also the system dynamics. By predicting the grinding force, the corresponding tool defection can be estimated in the grinding process. By compensating this tool deflection in the machining program, the grinding accuracy can be improved. Moreover, a grinding force model is the base for predicting the dynamic stability in the grinding process. With proper modeling of the system dynamics, excessive system vibration can be avoided in the grinding process.

However, an accurate prediction of grinding force is very difficult, as there are numerous irregular abrasive cutting edges on a grinding tool, and it is almost impossible to accurately model their individual chip generation process in the conventional grinding. Moreover, the complex material removal mechanisms in grinding ceramic materials also add the difficulty to grinding force modeling, as it involves both ductile flow and micro-level fracture, which are highly nonlinear processes.

This study aims to model ceramic microgrinding by finite element analysis (FEA). To account for the fracture related material removal mechanism in grinding ceramic materials, a cohesive zone method (CZM) was implemented in the FEA simulation to explicitly model the chip generation process. The miniature size of the microgrinding tool provides a unique opportunity to capture individual diamond cutting edge geometry by

3D interferometer measurement. With this advantage, this study explores the feasibility of accurate force prediction in microgrinding of ceramic materials. Based on the detail diamond profile and the corresponding chip thickness, the CZM based FEA simulation was used to predict peak grinding force in microgrinding alumina. The simulation results were compared with experimental results for the selected diamond on a microgrinding tool at different depths of cut and feed rates. The influence of the tool stiffness on the force prediction was also discussed in this study.

1.2.2 Numerical Modeling of Surface Generation in Microgrinding of Ceramic Materials

The surface finish is one of the key quality indexes in the grinding process. An accurate prediction of surface generation can provide useful guidance for selecting proper grinding conditions for effective materials removal. For example, in grinding ceramic materials, an aggressive grinding condition can be first applied for bulk material removal; in the final finish stage, calculated grinding parameters can be applied to achieve the desired surface finish. The flexibility and reliability in applying this grinding condition combination is built upon the capability to predict surface generation from grinding parameters.

However, surface generation is very complicated in grinding ceramic materials, which involves both surface chipping and ductile material flow. This study aims to investigate the surface generation in microgrinding of ceramic materials. Based on the experimental observations, we developed an analytical method to predict the overall surface generation in ceramic microgrinding by modeling both ductile material removal

and micro-level fracture. The surface generation from ductile material removal was simulated by the trajectory analysis based on detail abrasive cutting edge profiles. In the fracture mode grinding, the surface chipping depth was estimated from the fully damaged subsurface depth from FEA simulation. The resultant surface generation was then compared with surface finish measured in the experiment in various grinding conditions.

1.2.3 Tool Wear Mechanisms in Microgrinding of Ceramic Materials

The grinding tool wear affects both grinding force and surface generation in micro-machining of ceramic materials. Hence, it is desirable to understand the detail tool wear mechanisms in microgrinding for designing proper grinding process and tool conditioning operations. Conventionally, the grinding tool wear is mainly evaluated by the tool wear volume loss. The miniature size of the microgrinding tool enables a direct inspection of the tool wear mechanism in micro-machining of ceramic materials.

With this advantage, this study aims to understand the detail tool wear mechanisms of the metal-bonded microgrinding tool in machining ceramic materials. Each diamond on the microgrinding tool was tracked in this study for their wear mechanism. The observed tool wear was compared with the corresponding surface texture in microgrinding for their specific influence. Based on the observed tool wear mechanism in microgrinding, the proper selection of coolant condition is discussed in this study. Due to the low stiffness of the microgrinding tool, the tool deflection is expected to have a significant influence on the process signals in microgrinding high strength ceramic materials. The selection of proper signals for microgrinding tool wear monitoring is also

discussed in this study.

1.3 Dissertation Organization

The remainder of the dissertation is divided into four chapters. Chapter 2 of this thesis investigates grinding force modeling and prediction in microgrinding ceramic materials by the cohesive zone method and finite element analysis. Experiments were performed to understand the characteristics of the microgrinding force. The influence of tool stiffness on the grinding force prediction was discussed. Then, the proposed grinding force prediction method was tested in different grinding conditions for the validation purpose. In chapter 3, the characteristic of the surface generation was investigated in microgrinding of ceramic materials. Based on these observations, a hybrid surface generation model was proposed for microgrinding of ceramic materials, which accounts for both ductile mode grinding and surface chipping effects. In chapter 4, the detail tool wear mechanism was investigated in microgrinding ceramic materials by tracking individual diamond life cycles. The corresponding surface generation and process signal in the tool wear process were analyzed for the tool wear influence. Dissertation summary and contributions of the study are presented in chapter 5.

CHAPTER 2

FORCE MODELING AND PREDICTION IN MICROGRINDING OF CERAMIC MATERIALS BY COHESIVE ZONE BASED FINITE ELEMENT METHOD

2.1 Introduction

In the past decade, the potential of micro-machining of ceramic materials by the metal-bonded microgrinding tool has been recognized. This stems from the fact that this microgrinding process enables a perfect combination of machining flexibility and acceptable tool life in micro-machining of ceramic materials. However, as the application of the metal-bonded microgrinding tool is relatively new, there have been very few existing studies on its material removal mechanism, chip generation process and force prediction. In the conventional grinding, many studies have been done in these areas by experimental and analytical methods (Law et al., 1973, Yoshikawa et al., 1968, Hecker et al., 2003). However, it is questionable to apply this knowledge directly to microgrinding, since the microgrinding tool has a much lower tool stiffness and surface speed. More research efforts are required to model microgrinding process for its unique characteristics.

In this part of study, the unique characteristics in ceramic microgrinding were

investigated by the experiment. Based on these experimental findings, a finite element model, based on the cohesive zone method, is proposed to model peak grinding force in microgrinding of ceramic materials. By capturing the detail cutting edge profile and the corresponding grinding force on individual diamonds, this study explores the feasibility of accurate force prediction in microgrinding of ceramic materials.

2.2 Literature Review

Grinding force, which affects the tool deflection and the system vibration, is crucial for grinding accuracy and surface finish. However, an analytical modeling of grinding force in machining ceramic materials is difficult due to the stochastic nature in grinding tools as well as its complex material removal mechanisms.

The underlying material removal mechanisms in grinding ceramic materials include micro-level fracture, ductile flow and possible pulverization (Marinescu et al., 2000), as shown in Figure 2-1. The micro-level fracture is very common in grinding ceramic materials due to their brittle nature. It is mainly associated with the cracks, which are propagating within grains (Cleavage) or along the grains boundaries (Brittle Intergranular Fracture) (Malkin et al., 1996, Thomas, 2000). The ductile flow of ceramic materials often happens together with the brittle fracture in the plastic region (see Figure2-1) (Malkin et al., 1996). To achieve a ductile flow dominated ceramic machining, submicron depth of cut and high grinding wheel surface speed is required (Zhong, 2003). Some studies interpolated this ductile flow with energy balance between plastic deformation energy and surface energy in ceramic materials (Bifano et al., 1991). When

the grinding depth is below a critical value, the grinding energy is more likely to become plastic deformation energy, and this causes the ductile flow; on the other hand, when the depth of cut is above that critical value, the grinding energy tends to become surface energy and causes crack growth and eventually fracture. Pulverization refers to the forming of a powder layer under the ground surface due to the fracture of grains (Zhang et al., 1994). It often happens when the grinding depth is large. Some study shows that this phenomenon could be related to the Hertzain contact damage, which involves grain twining and model I, II brittle fracture (Licht et al., 2003).

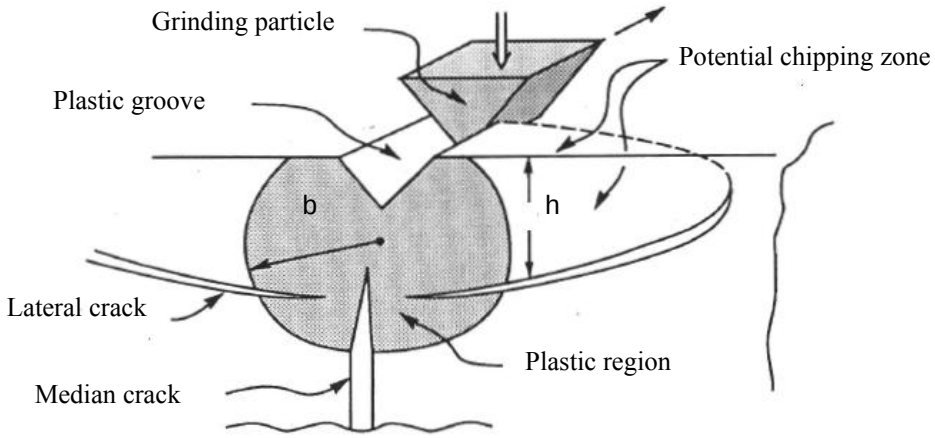

Figure 2-1 Material removal mechanisms in ceramic machining (Malkin et al., 1996)

In conventional grinding, many studies have been done in the force modeling by using different approaches, including friction method, simulation method and empirical method (Li et al., 1980, Tonshoff et al., 1992, Brinksmeier et al., 2006).

The friction method treats the tangential grinding force as friction force (Hakulinen, 1985). The ratio between tangential and normal grinding force is considered

as the friction coefficient. The specific grinding energy, which can be calibrated from the experiments, is needed to calculate the grinding force. This approach has been mainly used to predict average grinding force.

Typical simulation methods for grinding force prediction are kinematics-geometry simulation, Finite element analysis (FEA) and Molecular Dynamics (MD) simulation. The kinematics-geometry method models the grinding force based on the chip geometry and cutting edge trajectory (Malkin, 1989). Its accuracy is relatively low, as it lacks the detail in the actual material removal mechanisms. The FEA simulation has been used to predict subsurface damage in grinding ceramic materials based on continuum damage mechanics (Liu et al., 2002). However, it is unable to model the actual chip generation process in grinding ceramic materials, which involves crack growth, fracture and fragments generation. MD simulation has been used to model the machining of brittle materials, such as silicon (Brinksmeier et al., 2006). However, MD simulation is very computationally expensive, and its modeling scale is usually below 100nm (Brinksmeier et al., 2006). This is much smaller than the scale of a grinding process. To solve this problem, some study combined FEA and MD simulation by using MD simulation for tool-workpiece interaction and FEA for grinding tool system deflection (Ren et al., 2007), but it is still only capable of modeling grinding process with submicron depth of cut.

The empirical methods include statistical regression analysis and artificial neural network (Brinksmeier et al., 2006). Although they are easy to use in practice, they require time-consuming calibration to reduce prediction error, and their accuracy is sensitive to the change in the grinding condition due to their empirical nature.

Therefore, the stochastic nature in the grinding tool as well as the complex

material removal mechanisms make grinding force prediction very difficult in grinding ceramics materials. In order to predict the grinding force from the actual material removal mechanisms, it is necessary to incorporate the fracture related material removal mechanisms in the analysis.

Early studies in fracture mechanics began with the well-known Linear Elastic Fracture Mechanics (LEFM), proposed by Griffith (1920). This approach was improved by Irwin by considering the small plastic deformation effect during fracture process (Irwin 1957, Erdogan, E. 2000). Later, Rice introduced J-integral to calculate energy release rate in fracture (Rice, 1968), and this enabled fracture prediction from the energy perspective. Although these methods are widely used for predicting fracture, they model fracture mainly from a static perspective, and therefore, are more suitable for a "rules based design" than describing micro-mechanisms inherent in fracture. The cohesive zone method (CZM), proposed by Barenblatt (1962), overcame this limitation by assuming there is a micro-level traction region at the edge of cracks, and its traction determines the nucleation, propagation and coalescence of a crack (see Figure 2-2). By implementing CZM in FEA, a fracture process can be explicitly modeled by allowing elements to separate based on grain or sub-grain level material properties. By retaining both mathematical continuity and physical separation, CZM based FEA has been used to model failure of brittle materials under tension, bending and dynamic impacts (Warner et al., 2006, Zavattieri et al., 2001, Camacho et al., 1996). These early studies have proven that CZM based FEA can accurately simulate crack initiation, branching and fragment generation in general fracture process. However, few of these studies have investigated the reaction force on the indenter during fracture, and this is important for modeling the

machining force in grinding ceramic materials.

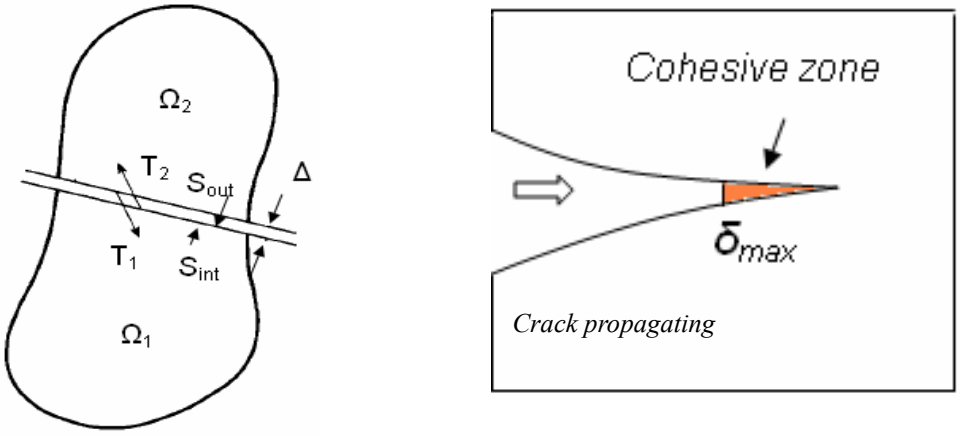

Figure 2-2 Scheme of fracture in cohesive zone method (Camacho et al., 1996)

This study aims to investigate force prediction in microgrinding of ceramic materials by CZM based FEA. The selection of CZM parameters is discussed in the following sections. Based on detail diamond profiles and the corresponding maximum chip thickness, a CZM based FEA model is constructed to simulate material removal in microgrinding of ceramic materials. The predicted grinding force is then compared with experimental results in microgrinding of alumina.

2.3 Cohesive Zone Method Based FEA and Parameter Selection

The traction-separation behavior in CZM is mainly characterized by its cohesive strength (σ), cohesive energy (Γ) and separation displacement (δ) (De Borst et al., 2003).

Common traction-separation profiles are exponential behavior, trapezoid behavior and bilinear behavior (Shet et al., 2004), as shown in Figure 2-3. The exponential behavior has been mainly used to model tensile failure of metallic and bi-metallic materials. The trapezoid behavior is suitable for modeling fracture process that involves yielding, such as failure of elastic-plastic materials. The bilinear model can be considered as a special case of the trapezoid behavior with little yielding behavior. It is often used to model fracture in brittle materials, such as fracture of ceramic materials due to hard impact (Camacho et al., 1996). Hence, in modeling microgrinding of ceramic materials, the bilinear behavior is selected as the traction-separation profile in the CZM based FEA model.

To specify a bilinear traction-separation profile, early researchers utilized cohesive strength (σ_{max}) or equivalent separation displacement (δ_{max}), critical separation displacement (δ_c) and cohesive energy (Γ) derived from different theories. In modeling fracture of alumina under impact, Camacho and Ortiz proposed that maximum cohesive strength could be derived from pre-existing flaws that populate grains (Camacho et al., 1996). This maximum strength, which is also referred as fracture strength (σ_{fr}), can be calculated from fracture toughness (K_{IC}) and collinear cracks of half-width (a_0), stated in Equation (2-1)

$$\sigma_0 = \sigma_{fr} = \frac{K_{IC}}{\sqrt{\pi a_0}} \tag{2-1}$$

Another approach to determine cohesive strength, proposed by Warner and Molinari (2006), is to fit macroscopic material properties from micro-level cohesive

strength. In their study, it was determined that the cohesive strength was around 4.2GPa for Alumina with a tensile strength of 1.4GPa and a compressive strength of 4.4GPa. As this approach requires time consuming numerical calibration, and it is difficult to verify in the experiment, in this study, the pre-existing flaws method is selected to calculate the cohesive strength.

In addition, it is generally believed that for microstructures subjected to multi-axial loading, there exists both tensile displacement and shear slip along grain boundaries. Many early studies assumed that this shear slip was hindered by the micro-level cohesive strength in the shear direction, and it equaled to the cohesive strength in the tensile direction. This assumption is mainly built upon the fact that in conventional scale, ceramic materials seldom exhibit shear failure under normal temperature (Warner et al., 2006, Zavattieri et al., 2001, Camacho et al., 1996). As it is the goal of this study to model micro-level fracture in microgrinding of ceramic materials, the equal shear and tensile cohesive strength assumption is adopted.

To determine the value of tensile and shear cohesive strength, the alumina workpieces are polished by 3μm and 1μm diamond abrasives for 30 minutes in sequence, and then they are inspected for the initial flaw dimension by a microscope after cleaned in ultrasonic bath, as shown in Figure 2-4. The geometry of the initial flaws is measured from six 300x300 μm^2 surface samples by image analyzing software (Image-J). It was observed that average half flaw size was about 6μm. This half crack width is used in this study for calculating the cohesive strength.

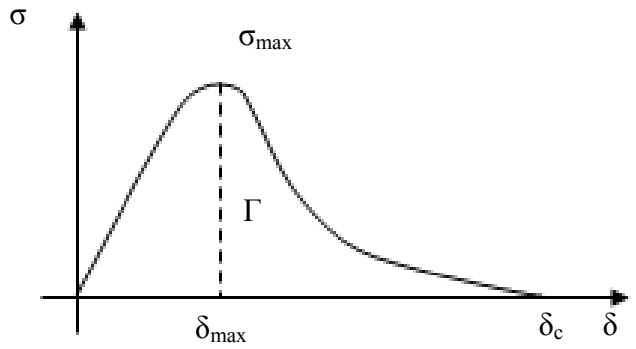

(a) Exponential behavior

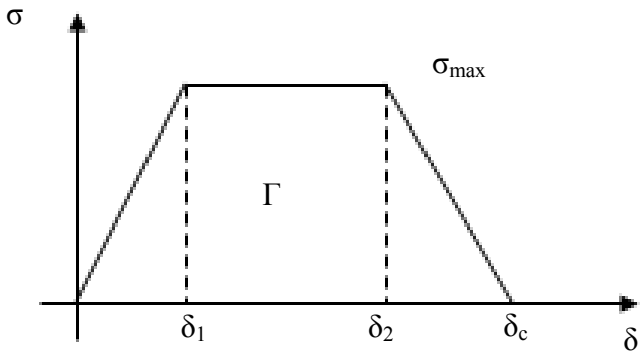

(b) Trapezoid behavior

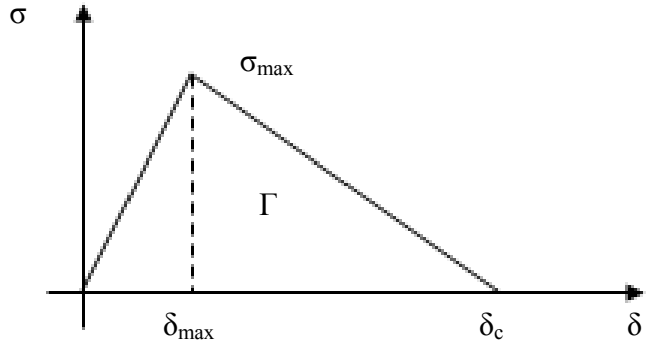

(c) Bilinear behavior

Figure 2-3 Various traction-separation behaviors for CZM (Shet et al., 2004)

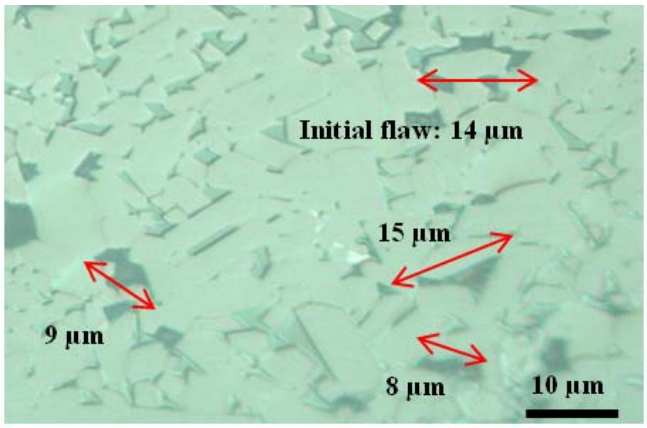

(a) Flaws populate in ceramic workpiece

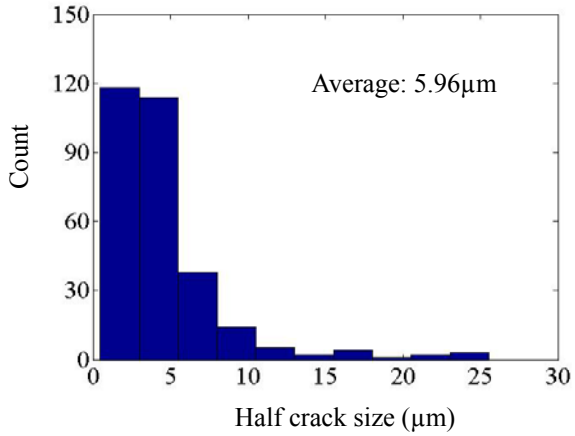

(b) Size of initial flaws

Figure 2-4 Initial flaws population in the ceramic workpiece after flattening

To assess the combined influence of tensile and shear cohesive strength on hindering cracks from propagating, two criteria are usually used: the quadratic separation/strength criterion and the maximum separation/strength criterion (Zavattieri et al., 2001). The quadratic criterion, as shown in Equation (2-2), assesses the resultant separation/strength during fracture process, and it is suitable for modeling crack with complex branching. The maximum criterion, as shown in Equation (2-3) evaluates cohesive strength in every direction separately. This criterion is developed from the

concept that grain boundary shear is controlled by atomic shuffling. The tensile strength of the grain boundary would not necessarily change shear strength, and therefore, they can be modeled independently (Warner et al., 2006). In the early studies, this criterion has been successfully applied in modeling the fracture of ceramic materials under tensile and dynamic impact (Zavattieri et al., 2001, Camacho et al., 1996). As the goal of this study is to model chip generation in microgrinding of ceramic materials, this criterion is also selected in this study.

$$\left(\frac{\sigma_N}{\sigma_{N\max}}\right)^2+\left(\frac{\sigma_S}{\sigma_{S\max}}\right)^2+\left(\frac{\sigma_T}{\sigma_{T\max}}\right)^2=1 \quad \text{or} \quad \left(\frac{\delta_N}{\delta_{N\max}}\right)^2+\left(\frac{\delta_S}{\delta_{S\max}}\right)^2+\left(\frac{\delta_T}{\delta_{T\max}}\right)^2=1 \qquad (2\text{-}2)$$

$$\max\left(\frac{\sigma_N}{\sigma_{N\max}},\frac{\sigma_S}{\sigma_{S\max}},\frac{\sigma_T}{\sigma_{T\max}}\right)=1 \quad \text{or} \quad \max\left(\frac{\delta_N}{\delta_{N\max}},\frac{\delta_S}{\delta_{S\max}},\frac{\delta_T}{\delta_{T\max}}\right)=1 \qquad (2\text{-}3)$$

where σ_N, σ_S, σ_T are the tractions in the tensile, sliding and tearing directions, δ_N, δ_S, δ_T are the equivalent separation; σ_{Nmax}, σ_{Smax}, σ_{Tmax} are the cohesive strength in these directions;, and δ_{Nmax}, δ_{Smax}, δ_{Tmax} are the separation at the maximum cohesive strength.

To fully specify a cohesive behavior, cohesive energy needs to be determined from the analysis of energy dissipation in a fracture process. Physically, fracture is a process during which work from external load is converted into recoverable elastic energy and irrecoverable dissipative energy, assuming the kinematic energy for rigid

body motion is very small and can be neglected (Shet et al., 2004). The irrecoverable dissipative energy can be further classified into plastic dissipated energy and fracture energy, which creates new surfaces, and some other inelastic work. By implementing CZM in this energy analysis, the fracture energy can be considered as the energy dissipated along the cohesive zone, where new surfaces are created. Assuming small plastic deformation, which is valid for most of brittle materials, this cohesive energy can be calculated by the J-integral, which is a path independent integration of strain energy release rate during fracture. The strain energy release rate is the energy dissipated in fracture per unit of newly created surface. In a more general loading case, when Modes I, II and III fracture are involved, the J-integral can be calculated by elastic stress-intensity for opening, sliding and anti-plane mixed fracture (Green, 1998), as shown in Equation (2-4) for plane stress. This provides an easy and reliable way for estimating cohesive energy for ceramic materials.

$$J = \frac{1}{E}(K_I^2 + K_{II}^2) + \frac{1+\nu}{E}K_{III}^2 \tag{2-4}$$

Early studies in applying CZM for modeling fracture of ceramic materials mainly focus on tensile failure. In this case, cohesive energy can be directly estimated from the critical J-integral (J_{IC}), stated by Equation (2-5) for plane stress. When different fracture modes are involved, based on Griffith theory (or the maximum strain energy release rate theory), which states that resistance in material to fracture does not depend on modes

mixity (Suresh, et al., 1991), the total strain energy release rate can be considered the same as the energy in pure mode I fracture (Green, 1998), as stated by Equation (2-6).

$$\Gamma = J_{IC} = \frac{K_{IC}^2}{E} \tag{2-5}$$

$$\Gamma = J_C = \frac{1}{E}(K_I^2 + K_{II}^2) + \frac{1+v}{E} K_{III}^2 = J_{IC} = \frac{K_{IC}^2}{E} \tag{2-6}$$

The initial slope (s) in a CZM profile specifies the elastic reaction to the external load. When bulk elasticity is used, it is desirable to have high initial slope to minimize additional system deformation from cohesive bonding. Most studies suggest that an ideal slope, which balances accuracy and simulation stability, can be calculated from Equation (2-7) based on bulk elasticity (E) and the maximum element size (d) in FEA (Espinosa et al., 2003). This approach is used in our study for the initial slope.

$$s = \frac{10E}{d} \tag{2-7}$$

2.4 Experimental Setup

A meso-scale grinding system is developed to conduct microgrinding, as shown in Figure 2-5. This system consists of four DC motor-driven linear slides, a high speed

electrical spindle for grinding, an electrical spindle for truing, and a mist generating device (COLUBRICATOR, UNIST Inc.). The DC motor-driven linear slides have a maximum load capacity of 133N in the traveling direction. Its positioning resolution is 0.1μm, and its positioning error is within 1μm, calibrated by a laser interferometer. The run out for the grinding spindle and truing spindle is within 1μm. An oil based coolant (Coolube 5500) is sprayed onto the workpiece at 0.198cc/min by the mist generating device during grinding.

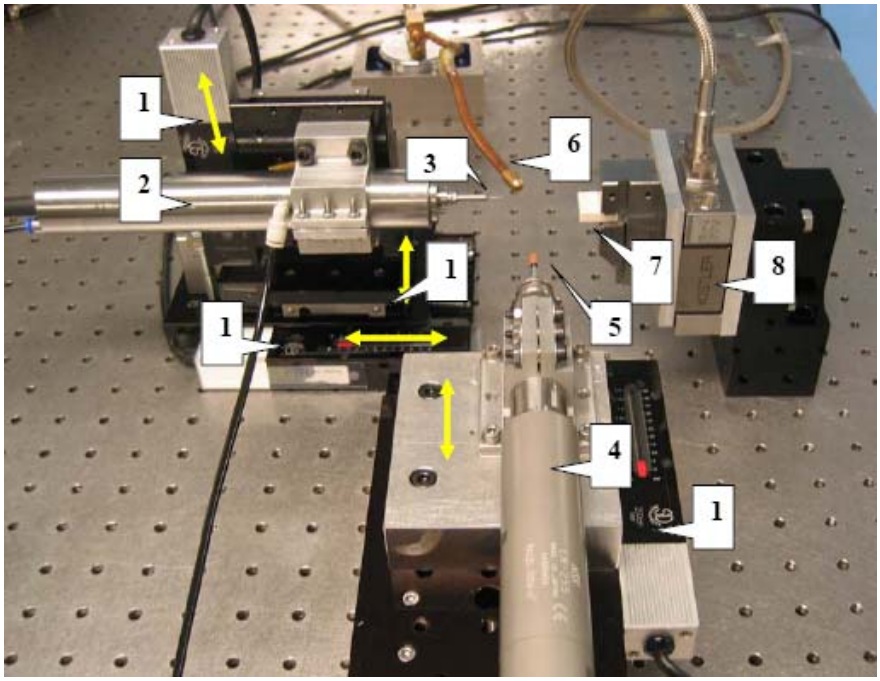

Legend

1. Linear slides
2. Grinding spindle
3. Microgrinding tool
4. Truing spindle
5. Truing wheel
6. Coolant Mist
7. Workpiece
8. Dynamometer

Figure 2-5 Experimental setup for microgrinding force study

A sintered nickel-copper bonded microgrinding tool is used in this study. Its diamond grit is 150, and the diamond concentration is 100. The microgrinding tool was trued to 850μm in diameter by a ∅7.8mm, 120 grit rotary diamond wheel. The spindle

speed for the truing wheel was set at 20,000rpm and the microgrinding tool was running at 20,000rpm during the truing process. Then, the end face of the microgrinding tool was trued when it is running at 5,000rpm to ensure end flatness. During dressing process, the microgrinding tool was dressed by a 220 grit size alumina dressing stick to expose the diamonds. A general purpose Alumina (AD94 from Coorstek) is used as workpiece in this study. Its material properties are summarized in Table 2-1. Before the experiment, the workpiece was flattened by a ∅7.8mm, 120 grit metal-bonded diamond grinding wheel at 70,000rpm.

Table 2-1 Material properties of Alumina (AD94)

Property	
Elastic modulus [GPa]	303
Poisson's ratio	0.21
Density [gm/cc]	3.70
Hardness [GPa]	11.5
Tensile strength [MPa]	139
Fracture toughness K_{IC} [MPa·$m^{1/2}$]	4-5

2.5 Characteristics of Microgrinding

One of the major challenges to predict force in the grinding process is to identify the active diamonds that involve in grinding. For a conventional grinding wheel, as it has numerous diamond cutting edge protrusions, it is difficult to identify the diamonds that contribute to material removal and grinding force. A microgrinding tool, by contrast, provides a unique opportunity for studying grinding force on individual diamonds. As

shown in Figure 2-6, detail geometrical features the diamond cutting edge, such as size and protrusion, can be measured by a white interferometer. The width and protrusion of some selected diamonds (Diamonds 1-6), are summarized in Table 2-2. The width of the diamond is measured by taking SEM pictures. The protrusion of the diamond is identified by line scan of individual diamond by the interferometer. For each interested diamond, line scan is repeated three times for its average protrusion.

Table 2-2 Dimension of diamonds on a 150 grit microgrinding tool

Diamond	Protrusion (μm)	Width (μm)	Spacing Angle (°)
1	6.4±0.2	90	83
2	8.9±0.2	102	39
3	9.0±0.2	90	72
4	5.5±0.9	137	76
5	6.4±0.1	100	45
6	5.6±0.9	90	45

As the purpose of this study is to investigate force prediction in microgrinding of ceramic materials, it is important to capture the grinding force on individual diamond with little interference from each other. Hence, the grinding width is fixed at 150μm, considering that the averaged diamond width is around 90 ~ 140μm, and in this case, only one layer of diamonds will be involved in grinding in radial direction, as shown in Figure 2-7.

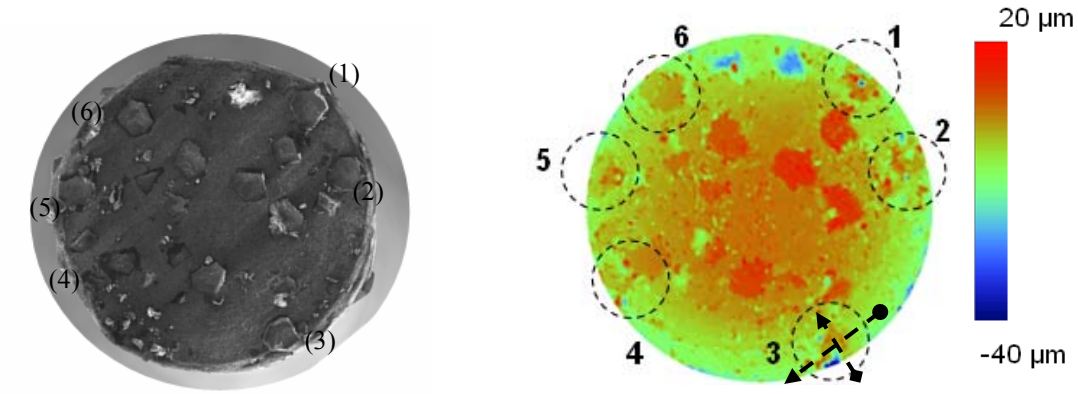

(a) SEM picture of the microgrinding tool *(b) 3D picture of the microgrinding tool*

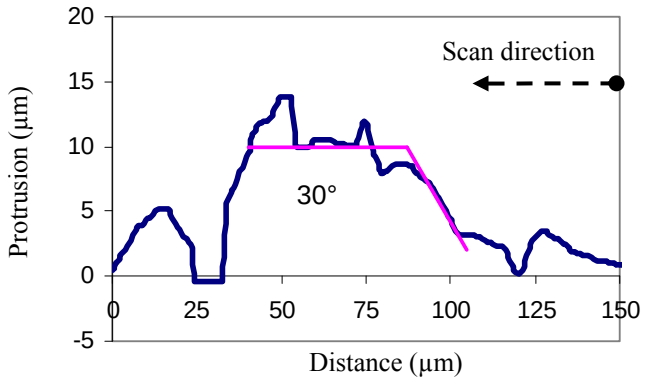

(c) Diamond 3, tangential line scan

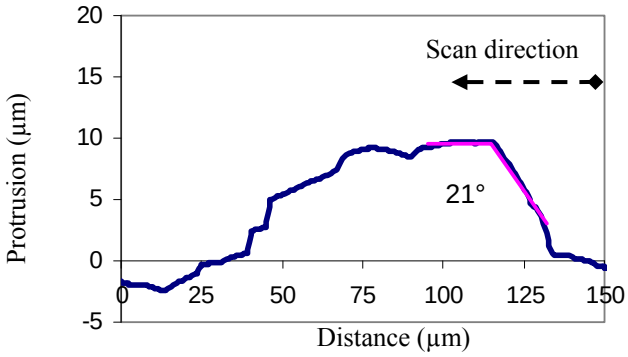

(d) Diamond 3, radial line scan

Figure 2-6 Diamond profile on the microgrinding tool

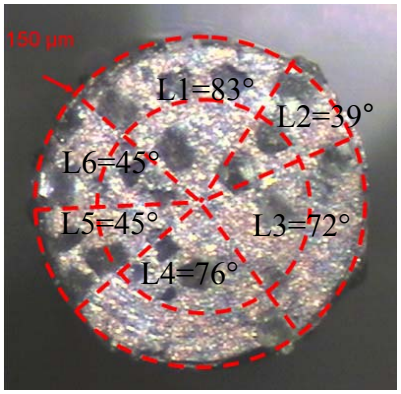

(a) Microgrinding tool and diamond spacing

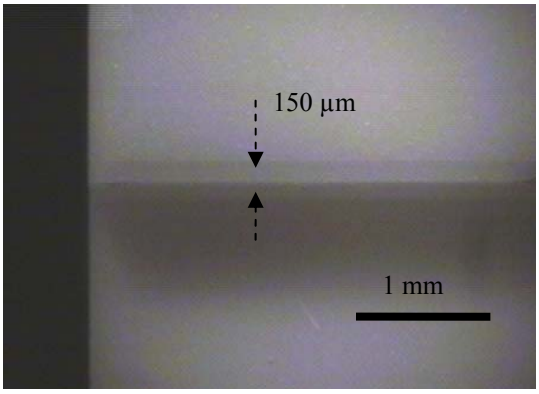

(b) Microground ceramic workpiece

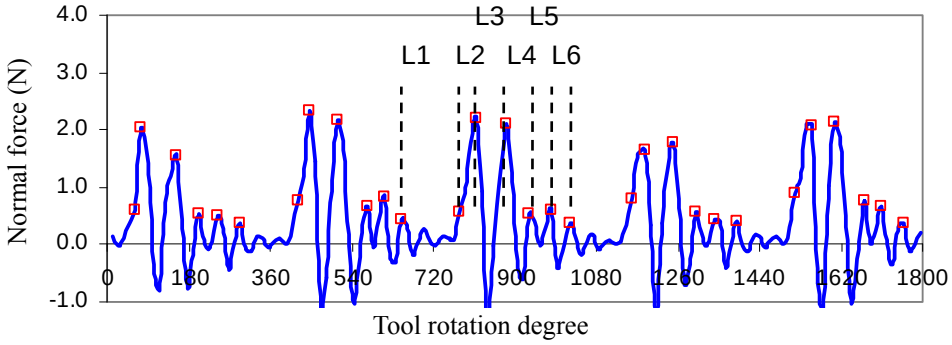

(c) Normal grinding force profile

Figure 2-7 Topography of microgrinding tool and corresponding force peaks

Moreover, by matching force peaks with individual diamond protrusion (Diamonds 1-6, see Table 2-2) and their spacing angles (L1-L6), the force peaks on individual diamond can be identified, as shown in a test conducted at 7µm depth of cut, 20,000rpm spindle speed, 60mm/min feed rate (see Figure 2-7). These force peaks are expected to happen when the maximum chip thickness is reached for individual diamond. Hence, the microgrinding force can be characterized by the force peaks, and by accurate predicting these force peaks, it is possible to construct the overall force profile.

One major difference between microgrinding and conventional grinding lies in the much lower loop stiffness of a microgrinding system. This will result in a much more significant tool deflection during grinding high strength materials, and consequently causes a difference between nominal depth of cut (NDOC) and actual depth of cut (ADOC). To quantify this influence, an experiment is conducted to measure the loop stiffness of the microgrinding machine in normal direction by moving the microgrinding tool against a workpiece mounted on the force sensor, as shown in Figure 2-8. The displacement and force data are captured in this study to calculate the system loop stiffness. Although this test only measures the tool stiffness in the static condition, which could vary when tool is rotating, early study suggests this static stiffness is sufficient for estimating its influence on the grinding force and ADOC (Zhang, 2001). It is found that the microgrinding system loop stiffness in normal direction is about 0.27N/μm. This is much lower than the loop stiffness of conventional grinding machines (20~40N/μm) (Zhang, 2001).

With such low tool stiffness, the tool deflection in microgrinding could be very significant. Hence, in microgrinding, the same rotating microgrinding tool is used to measure the ADOC by probing the ground surface after grinding, and the contacting force is monitored during each probing pass to determine the ADOC. As shown in Figure 2-9, the measured ADOC is proportional to the NDOC. This close to linear correlation is also verified in the study conducted by Zhang (2001) in assessing grinding tool stiffness in end grinding. In addition, Zhang proposed that the correlation between ADOC and NDOC at *i*th path could be calculated based on a time invariant system loop stiffness (K_l) and cutting stiffness (K_W), as shown in Equation (2-8).

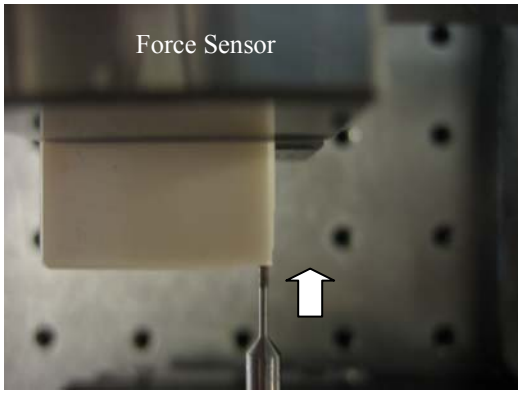

(a) Normal tool stiffness measurement

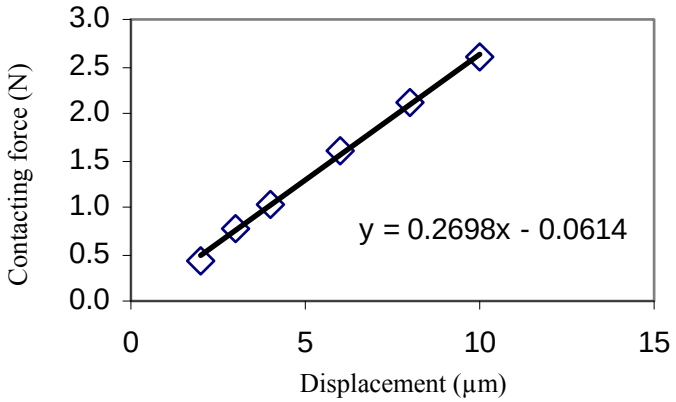

(b) Fitting of normal tool stiffness

Figure 2-8 Measurement of microgrinding tool stiffness in normal direction

$$ADOC = NDOC\left\{1-\left(\frac{k_W}{k_t + k_W}\right)^i\right\} \tag{2-8}$$

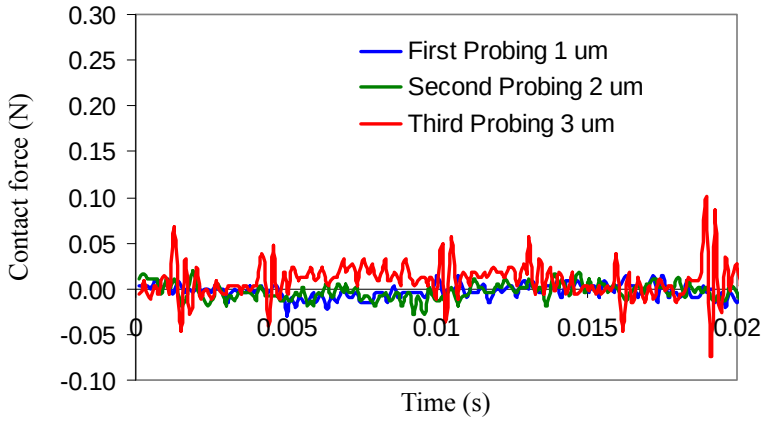

(a) Contacting force during ADOC probing

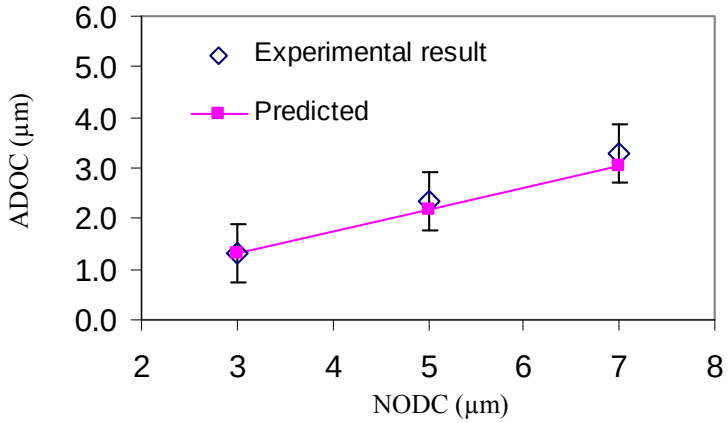

(b) Measured and predicted ADOC

Figure 2-9 Measurement and derivation of ADOC in microgrinding

The measured ADOC and the predicted ADOC, which is calculated from the average ADOC/NDOC ratio (0.43) determined at 3µm NDOC in microgrinding of alumina are compared in Figure 2-9. The small difference suggests that ADOC in microgrinding can be predicted from Equation (2-8) and treated as a derived parameter in modeling ceramic microgrinding.

2.6 Cohesive Zone Method Based FEA at Maximum Chip Thickness

As shown in Figure 2-7, microgrinding force contains periodic peaks. The time intervals between these force peaks are related to the diamond location that can be measured from the microgrinding tool topography. The peak amplitude, by contrast, is related to material removal, tool deflection and tool vibration. In this study, the influence of tool vibration is not considered in force modeling due to the limited understanding of dynamic chip generation in microgrinding. It is generally accepted that machining force reaches peak amplitude at the maximum chip thickness, so it is necessary to calculate these maximum chip thickness (h_m) for individual diamond. A classic maximum grinding chip thickness model, developed by Malkin (1989), is shown in Equation (2-9), based on feed rate (f), width of cut (a), tool rotational speed (w), tool diameter (d_S), diamond spacing angles (L_i) and idealized diamond profiles, as shown in Figure 2-10.

$$h_m = 2s\left(\frac{a}{d_S}\right)^{1/2}\left(1-\frac{a}{d_S}\right)^{1/2} - \frac{s^2}{d_S}, \text{ where } s = \frac{L_i f}{w} \tag{2-9}$$

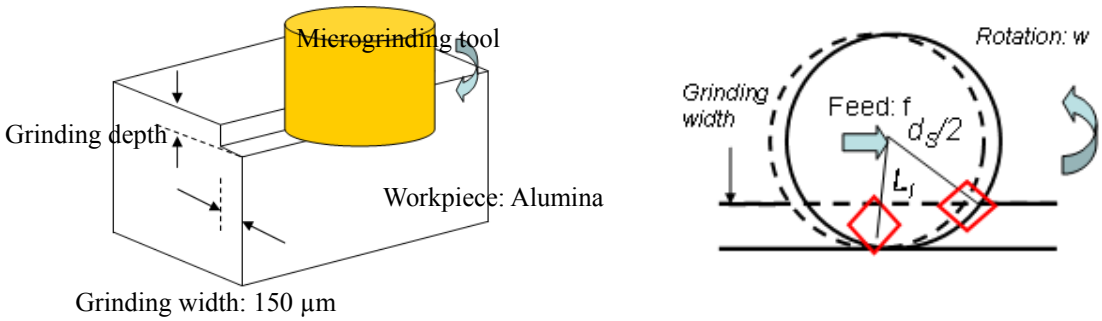

Figure 2-10 Scheme of microgrinding in the experiment

As suggested in Figure 2-6, individual diamonds on a grinding tool have their protrusion, width, side angle and front angle. Their corresponding chip profile can, therefore, be more accurately modeled as a parallelogram considering diamond side angle based on the classic maximum chip thickness model, as shown in Figure 2-11.

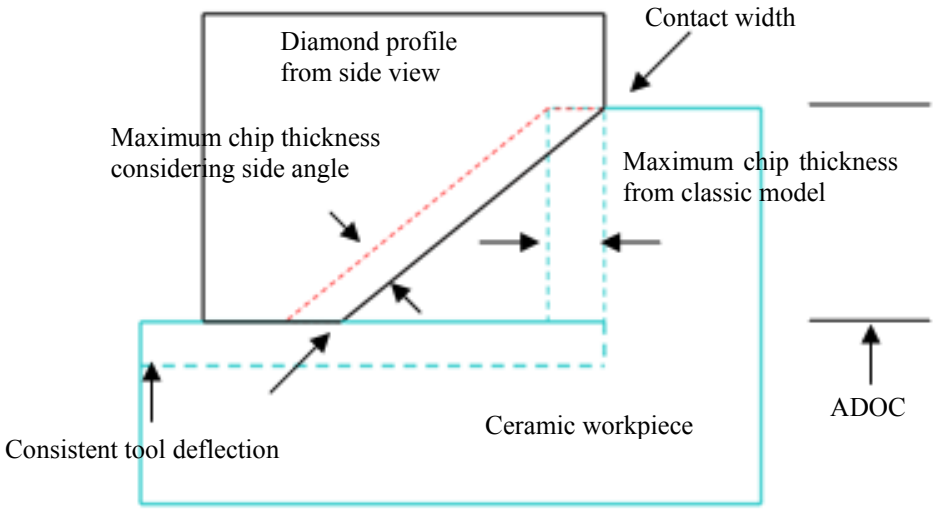

Figure 2-11 Maximum chip thickness profile in microgrinding

Moreover, as a consistent tool deflection was observed in the experiment based on NDOC and measured ADOC, it is reasonable to assume that this tool deflection effect is consistent during grinding and contributes to grinding force. The peak grinding force can, therefore, be considered as a linear combination of tool deflection force and machining force, as stated in Equation (2-10).

$$F_{peak} = F_{grinding} + F_{deflection}$$

$$F_{peak} = F_{grinding} + (NDOC - ADOC)k_l \tag{2-10}$$

The FEA configuration based on the profile of Diamond 3 (see Figure 2-6) is shown in Figure 2-12. The ceramic workpiece is composed of layers of sub-domains with an inclined angle equals to the diamond side angle. The thickness of top layer equals to the maximum chip thickness, and they are bonded to the base materials. The reaction force at bottom is summed for the grinding force. Variation is also applied to the shape of sub-domains to reflect actual chip profile. These variations follow a uniform distribution of half maximum chip thickness. Their CZM properties are calculated based on Equations (2-1, 2-6, 2-7) and workpiece material properties, as summarized in Table 2-3. The CZM based FEA model is implemented in a commercial FEA software ABAQUS. Four nodes linear tetrahedron is selected as the element for meshing sub-domains in ceramic materials, as shown in Figure 2-12(b). The mesh size is set below 0.8μm.

Table 2-3 Summary of CZM parameters

Parameters	
Maximum mesh size [μm]	0.8
Initial stiffness [GPa/mm]	3787500
Half-width of crack [μm]	6
Micro-level Cohesive strength [GPa]	1.04
Maximum displacement [μm]	0.000274
Fracture Energy [J/m^2]	66.8

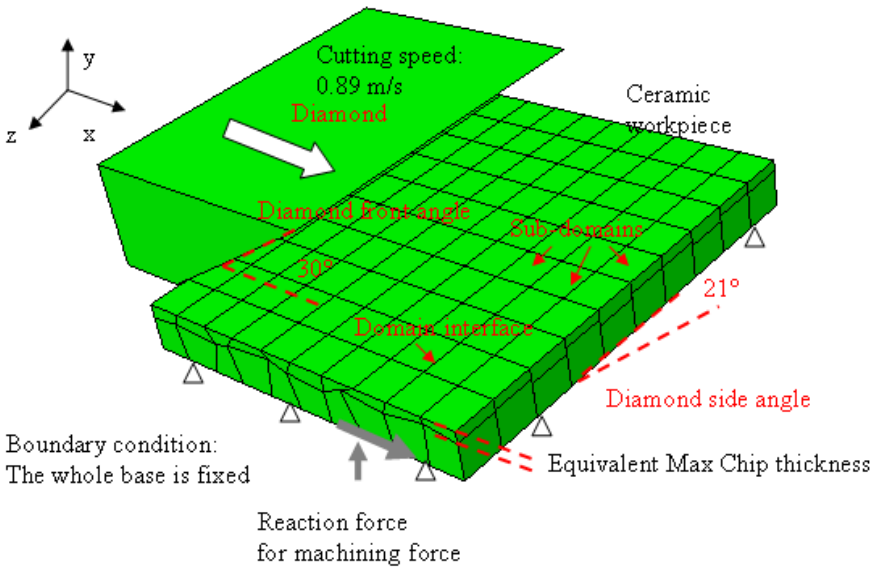

(a) CZM based FEA configuration

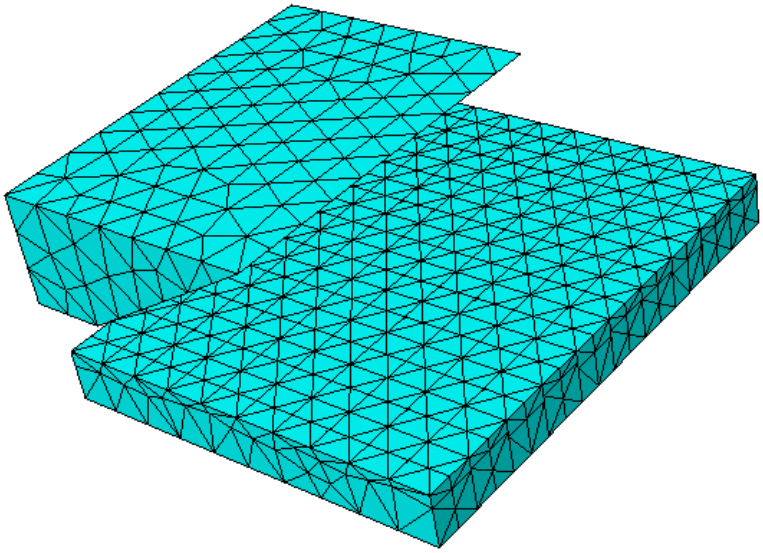

(b) Meshed FEA model

Figure 2-12 CZM based FEA model for single diamond ceramic machining

In order to achieve accurate force prediction from CZM based FEA in microgrinding, it is necessary to determine the proper friction coefficient that reflects the possible adhesion, abrasion and asperity deformation in micro-scale diamond-ceramic contacting. In machining ceramic material, this friction coefficient is usually determined by the tangential-normal force ratio in single diamond grinding (Cai et al., 2002). This experimental approach is also adopted in our study. The peak tangential-normal force ratios on different diamonds (D2 and D3 in Figure 2-6) in different grinding conditions are collected in the microgrinding process. As shown in Figure 2-13, average tangential-normal force ratio is around 0.3. This ratio is used to approximate the friction coefficient in modeling ceramic microgrinding.

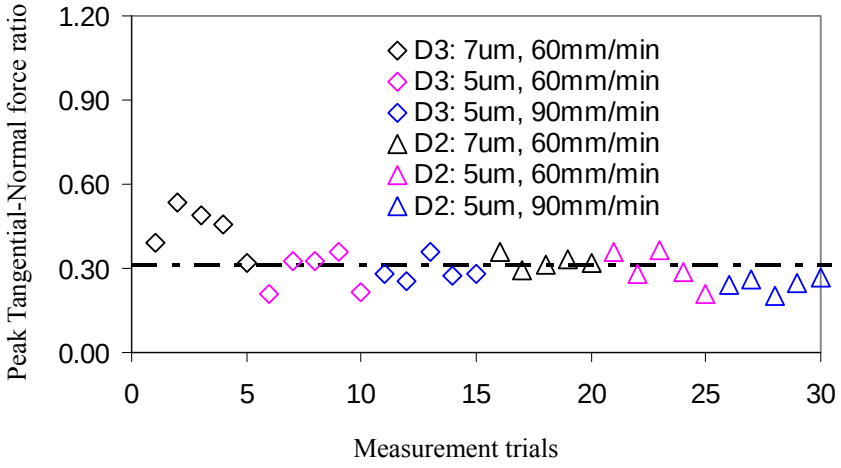

Figure 2-13 Identification of ceramic-diamond contact friction

2.7 Simulation and Experimental Results

The force prediction is conducted for Diamond 3 (see Figure 2-6) in microgrinding of alumina at different NDOC by the CZM based FEA. The machining parameters and the corresponding maximum chip thickness are summarized in Table 2-4.

Table 2-4 Machining parameters for microgrinding of ceramic materials

Parameters	
NDOC [μm]	3, 5, 7
ADOC [μm]	1.3, 2.3, 3.3
Feed rate [mm/min]	60
Tool Radius [μm]	425
Spindle Speed [rpm]	20000
Max Chip thickness [μm]	0.32
Side angle [°]	21
Width of the Chip [μm]	3.7, 6.5, 9.3

The FEA simulations are shown in Figures 2-14, 2-15 and 2-16 for NDOC of 3, 5 and 7μm. The generation of ceramic chips is observed in these simulations, and this represents the material removal due to fracture.

The normal and tangential forces from the base of the ceramic workpiece are collected in the simulation. It is observed that both normal and tangential forces experience an increasing period and then become relatively stable. The average values of their stable regions are used for calculating normal and tangential grinding force. Three FEA simulation trials were performed for each grinding condition, and grinding force results are summarized in Table 2-5. Slightly different simulation force results were observed for a same grinding condition, and this is due to the variation assigned to

individual sub-domains. Their average values are then used to predict the grinding force in normal and tangential directions. The cross section view of cutting process is plotted in Figures 2-14, 2-15 and 2-16. It is observed that peak stress happens on the ceramic chips under the cutting edge. For small NDOC, peak stress is around 150GPa, but it can reach 350GPa for large depth of cut. The peak grinding force is calculated based on the linear combination of machining force from FEA and the tool deflection introduced force based on Equation (2-10), as shown in Table 2-5.

Table 2-5 Summary of normal force results at different depths of cut

NDOC (μm)	Normal force from FEA (N)			Normal force from Deflection (N)	Total normal direction force (N)
	Trial 1	Trial 2	Trial 3		
3	0.21	0.22	0.23	0.45	0.68±0.01
5	0.43	0.39	0.39	0.72	1.17±0.02
7	1.04	0.99	0.96	0.99	2.07±0.04

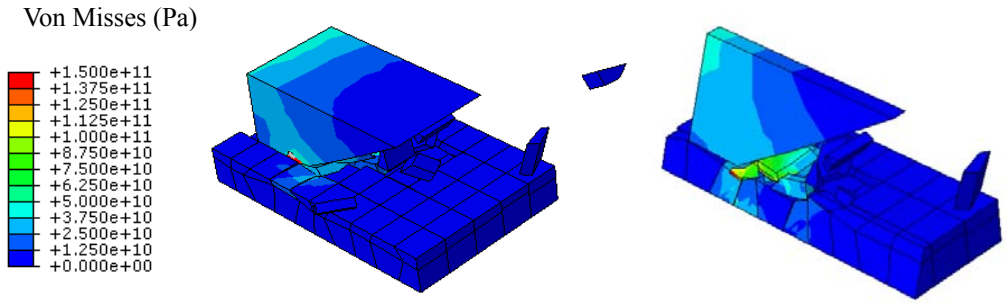

(a) Simulation of cutting process

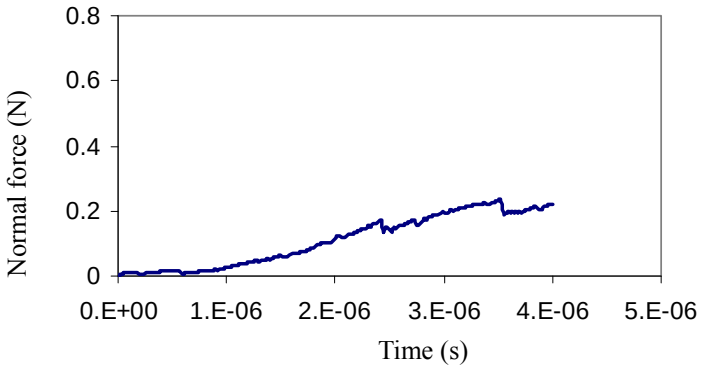

(b) Normal force from simulation

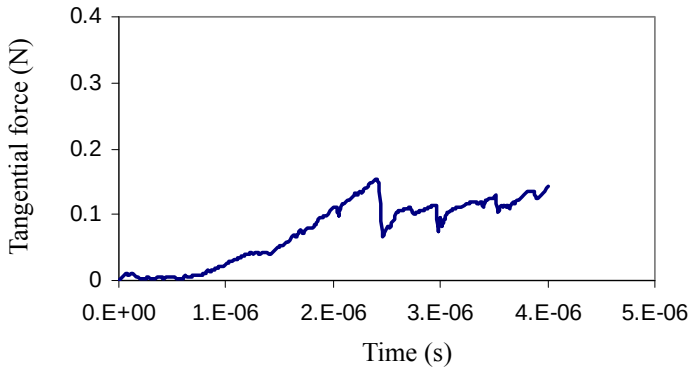

(c) Tangential force from simulation

Figure 2-14 Simulation of ceramic microgrinding at 3µm NDOC, 60mm/min feed rate in Trial 1

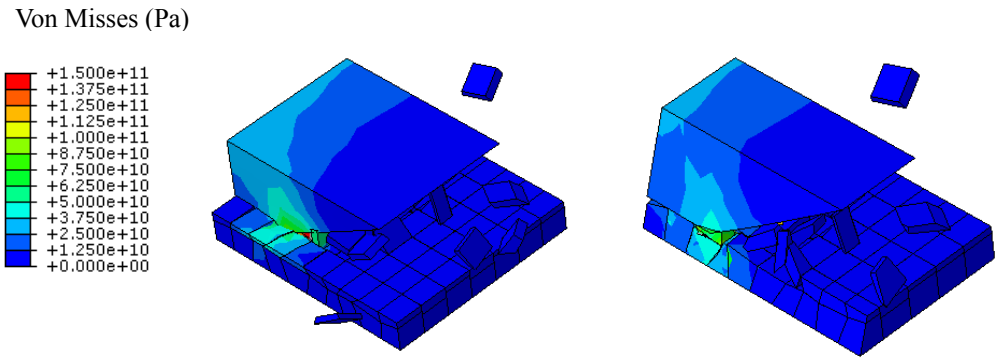

(a) Simulation of cutting process

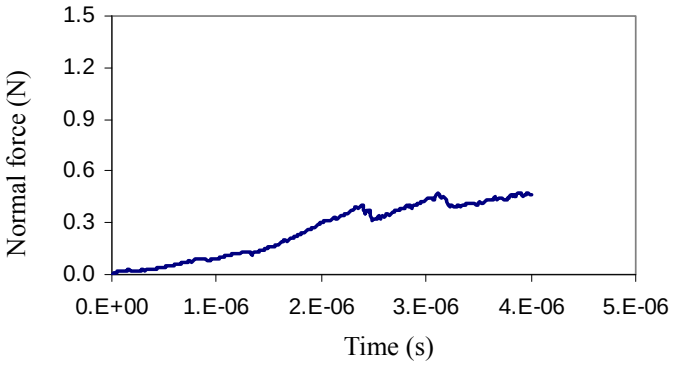

(b) Normal force from simulation

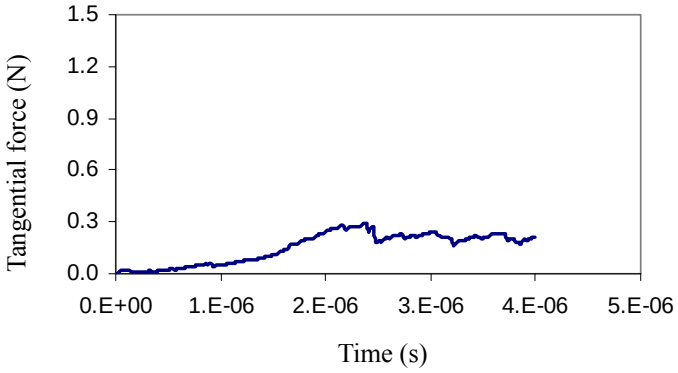

(c) Tangential force from simulation

Figure 2-15 Simulation of ceramic microgrinding at 5µm NDOC, 60mm/min feed rate in Trial 1

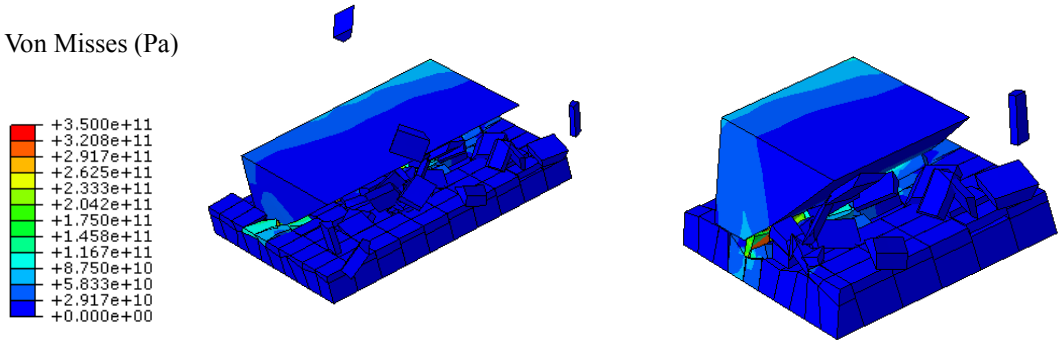

(a) Simulation of cutting process

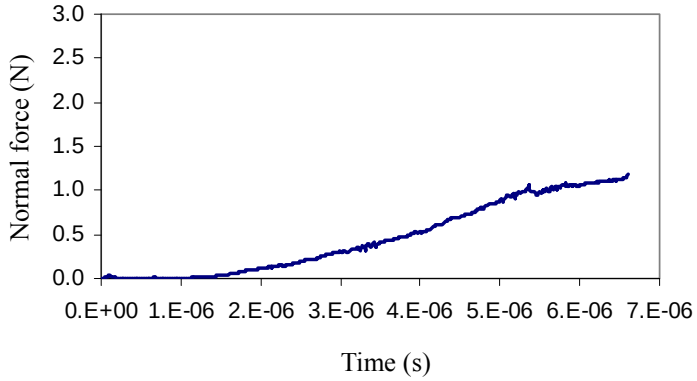

(b) Normal force from simulation

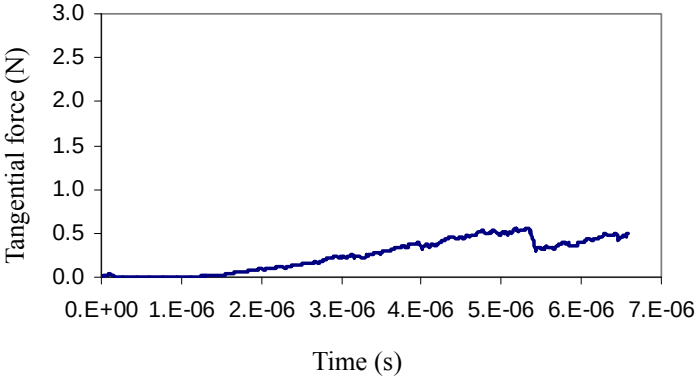

(c) Tangential force from simulation

Figure 2-16 Simulation of ceramic microgrinding at 7µm NDOC, 60mm/min feed rate in Trial 1

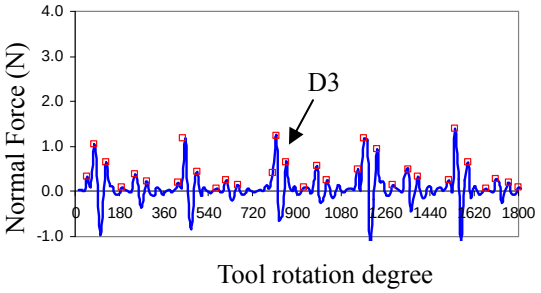

(a) Normal force at 5μm NDOC

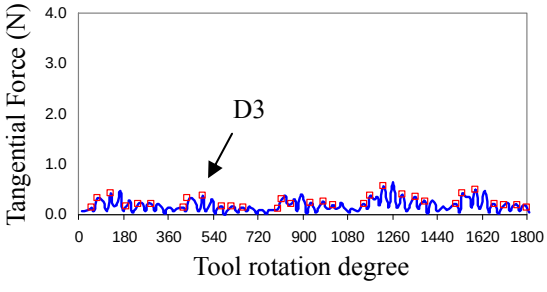

(b) Tangential force at 5μm NDOC

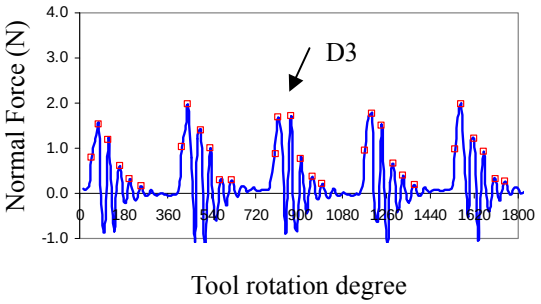

(c) Normal force at 5μm NDOC

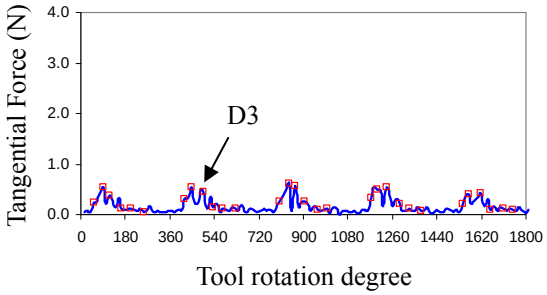

(d) Tangential force at 5μm NDOC

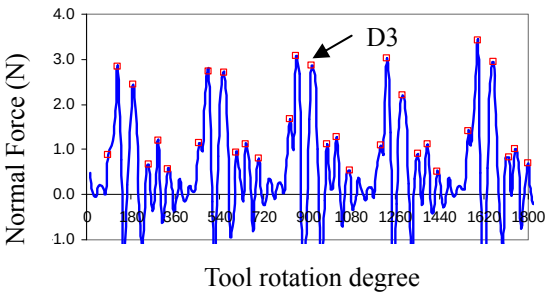

(e) Normal force at 7μm NDOC

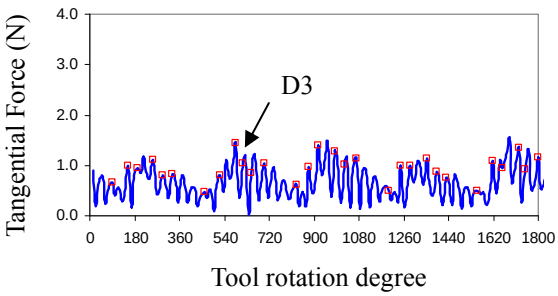

(f) Tangential force at 7μm NDOC

Figure 2-17 Measured grinding force at 60mm/min feed rate at different NDOC

To verify the simulation results, experiments are conducted at different NDOC, as shown in Figures 2-17. The peak force on Diamond 3 is captured based on diamond spacing angle and its protrusion. The averaged peak force of ten tool revolutions is compared with simulation results at different NDOC. As shown in Figure 2-18, the predicted normal force matches well with experimental results. Relative large variation is

observed at large depth of cut. This could be resulted from the increasing tool vibration at large depth of cut.

The predicted tangential grinding force is also compared with experimental results, as shown in Figure 2-18(b). The predicted tangential force follows a similar increasing trend as the experimental results, but there is always an underestimation of tangential force at different NDOC. It is expected that in actual microgrinding process, tool deflection, chipping clogging and other friction related factors have all contributed to tangential force in material removal. However, these factors are not considered in the current CZM based FEA.

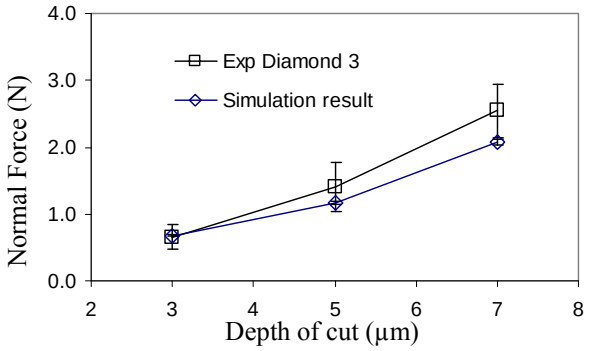

(a) Normal grinding force

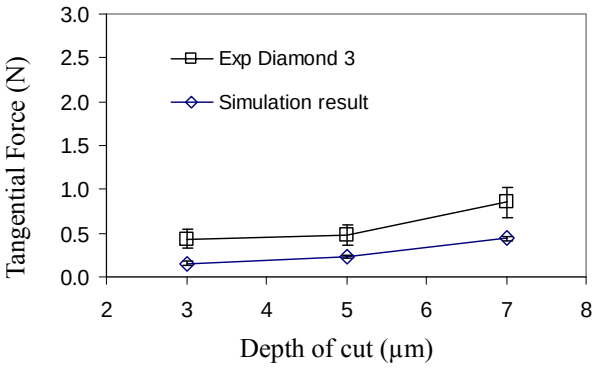

(b) Tangential grinding force

Figure 2-18 Comparison of experimental and simulation results at different NDOC

To further assess the feasibility of force prediction in microgrinding of ceramic materials, the CZM based FEA simulation is conducted at different feed rates for Diamond 3, as summarized in Table 2-6. The ADOC is measured three times in the experiment by probing the rotating tool towards the ground surface, and it is observed that high feed rate reduces the ADOC, but its influence is relatively small. The simulation results are shown in Figures 2-15, 2-19 and 2-20. Higher stress is observed in higher feed rate, which is about 200GPa. The normal grinding force, which consists of force from cutting process and force from tool deflection is calculated in Table 2-7.

Table 2-6 Chip thickness in microgrinding at different feed rates (Diamond 3)

Feed rate (mm/min)	Maximum chip thickness (μm), at 5μm NDOC, 20000rpm	Measured ADOC (μm)
30	0.17	2.3±0.5
60	0.32	2.3±0.5
90	0.49	2.0±0.5

Table 2-7 Summary of normal force results at different feed rates

Feed rate (mm/min)	Normal Force FEA (N)			Normal force deflection (N)	Total normal direction force (N)
	Trial 1	Trial 2	Trial 3		
30	0.15	0.15	0.12	0.72	0.86±0.02
60	0.43	0.39	0.39	0.72	1.12±0.02
90	0.64	0.59	0.66	0.81	1.44±0.04

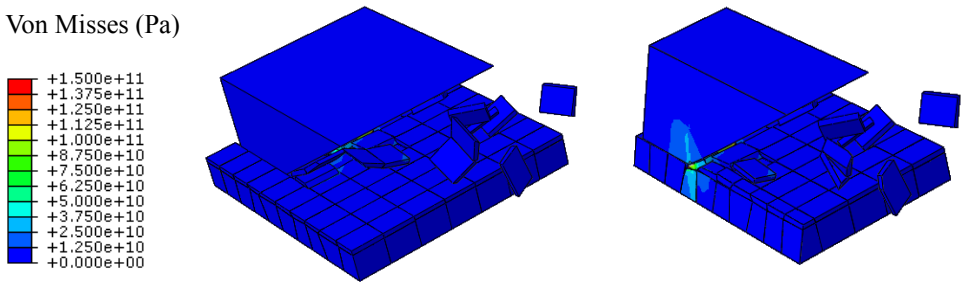

(a) Simulation of cutting process

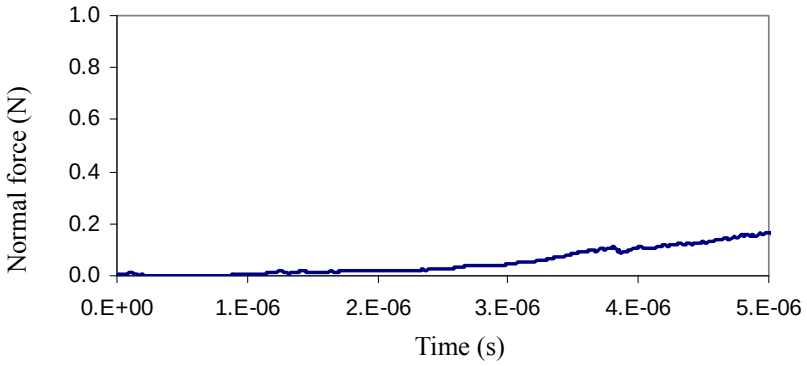

(b) Normal force from simulation

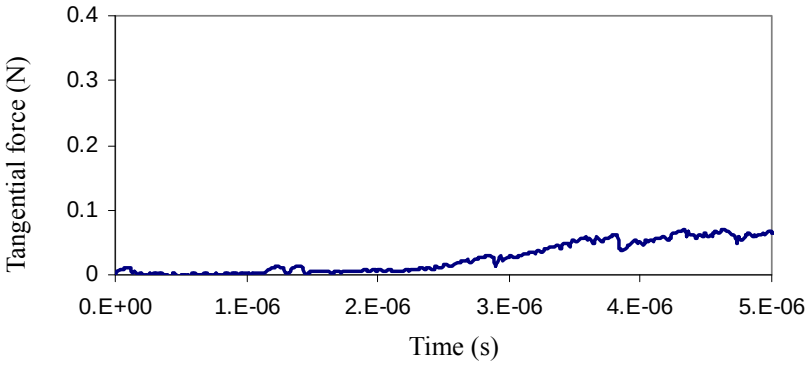

(c) Tangential force from simulation

Figure 2-19 Simulation of ceramic microgrinding at 5µm NDOC, 30mm/min feed rate in Trial 1

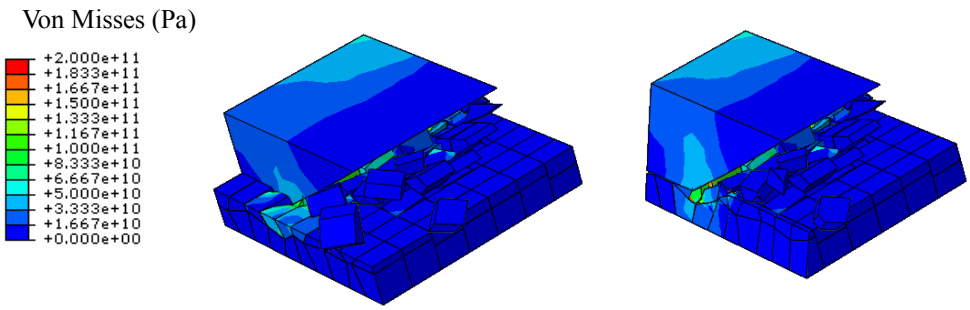

(a) Simulation of cutting process

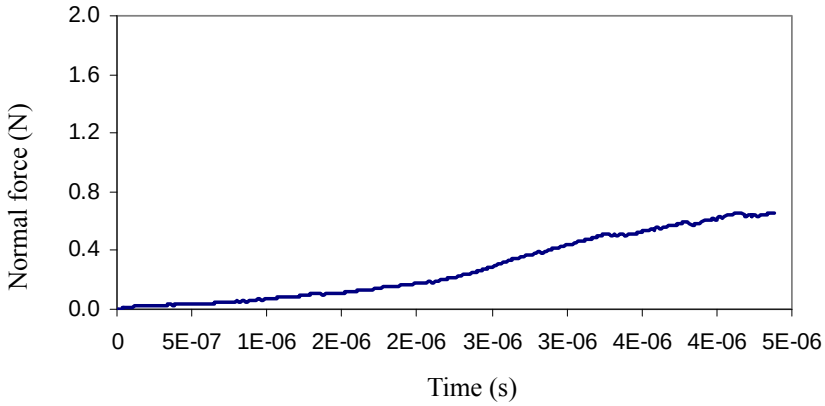

(b) Normal force from simulation

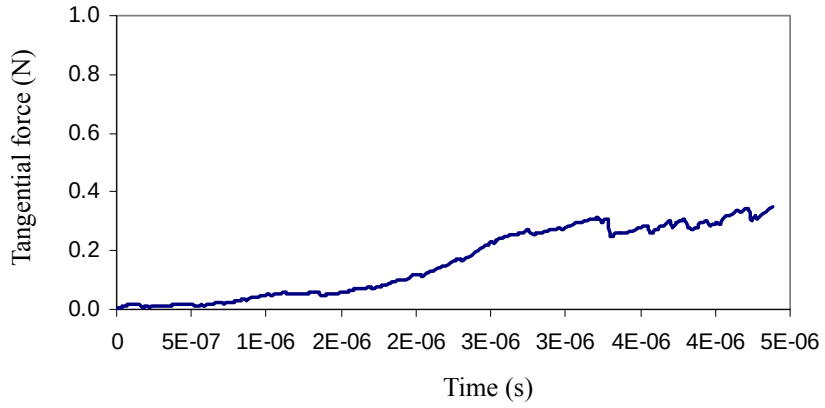

(c) Tangential force from simulation

Figure 2-20 Simulation of ceramic microgrinding at 5µm NDOC, 90mm/min feed rate in Trial 1

The microgrinding experiments are also conducted at different feed rates, as shown in Figure 2-21. Grinding force on Diamond 3 is also collected in this study, and compared with simulation results, as shown in Figure 2-22. It is observed that at small feed rate, the predicted normal grinding force matches well with the experimental results, while at high feed rate, relatively large error is observed. This could also be related to the increasing dynamic effects at high feed rate in experimental results, which has not been considered in the FEA model. In addition, it is observed that for tangential force, the simulation results follow a similar increasing trend as the experimental results. However, in magnitude, simulation results always underestimate tangential force. This could be related to the complex actual diamond-ceramic contacting condition, in which, tool deflection and chips clogging could significantly affect the adhesion and abrasion.

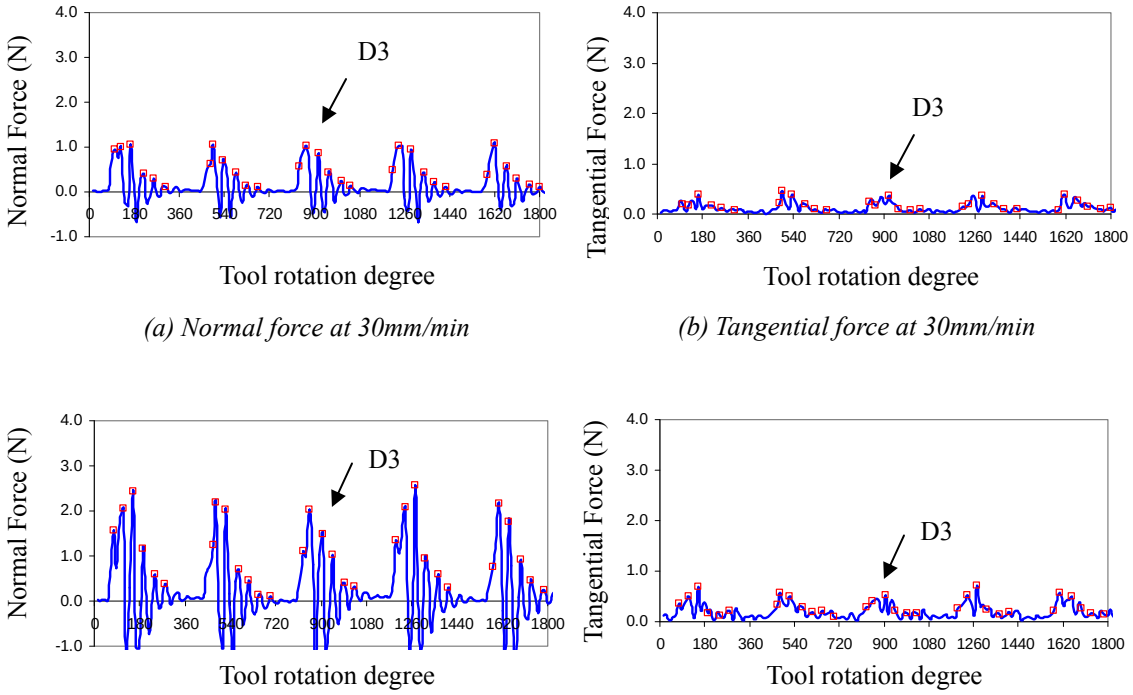

(a) Normal force at 30mm/min

(b) Tangential force at 30mm/min

(c) Normal force at 90mm/min

(d) Tangential force at 90mm/min

Figure 2-21 Measured grinding force at 5µm NDOC at different feed rates

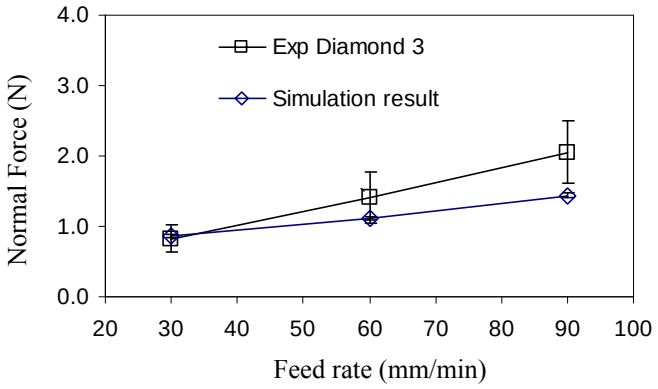

(a) Normal grinding force

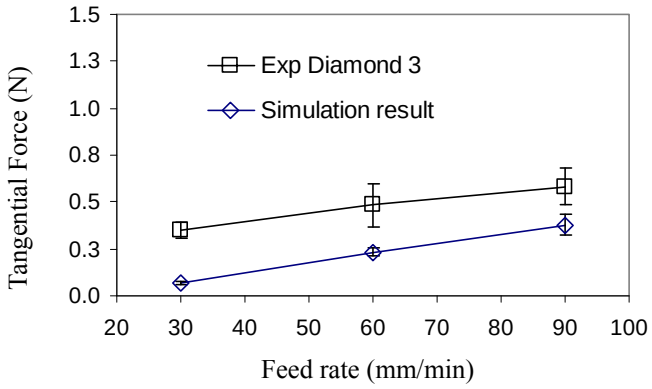

(b) Tangential grinding force

Figure 2-22 Comparison of experimental and simulation results at different feed rates

2.8 Analysis of Prediction Error

As shown in Figures 2-18 and 2-22, the proposed CZM based FEA underestimates tangential force in microgrinding. It is expected that in addition to ceramic cutting, which is modeled by CZM based FEA, tool deflection, chip clogging and process vibration all contribute to the resistance in tangential direction in microgrinding. Based on the measured ADOC in microgrinding, the tool deflection contributes to the normal grinding force in a consistent manner. In tangential direction, it

can be assumed that the tool deflection also increases the friction, as shown in Equation (2-11). The friction coefficient (μ), measured from tangential-normal force ratio (see Figure 2-13), is used to calculate the additional tangential resistance. As shown in Figure 2-23, by considering the friction introduced by both cutting and tool deflection, the error between actual grinding force and calculated tangential grinding force is significantly reduced.

$$F_{\tan\_peak} = F_{\tan\_grinding} + \mu(NDOC - ADOC)k_l \tag{2-11}$$

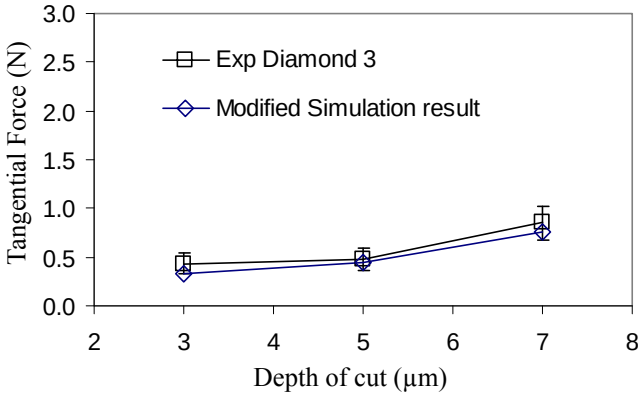

(a) Normal grinding force

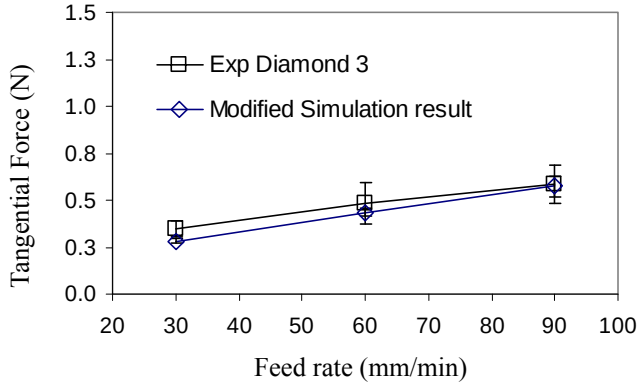

(b) Tangential grinding force

Figure 2-23 Experimental and simulation results with modified friction from tool deflection

2.9 Conclusion

This study investigates force prediction in microgrinding of ceramic materials by CZM based FEA. Based on actual diamond profiles and the corresponding maximum chip profile, a CZM based FEA model is constructed to model grinding force peak in microgrinding of ceramic materials. The effect of tool deflection is also considered in force prediction in microgrinding. The predicted grinding is compared with the experimental measurement at different depths of cut and feed rates. It is observed that the predicted normal force matches well with the experimental results, but there are consistent underestimations in tangential grinding force from pure CZM based FEA simulation. However, these prediction errors can be minimized by considering the kinematic friction introduced by tool deflection effect. In addition, it is observed that the predicted normal force is always smaller than the experimental result at high depth of cut and feed rate. This could be related to the increasing dynamic effect in the experiment. Hence, the proposed CZM based FEA is suitable for predicting force peaks in microgrinding of ceramic materials, and by considering the tool deflection effect, accurate force prediction is feasible.

CHAPTER 3

NUMERICAL MODELING OF SURFACE GENERATION IN MICROGRINDING OF CERAMIC MATERIALS

3.1 Introduction

The surface generation, which is composed of surface integrity, surface texture and roughness, is one of the key indexes in assessing the quality of a ground component. The capability to model surface generation in microgrinding will not only benefit the selection of proper grinding conditions for effective material removal, but also improve the reliability of the ground components by achieving high surface quality. Since microgrinding of ceramic materials is a relatively new process, few existing studies have investigated its surface generation and modeling approach. Many studies have been done in surface roughness prediction in conventional grinding by considering the effect of tool topography, grinding parameters and initial workpiece surface (Tonshoff et al., 1992), but few of them are applicable to microgrinding, due to the difference in tool stiffness, surface speed, system vibration and material removal mechanism. This part of study aims to investigate the characteristics of surface generation in microgrinding of ceramic materials. Based on the experimental observation, this study explores the feasibility of

accurate surface roughness prediction in microgrinding of ceramic materials based on detail material removal mechanisms.

3.2 Literature Review

Many studies have been done in modeling surface finish in conventional grinding in the past. In early study, the empirical or semi-empirical methods were mainly utilized to predict surface roughness in grinding by considering the effects of the grinding tool topography, workpiece material properties and grinding parameters (Tonshoff et al., 1992). Although these models are relatively easy to use in practice, they require time consuming experimental calibration to ensure the accuracy. As the grinding condition varies, these models need re-calibration due to their empirical nature. This has posted a need to analytically model the surface generation in grinding based on the detail material removal mechanisms.

The attempts to analytically model the surface finish in grinding process were initiated by the effort to characterize the actual grinding tool topography from direct stylus measurement. Based on the actual tool profile, various numerical approaches, such as cutting edge trajectory analysis (Law et al. 1973), Monte-Carlo simulation (Yoshikawa et al., 1968) and statistical derivation (Hecker et al., 2003), have been utilized to model surface generation in grinding process. Although these approaches have improved the surface roughness prediction accuracy in grinding metallic materials, they are not suitable for modeling surface chipping/crack in grinding ceramic materials (Malkin, 1989), which are resulted from the brittle nature of ceramic materials. In practice, surface chipping will

affect not only surface finish indexes, such as arithmetic average surface roughness (Ra) and root mean squared surface roughness (Rq), but also have an impact on the strength of the ground parts. Hence, it is crucial to incorporate their influence in modeling surface finish in grinding ceramic materials.

The surface chipping has always been recognized as the major factors that affect surface generation in grinding ceramic materials in both ductile mode and fracture mode grinding. As shown in Figure 3-1(a), when the grinding is conducted in fracture mode, the ground surface is composed of surface chipping regions as well as ductile regions, where visible cutting marks can be observed (Zhou et al. 2002). These surface chippings are related to micro-level fracture in the grinding process, which involves grain cleavage and inter-granular fracture. In a ductile mode dominant grinding, surface chippings are related to the inherent flaws in the workpiece, and they limit the best surface quality that can be achieved in the grinding process (Zarudi et al., 2000), as shown in Figure 3-1(b). In the past, the surface chipping has been mainly investigated by moving indentation experiment. In these studies, it was observed that cracks generated in micro-level fracture can be classified into: median/radial cracks and lateral cracks (Lawn et al, 1980, Marshall et al., 1982). The median/radial cracks are produced inside workpiece, while the lateral cracks will branch onto the workpiece surface and cause surface chipping. In order to predict the surface chipping, Bifano et al. (1991) proposed a critical depth of cut for surface chipping initiation based on the energy balance between machining energy, surface energy and plastic deformation energy. However, as this approach mainly focuses on the initiation of surface chippings instead of their profile, a direct application of this method for surface roughness modeling is difficult. By measuring the total surface

chipping areas and average chipping depth with 3D interferometer, it has been found that surface roughness (Ra) is closely related to surface chipping depth (Maksoud et al., 1999).

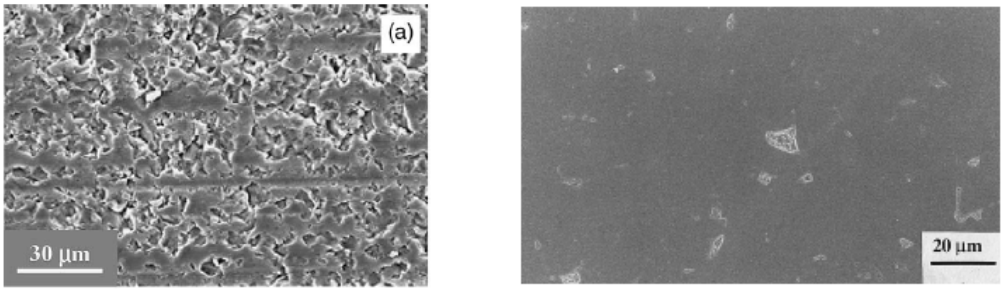

(a)Fracture mode grinding (Zhou et al, 2002) *(b) Ductile mode grinding (Zarudi et al., 2000)*

Figure 3-1 Generation of surface chipping in grinding ceramic

By recognizing the importance of surface chipping on surface finish in grinding, it is desirable to predict their dimension for modeling overall surface roughness. However, this is very difficult in the grinding, not only due to complex material removal mechanisms, but also resulted from the challenge to profile the numerous irregular diamonds on a conventional grinding tool. The microgrinding tool provides a unique opportunity for studying this problem. As there are much less diamonds on a microgrinding tool, individual diamond profile can be accurately captured by 3D profile measurement, such as the white light interferometer. This reduces the error of assuming all diamonds follow a same spherical or pyramid shape. With this advantage, this study will explore modeling of surface finish in microgrinding of ceramic materials based on actual diamond profile and detail material removal mechanisms.

3.3 Experimental Setup and Pretest

A meso-scale grinding system is developed to conduct microgrinding in this study, as shown in Figure 3-2. Its accuracy, load capacity and maximum spindle speed have been discussed in detail in the previous section (2.4)

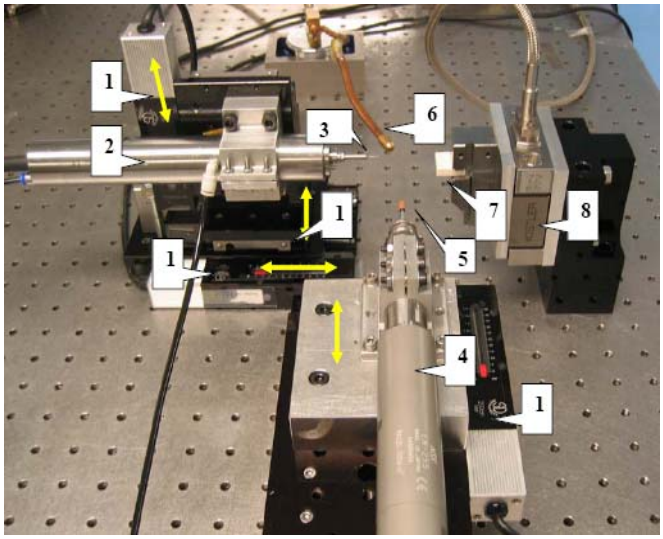

Legend

1. Linear slides
2. Grinding spindle
3. Microgrinding tool
4. Truing spindle
5. Truing wheel
6. Coolant Mist
7. Workpiece
8. Dynamometer

Figure 3-2 Microgrinding experimental setup

A sintered nickel-copper bonded microgrinding tool is used in this study (see Figure 3-3). Its diamond grit is 240, and the diamond concentration is 100. The microgrinding tool was trued to 850μm in diameter by a ∅7.8mm, 120 grit rotary diamond wheel. The spindle speed for the truing wheel was set at 20,000rpm and the microgrinding tool was running at 60,000rpm during truing process. Then, the end face of the microgrinding tool was trued at 5,000rpm to ensure end flatness. During dressing process, the microgrinding tool was dressed by a 220 grit alumina dressing stick to expose diamonds. Alumina (AD94 from Coorstek) is selected as workpiece in this study,

and its material properties are summarized in Table 2-1 in the previous section (2.4). Before the microgrinding experiment, the workpiece was flattened by a ∅7.8mm, 120 grit metal-bonded diamond grinding wheel at 70,000rpm. During the experiment, straight slots are ground on the Alumina workpiece, as shown in Figure 3-3(b). These slots are 6.35mm in length and 0.85mm in width.

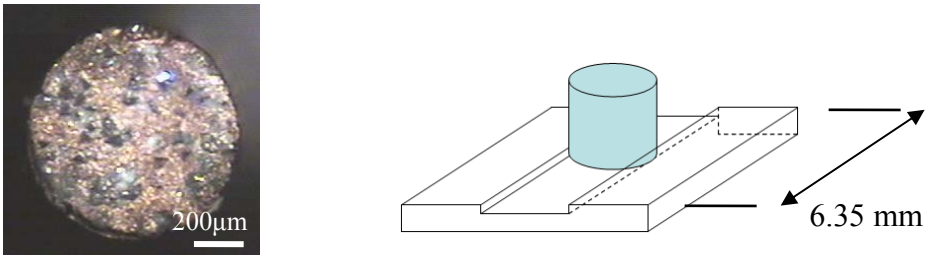

(a) Top view of the microgrinding tool *(b) Microgrinding configuration in end model*

Figure 3-3 Microgrinding tool and end-grinding configuration

In order to determine a proper methodology for modeling surface finish in microgrinding of ceramic materials, the surface of the ground Alumina workpiece is inspected by a scanning electron microscope. The sample Alumina workpiece is ground at 2μm depth of cut, 90mm/min feed rate, 60,000rpm spindle speed and the total grinding depth is 24μm. As shown in Figure 3-4, the ground ceramic surface is composed of surface chipping region and ductile flow region. In the ductile flow region, there are visible cutting marks generated from cutting edge trajectories. The topography of the ground surface is inspected by a white light interferometer. As shown in Figure 3-4, surface chipping has caused the major deviation in the surface profile. This indicates that

it is necessary to model surface generation from both ductile flow mode grinding and fracture mode grinding, which causes the surface chipping.

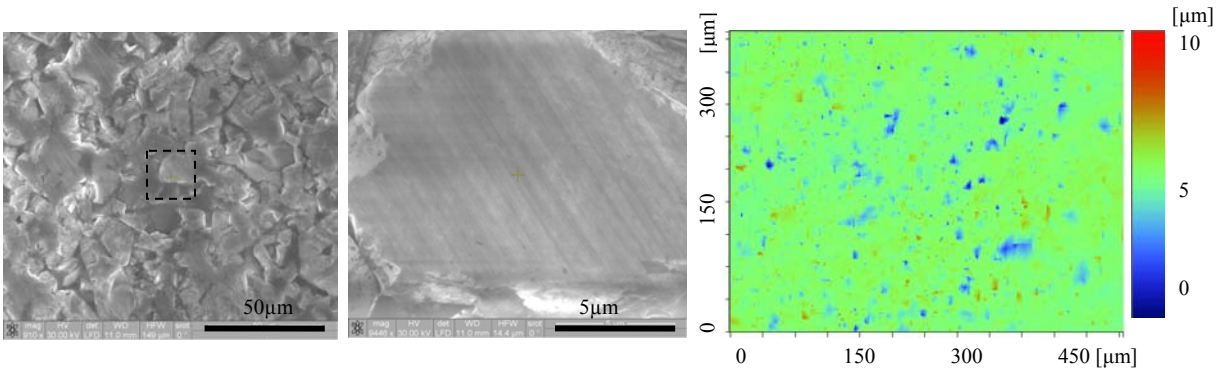

(a) Microground surface *(b) Detail surface texture* *(c) 3D profile of the microground surface*

Figure 3-4 Fracture and ductile regions on a microground alumina workpiece

3.4 Modeling of Surface Chipping in Microgrinding Ceramics

3.4.1 CZM based FEA for modeling fracture related material removal mechanism

As surface chippings are mainly generated in micro-level fracture in microgrinding, it is necessary to model these micro-level fractures for predicting surface chipping. However, since fractures are highly nonlinear processes (Zarudi et al., 2000, Brinksmeier et al., 2006, Griffith, 1920), they are difficult to predict by pure analytical methods. In the past, some numerical approaches have been proposed for modeling material removal in machining brittle materials. For example, Molecular Dynamic (MD) simulation has been used to model chip generation in machining of silicon and ceramic materials (Erdogan, 2000, Ren et al., 2007). However, due to the high computation cost

of MD simulation (Ren et al., 2007), its length scale is usually limited to 100nm, and this is insufficient for modeling the surface generation in grinding process. FEA simulation has also been investigated for modeling grinding process. As FEA is built on the existence of field equations or stiffness matrix for a continuous media, it could have singularity issues in modeling fracture without predefined cracks. To overcome this problem, Continuum Damage Mechanics is developed for modeling material degradation in machining ceramic materials (Liu et al., 2002). However, as actual chip generation is not considered in this approach, it is not suitable for modeling surface generation. In order to achieve an explicit modeling of fracture, cohesive zone method (CZM), proposed by Barenblatt, has been applied in FEA to model the failure of brittle materials under tension, bending and impact (Barenblatt, 1962, Camacho et al., 1996, De Borst et al., 2003, Shet et al., 2004, Warner et al., 2006). The CZM assumes that there exists a micro-level traction region at the edge of cracks, and its traction determines nucleation, propagation and coalescence of a crack (Liu et al., 2002) (see Figure 3-5). By retaining both mathematical continuity and physical separation, CZM based FEA can model crack initiation, branch and fragment generation by allowing elements to separate based on grain or sub-grain level material properties. Hence, it is suitable for modeling micro-level fracture in microgrinding of ceramic materials to predict the possible surface chipping.

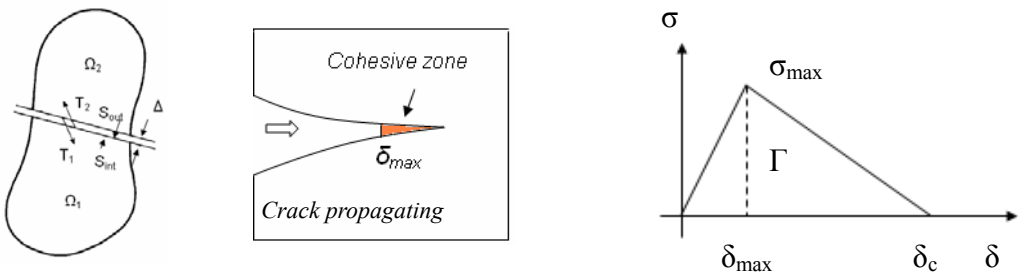

(a) Scheme of fracture in CZM *(b) Bilinear cohesive behavior*

Figure 3-5 Modeling fracture process by cohesive zone method (Camacho et al., 1996)

Characterized by different traction-separation profile, CZM based FEA are classified into: exponential behavior, trapezoid behavior and bilinear behavior (Shet et al., 2004). The exponential behavior is suitable for modeling tensile failure of metallic and bi-metallic materials. The trapezoid behavior is designed to model fracture involving yielding, such as failure of elastic-plastic materials. The bilinear behavior is a special case of trapezoid behavior by allowing little material yielding (see Figure 3-5(b)). It is mainly used to model fracture of brittle materials (Shet et al., 2004). Hence, it is selected for modeling micro-level fracture in microgrinding of ceramic materials. To specify a bilinear CZM, early researchers proposed utilizing cohesive strength (σ_{max}) or equivalent separation displacement (δ_{max}), critical separation displacement (δ_c) and cohesive energy (Γ) derived from different theories. To determine these cohesive parameters, Warner and Molinari (2006) proposed a numerical calibration technique, in which macro-level material properties are fitted from micro-level cohesive strength by CZM based FEA. Although it can provide a reasonablely accurate estimation, it requires time-consuming calculation and experimental verification. A more direct approach, proposed by Camacho

and Ortiz, is to derive cohesive parameters from pre-existing flaws that populate in grains (Camacho et al., 1996). In their assumption, the mathematically derived cohesive strength in CZM essentially is the fracture strength (σ_{fr}) in ceramic workpiece that prevents crack from propagation. Hence, it can be calculated from fracture toughness (K_{IC}) and collinear cracks/flaws of half-width (a_0), stated in Equation (3-1).

Moreover, it is assumed that the shear cohesive strength is close to tensile cohesive strength in the micro-scale in this approach. This assumption is derived from the fact that in conventional scale, ceramic materials mainly exhibit tensile failure instead of shear failure under normal temperature (Griffith, 1920). By further adapting the concept that grain boundary shear motion is controlled by atomic shuffling, and tensile strength of the grain boundary would not necessarily change shear strength, the combined influence of cohesive tensile and shear strength can be assessed in an independent manner (Warner et al., 2006), as stated in Equation (3-2). The initial slope (s) determines the response of cohesive traction to external loading. In early studies, it is found that a high initial slope could cause converging issue in CZM based FEA (Zavattieri et al., 2001, Espinosa et al., 2003), while a low initial slope will introduce extra deformation in cohesive bonding. For balance, a semi-empirical value, as shown in Equation (3-3), based on bulk elasticity (E) and maximum finite element size (d), is usually used for initial slope in CZM based FEA (Zavattieri et al., 2001, Espinosa et al., 2003). This method is also adopted in this study.

$$\sigma_0 = \sigma_{fr} = \frac{K_{IC}}{\sqrt{\pi a_0}} \tag{3-1}$$

$$\max\left(\frac{\delta_N}{\delta_{N\max}},\frac{\delta_S}{\delta_{S\max}},\frac{\delta_T}{\delta_{T\max}}\right)=1 \quad \text{or} \quad \max\left(\frac{\sigma_N}{\sigma_{N\max}},\frac{\sigma_S}{\sigma_{S\max}},\frac{\sigma_T}{\sigma_{T\max}}\right)=1 \tag{3-2}$$

$$s=\frac{10E}{d} \tag{3-3}$$

Different from cohesive strength, which specifies the initiation of material degradation, cohesive energy characterizes the total damage that a cohesive bonding can undertake before failure. Based on energy dissipation analysis, fracture is a process during which external work is converted into recoverable elastic energy and irrecoverable dissipative energy, assuming small kinematics energy due to rigid body motion (Warner et al., 2006). The irrecoverable energy is mainly dissipated in plastic deformation, fracture and other inelastic work. For ceramic materials, assuming a negligible plastic deformation, the irrecoverable energy that dissipates in cohesive zone is equal to the cohesive energy. Hence, cohesive energy can be calculated by J-integral, which is a path independent integration of strain energy release rates during fracture (Rice, 1968). Based on Griffith theory (or the maximum strain energy release rate theory), resistance in material to fracture initiation does not depend on the fracture modes mixity (Green, 1998), the total strain energy release rates in a general fracture process, which consists of Mode I, II and III fracture, can be calculated from the energy in pure mode I fracture (Green, 1998, Suresh et al., 1991), stated by Equation (3-4).

$$\Gamma = J_C = \frac{1}{E}(K_I^2 + K_{II}^2) + \frac{1+\nu}{E} K_{III}^2 = J_{IC} = \frac{K_{IC}^2}{E} \tag{3-4}$$

3.4.2 Configuration of CZM based FEA for ceramic microgrinding

In order to model material removal due to micro-level fracture in microgrinding by CZM based FEA, it is important to develop a proper FEA model which characterizes the microgrinding tool. As shown in Figure 3-6, individual diamonds on the microgrinding tool are measured by the 3D white light interferometer. As the diamonds on the outer region of a grinding tool are responsible for most of material removal in end grinding, it is reasonable to assume that most chip generation is conducted by these diamonds. Their protrusions, spacing angles (α) and cutting edge angles (β) are measured by line-scan, as summarized in Table 3-1. Each measurement is repeated three times for the average value. As shown in Table 3-1, the variation in diamond protrusion and cutting edge angle is much smaller than the spacing angle. This indicates that it is proper to characterize diamond profile with average protrusion and cutting edge angle, while using measured value for spacing angles. Based on these diamond profiles and locations, detail chip load can be calculated for individual diamond from grinding parameters. As shown in Figure 3-7, during a fully engaged end grinding process, chip load reaches maximum value when diamonds are rotating to the middle of ground surface, and the actual chip load is more like a parallelogram considering the slope of diamond cutting edge.

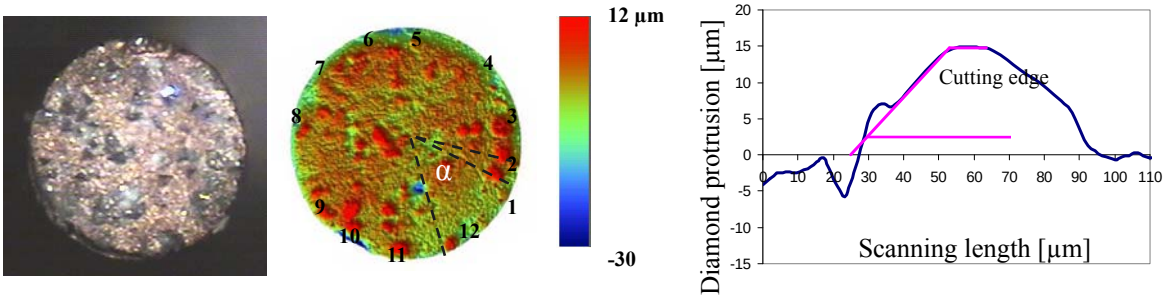

(a) Microgrinding tool *(b) 3D tool topography* *(c) Line-scan of Diamond 2*

Figure 3-6 Microgrinding tool, topography and diamond cutting edge profile

Table 3-1 Dimension of diamonds on a microgrinding tool

Diamond	Protrusion (µm)	Cutting edge angle β (°)	Spacing angle α (°)
1	15.2±1.1	26.7±3.1	50
2	15.7±0.9	30.3±2.2	13
3	11.0±0.9	28.7±4.6	18
4	10.8±0.3	31.2±2.1	37
5	11.1±0.1	24.1±1.5	51
6	10.1±0.2	33.4±1.3	27
7	10.5±0.3	39.9±2.6	12
8	10.7±0.6	27.0±2.3	40
9	8.6±0.7	25.6±1.8	40
10	14.4±0.2	26.7±1.6	15
11	13.4±0.3	45.2±2.1	35
12	6.8±0.3	41.9±3.7	22
Average	11.5	31.9	30
Standard deviation	2.7	6.9	12

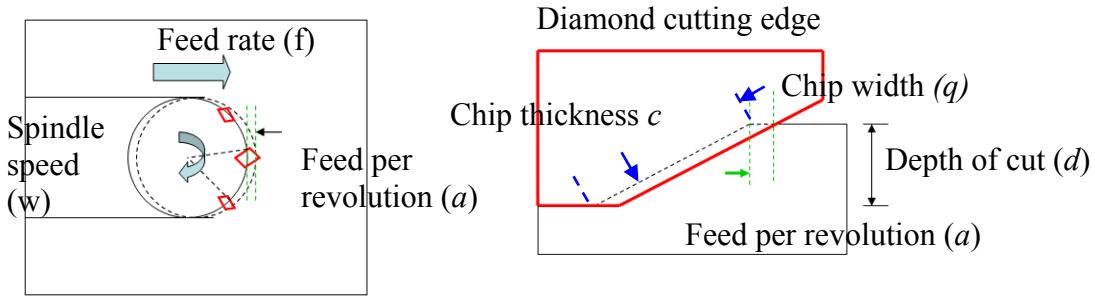

(a) End grinding configuration *(b) Actual chip load on diamond cutting edge*

Figure 3-7 Scheme of microgrinding process and corresponding chip load.

As shown in Figure 3-7, actual chip load in microgrinding is characterized by diamond cutting edge angle, feed per revolution and depth of cut. One major concern in microgrinding lies in its much lower tool stiffness. This will result in tool deflection in grinding high strength ceramic materials. In end grinding, the correlation between actual depth of cut (ADOC) and nominal depth of cut (NDOC) at *i*th pass is proposed by Zhang et al. (2001), based on time invariant system loop stiffness (K_l) and cutting stiffness (K_W), as shown in Equation (3-5). Our experimental study demonstrated that typical microgrinding system loop stiffness is around 0.269N/μm, and cutting stiffness is around 0.471N/μm. Based on these values, the ADOC is expected to be close to NODC as the microgrinding tool machine deep into the workpiece at a consistent depth of cut and feed rate. As calculated by Equation (3-5), after grinding twelve grinding passes, the difference between ADOC and NDOC is smaller than 1%.

$$ADOC = \left\{1 - \left(\frac{k_W}{k_l + k_W}\right)^i\right\} NDOC$$

$$ADOC = \left\{1 - \left(\frac{0.471}{0.471 + 0.269}\right)^{12}\right\} NDOC = 99.55\% NDOC$$

(3-5)(Zhang et al., 2001)

To validate this analysis, the actual grinding depth in the microgrinding was measured by probing the ground surface with the same microgrinding tool, as shown in Figure 3-8. Before microgrinding, the initial surface was measured by monitoring the contacting force through probing. Before the grinding operation, the microgrinding tool is gauged against a fixed location for the possible tool wear, and this probing was repeated for three times for the average value. As shown in Figure 3-8(c), when the microgrinding tool grinds deep into the workpiece, the increase in the actual total depth of cut equals to the nominal increase. This suggests that the ADOC at the last several passes equals to the NDOC.

Hence, the microgrinding operation is conducted for twelve passes in the experimental study in this paper. The NDOC can, therefore, be directly used in CZM based FEA for modeling material removal.

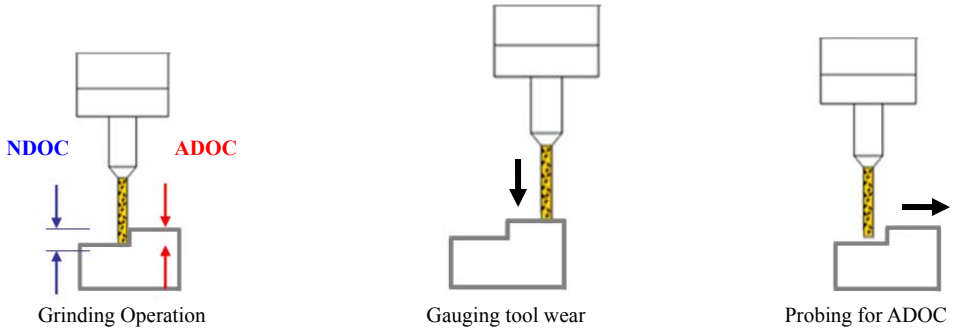

(a) Microgrinding, tool wear gauging and surface probing for the actual

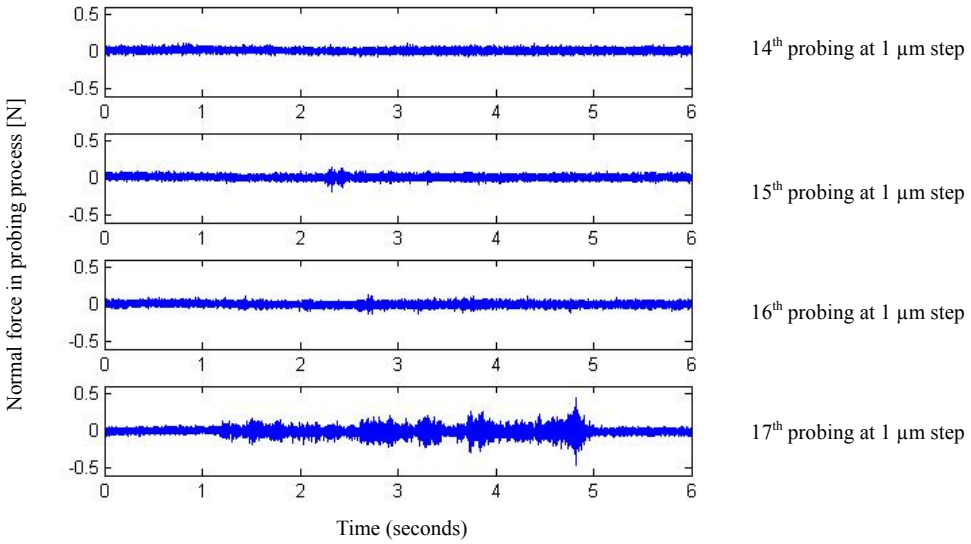

(b) Contacting force in the probing for 2 µm ADOC, 90 mm/min after 10 passes

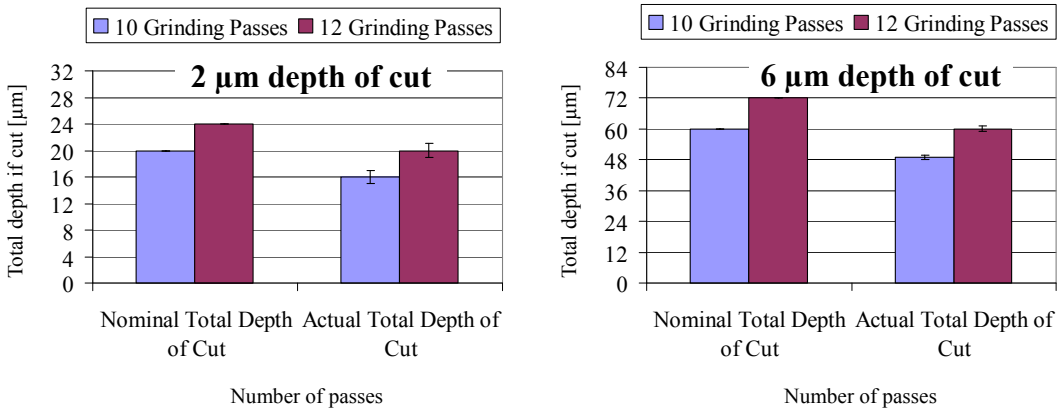

(c) Measured ADOC at 2 µm and 6 µm NDOC, 90 mm/min after 10 passes and 12 passes

Figure 3-8 Determination of ADOC in the microgrinding operation

Based on the maximum grinding chip profile, the CZM based FEA configuration is developed for individual diamond in microgrinding of ceramic materials, as shown in Figure. 3-9. The CZM based FEA model is composed of a diamond cutter and a ceramic workpiece. The measured average diamond cutting angle is used for the diamond cutter, and its width is the same as the calculated chip width. The ceramic workpiece consists of cohesive FEA region and regular FEA region. The major material removal takes place in the cohesive FEA region, and it is composed of layers of sub-domains. These sub-domains are 1.3μm x 1.3μm x 1.3μm in dimension, and they are bonded together by the designed cohesive properties. The regular FEA regions are bonded to cohesive FEA on the side, and they are constrained by the fixed boundary. The CZM based FEA is implemented in a commercial FEA software ABAQUS. Four nodes linear tetrahedron is selected as element for meshing the ceramic workpiece, and the maximum mesh size is set to be 0.8μm.

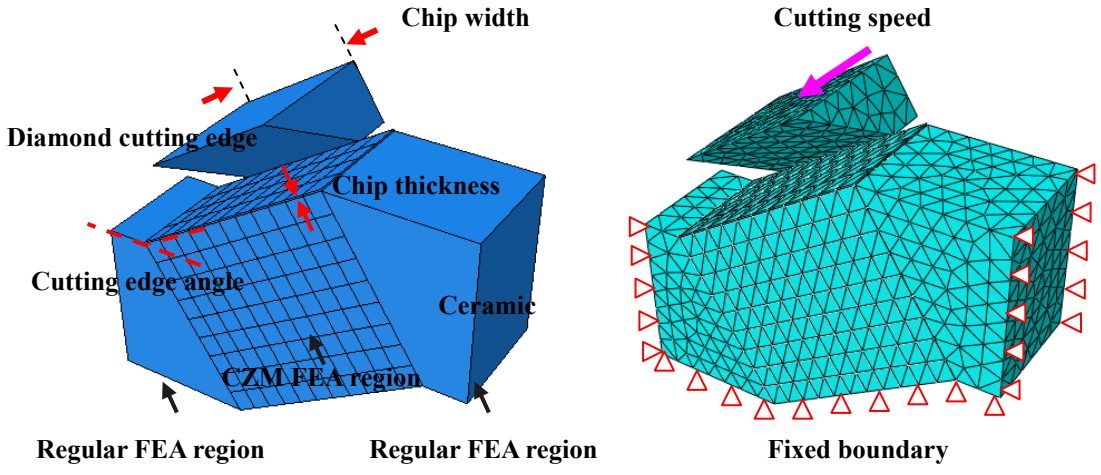

(a) FEA configuration *(b) Mesh and boundary condition*

Figure 3-9 CZM based FEA for microgrinding process

3.4.3 Prediction of surface chipping from CZM based FEA

Different from single diamond moving indentation, in which surface chipping is directly related to the specific diamond that conducts cutting, grinding involves surface generation from multiple diamonds. Therefore, surface chipping is a more cumulative process, in which subsurface damage from one diamond trajectory could become surface chipping in an afterward trajectory from another diamond. Moreover, early micromachining study has also suggested that there is variation in material properties in micro-scale due to the presence of inherent flaws, dislocations and difference in grain direction (Vogler et al., 2003). Thus, surface chipping in microgrinding is related to the localized initial flaws as well as the trajectories from multiple diamonds. To quantify variations in initial flaws, Alumina workpiece is inspected for the ceramography, as shown in Figure 3-10. Because the Alumina workpiece is flattened by a 120 grit grinding wheel in the flattening procedure in the experiment, in order to reflect its influence on the ceramography, typical superfine grit grinding for the ceramography preparation is not employed. The flattened Alumina is polished by 3μm and 1μm diamond grits for 30 minutes respectively, and it is cleaned by ultrasonic bath for 1 hour. As shown in Figure 3-10(a), there is a relatively high flaw density, which is resulted from flattening process. The surface flaws on the polished surface are counted and measured in six 150μm x 150μm surface samples. The distribution of the half flaw size is shown in Figure 3-10(b). Average flaw size is 5.96μm, and it follows a Weibull distribution, as shown in Equation (3-6).

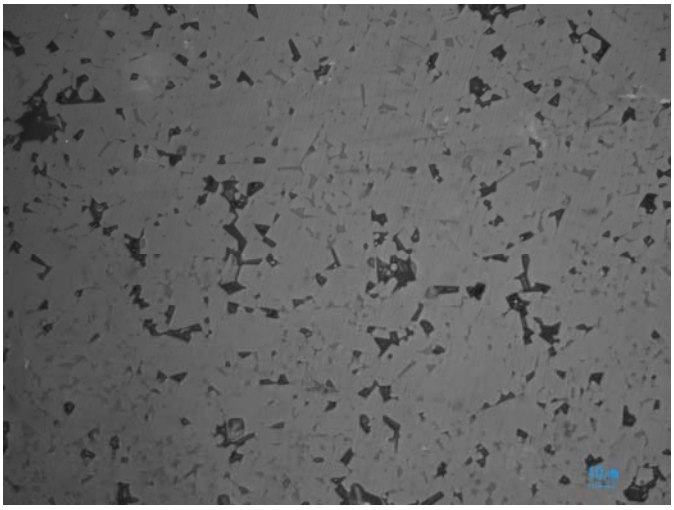

(a) Polished surface after flatting process

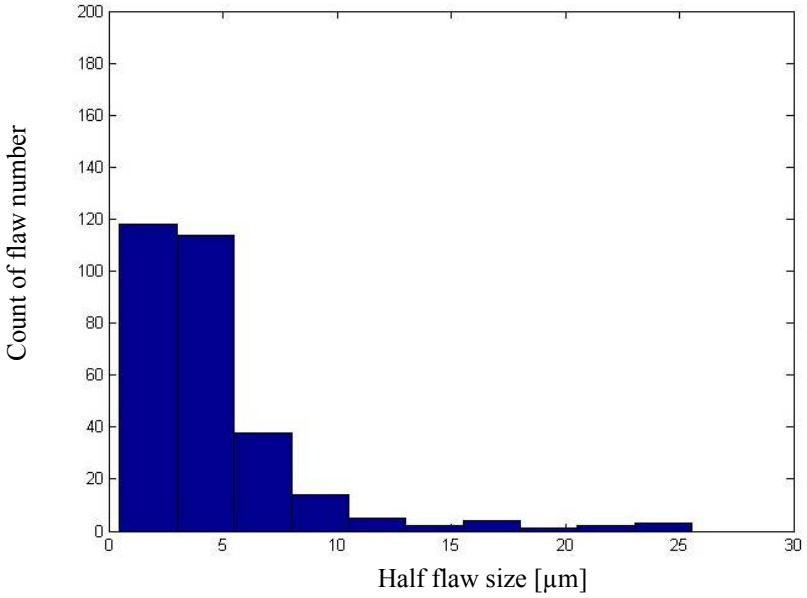

(b) Half flaw size distribution

Figure 3-10 Initial surface flaws populate in the workpiece after flattening process

$$f(x) = \frac{5.07}{1.39}\left(\frac{x}{1.39}\right)^{4.07} e^{-(x/1.39)\times 5.07} \tag{3-6}$$

By characterizing surface flaws in detail, it is possible to assess their influence in surface generation in CZM based FEA by applying different levels of cohesive strength. As summarized in Table 3-2, the cohesive strength and its corresponding critical cohesive displacement is calculated for different flaw size ranging from 1μm to 18μm. These parameters are then implemented in simulation for Diamond 1 (see Table 3-1) at 90mm/min feed rate, 60,000rpm spindle speed and 4μm depth of cut. In the simulation, subsurface damage is calculated based on the level of degradation at each cohesive bonding. The bonding damage level ranges from 0 to 1, which represents no degradation to fully damaged.

Table 3-2 Summary of CZM Parameters

Parameters	
Maximum mesh size [μm]	0.8
Initial stiffness [GPa/mm]	3787500
Half-width of crack [μm]	1, 6, 12, 18
Micro-level Cohesive strength [GPa]	2.54, 1.04, 0.73, 0.52
Maximum displacement [mm]	6.71e-7, 2.74e-7, 1.94e-7, 1.58e-7
Fracture Energy [J/m^2]	66.8
Feed rate [mm/min]	90
Depth of cut [μm]	4
Spindle speed [rpm]	60,000

As shown in Figure 3-11, subsurface damage spreads into the ceramic workpiece due to material removal, similar to the experimental observation in moving indentation study (Marshall, 1984). Underneath the diamond-ceramic contacting boundary, there is a fully damaged subsurface region, and it is most likely to become surface chipping,

considering an accumulation of trajectories of multiple diamonds afterwards. Therefore, the depth of this fully damaged subsurface region is treated as the possible surface chipping depth in this study. This fully damaged subsurface depth is measured when the designed grinding chip has been removed from the workpiece, as shown in Figure 3-11, and a larger initial flaw promotes more aggressive subsurface damage in the workpiece. By contrast, when initial flaw is small, grinding will barely cause any subsurface damage due to the higher cohesive strength, and the microgrinding is likely in ductile flow mode. This shows that there exists a critical flaw size which distinguishes ductile flow grinding from fracture mode grinding. When the workpiece has an inherent flaw smaller than this critical value, the workpiece is so strong that it only has little subsurface damage. However, when the initial flaw goes beyond this critical value, it will behave much more fragile and produces chippings. By estimating this critical flaw size from FEA simulation, in the case when it only produces a negligible subsurface damage depth, the surface generation in microgrinding can be selectively modeled in ductile flow mode or fracture model based on the localized initial flaw in different size. The complex surface generation in microgrinding is, therefore, simplified to surface generation in ductile mode and fracture mode due to cutting from selected diamonds.

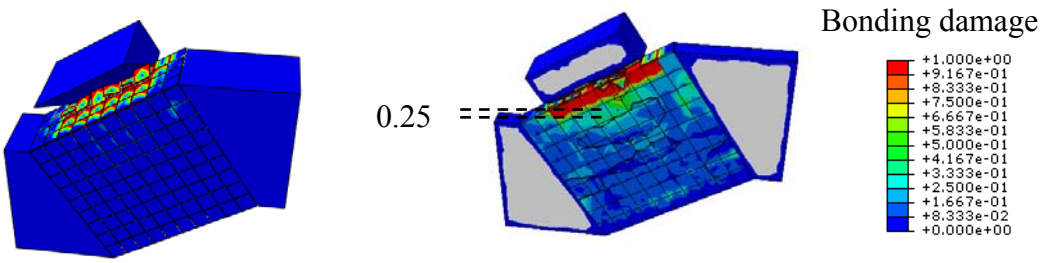

(a) Surface damage at 1µm half flaw size

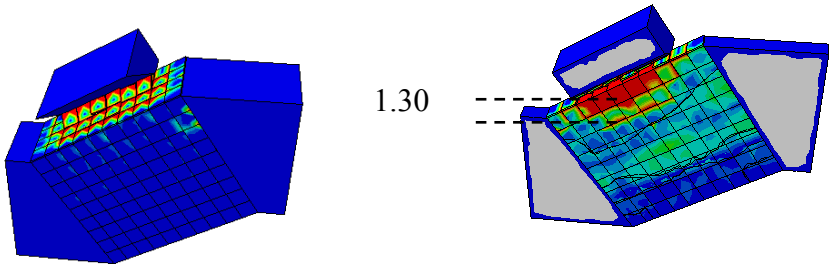

(b) Surface damage at 6µm half flaw size

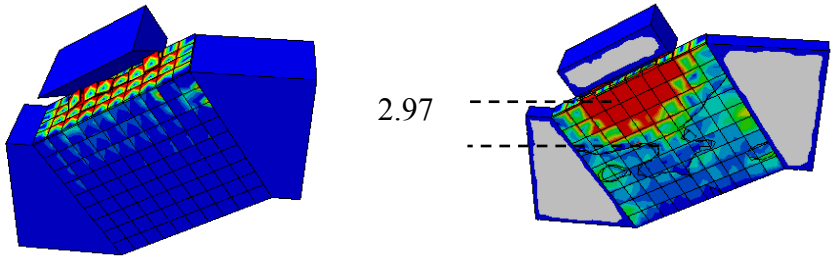

(c) Surface damage at 12µm half flaw size

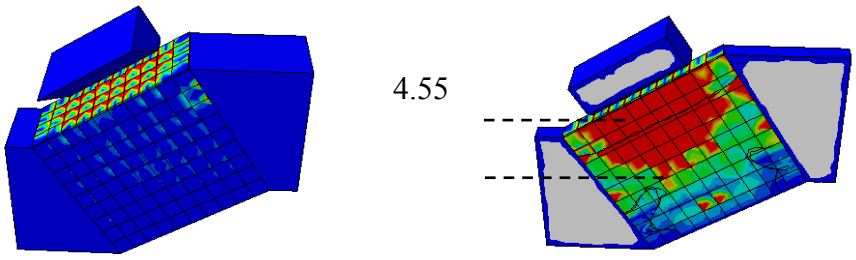

(d) Surface damage at 18µm half flaw size

Figure 3-11 Effect of flaw sizes on surface damage depth at 4µm depth of cut, 90mm/min feed rate, 60,000rpm spindle speed

3.5 Surface Generation in Different Grinding Modes

3.5.1 Surface generation in ductile flow mode grinding

The trajectory analysis has been mainly utilized in modeling surface generation in metallic grinding process, in which grinding is assumed effective material removal, and surface generation is mainly determined by grinding wheel topography and grinding parameters. This assumption is also adopted in this study for modeling surface generation in ductile flow mode microgrinding of ceramic materials. A typical trajectory analysis involves grinding tool topography modeling, numerical simulation and surface finish evaluation. The grinding tool topography modeling is to extract the key geometry profiles of the grinding tool that has impact on the surface generation. Early studies assume the cutting edges are in a cone or pyramid shape, and they follow a uniform distribution on the grinding wheel (Malkin, 1989). Based on the measured diamond profile in Table 3-1, Diamonds 1, 2 and 10 have higher protrusion than others, and they are more important than other diamonds for the surface generation in the ductile flow mode grinding. The trajectory analysis is performed for these diamonds at 4μm depth of cut at different feed rates at 60,000 spindle speed as shown in Figure 3-12. The simulated arithmetic average surface roughness (Ra) is much smaller than the experimental result, as shown in Figure 3-12(d). This suggests the pure trajectory analysis is insufficient for surface roughness prediction in microgrinding of ceramic materials.

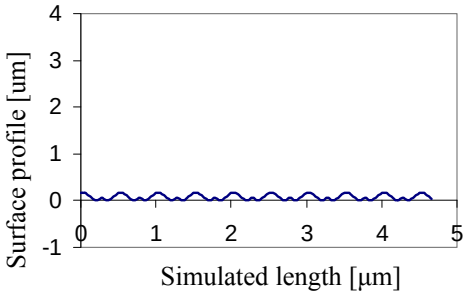

(a) Feed rate: 30 mm/min

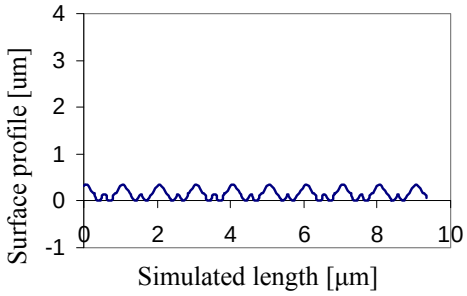

(b) Feed rate: 30 mm/min

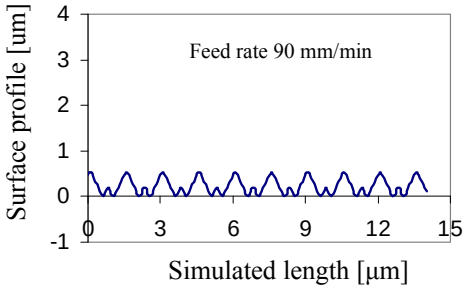

(c) Feed rate: 90 mm/min

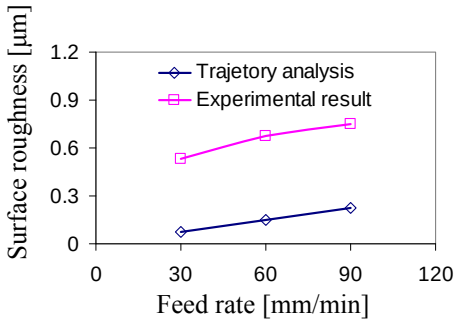

(d) Experimental and simulated surface roughness

Figure 3-12 Simulated surface generation in microgrinding

3.5.2 Calibration of possible surface chipping depth with initial flaw size

In order to determine the correlation between surface chipping depths with the initial flaw size, CZM based FEA is performed at different feed rates and depths of cut for the fully damaged subsurface depth. The Diamond 1 is selected in this calibration, as it undertakes high chip load due to its above average protrusion and spacing angle. It is expected to cause deeper subsurface damage than other diamonds during one tool rotation. The corresponding chip profiles are calculated for different grinding conditions as summarized in Table 3-3.

Table 3-3 Maximum chip load on Diamond 1

Depth of cut [μm]	Feed rate [mm/min]	Chip width [μm]	Chip thickness [μm]
2	90	3.11	0.19
4	90	6.23	0.19
6	90	9.34	0.19
4	30	6.23	0.06
4	60	6.23	0.13

The CZM based FEA is performed for four levels of cohesive strength with initial flaw size of 1, 6, 12 and 18μm. The detail cohesive parameters are summarized in Table 3-2. The fully damaged subsurface depth is measured at same simulation time point when designed chip load is removed, as summarized in Figure 3-13. The detail CZM based FEA simulation for different grinding conditions are shown in Figures 3-11, 3-14, 3-15, 3-16 and 3-17. As suggested in Figure 3-13, larger depth of cut and higher feed rate will increase fully damaged subsurface depth. When the half initial flaw size is small, the fully damaged subsurface depth will approach zero. By fitting the correlation between fully damaged subsurface depth and half initial flaw size with a second order polynomial, it can be inferred that there is a critical half flaw size (C_R), at which the fully damaged subsurface depth is zero. These critical half flaw sizes are calculated for each grinding condition, as summarized in Table 3-4, along with the coefficient for the fitted polynomials.

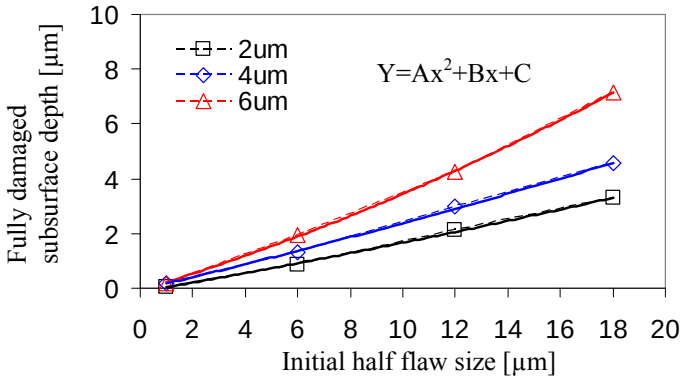

(a) Effect of depth of cut

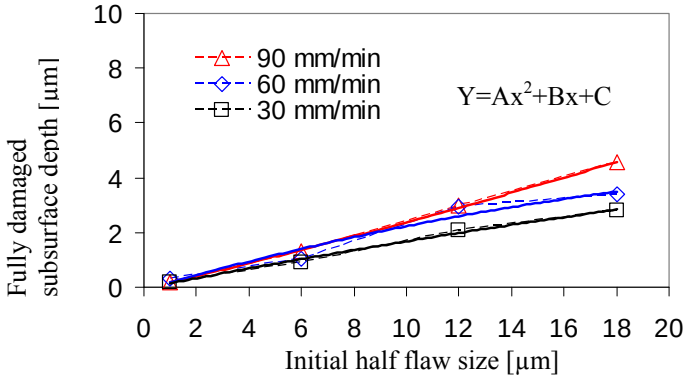

(b) Effect of feed rate

Figure 3-13 Effect of initial flaw sizes on fully damaged subsurface depth

Table 3-4 Fitted coefficients for the second-order polynomials

Depth of cut [µm]	Feed rate [mm/min]	A	B	C	Critical half flaw size [µm]
2	90	0.006	0.2916	-0.0753	0.27
4	90	0.0016	0.2273	-0.0551	0.24
6	90	0.0014	0.1655	-0.1287	0.77
4	30	-0.0015	0.1870	-0.0366	0.20
4	60	0.0041	0.2727	-0.0837	0.31

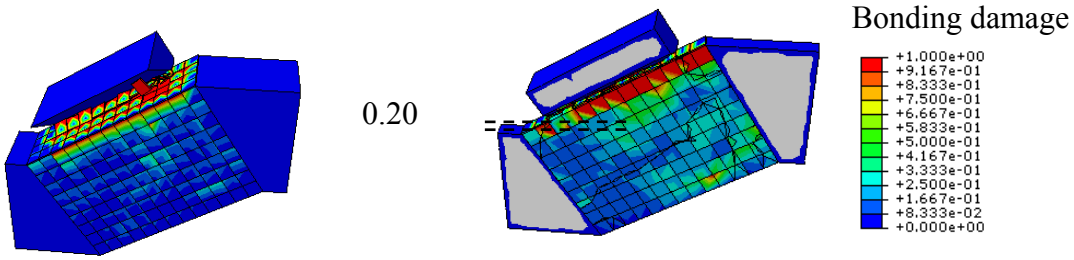

(a) Surface damage at 1μm half flaw size

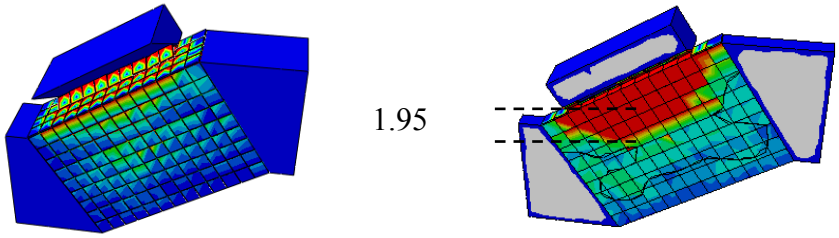

(b) Surface damage at 6μm half flaw size

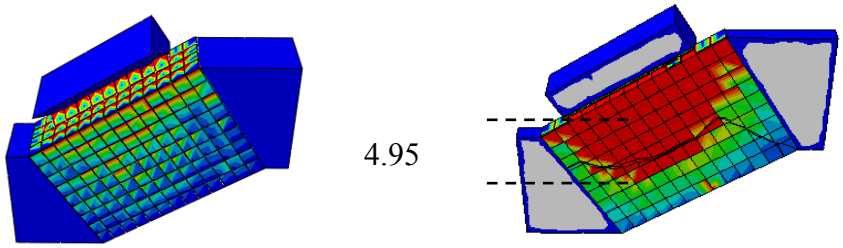

(c) Surface damage at 12μm half flaw size

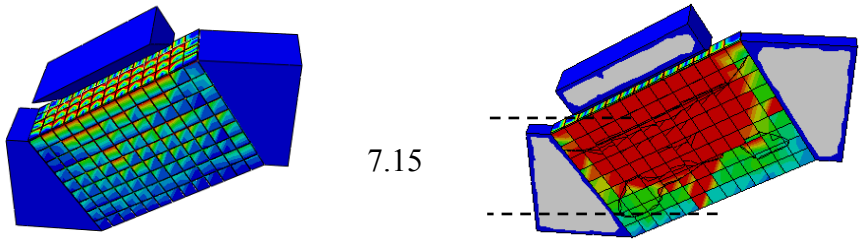

(d) Surface damage at 18μm half flaw size

Figure 3-14 Effect of flaw sizes on subsurface damage depth at 6μm depth of cut, 90mm/min feed rate, 60,000rpm spindle speed

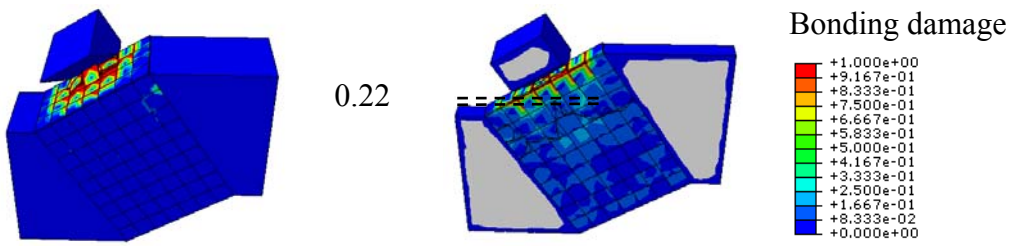

(a) Surface damage at 1μm half flaw size

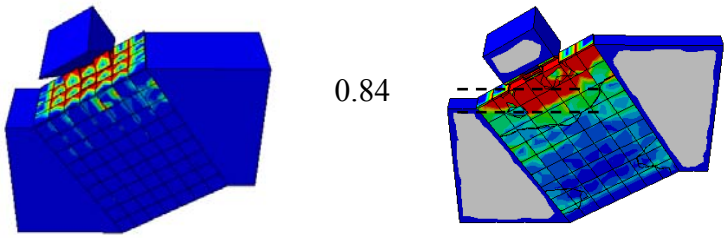

(b) Surface damage at 6μm half flaw size

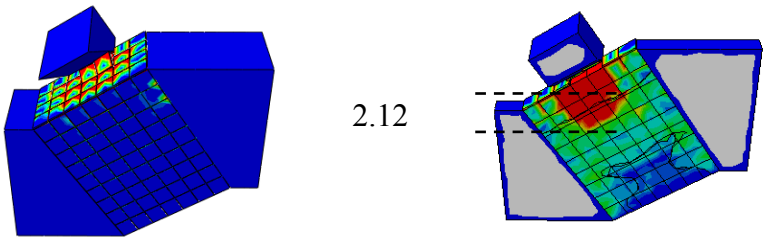

(c) Surface damage at 12μm half flaw size

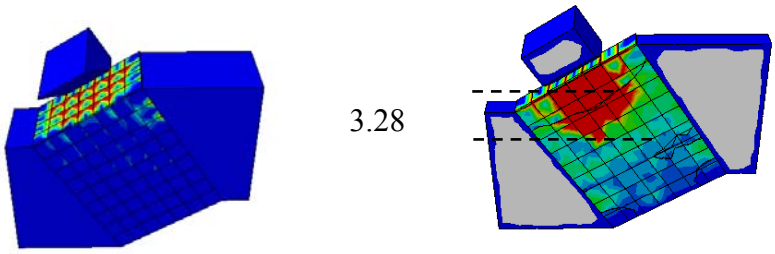

(d) Surface damage at 18μm half flaw size

Figure 3-15 Effect of flaw sizes on subsurface damage depth at 2μm depth of cut, 90mm/min feed rate, 60,000rpm spindle speed

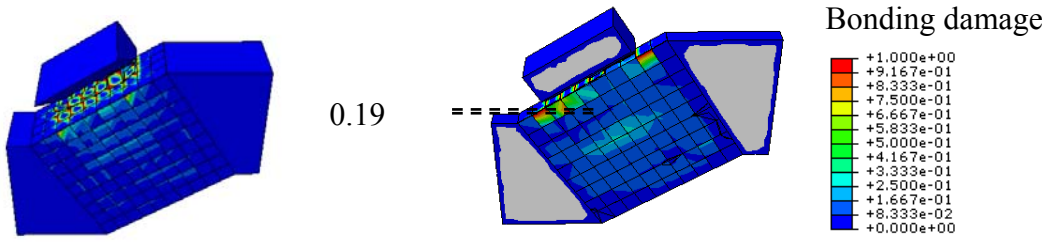

(a) Surface damage at 1μm half flaw size

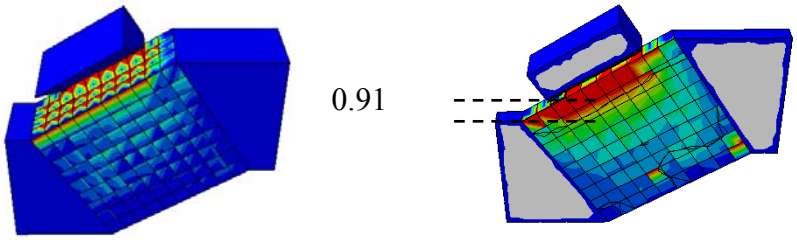

(b) Surface damage at 6μm half flaw size

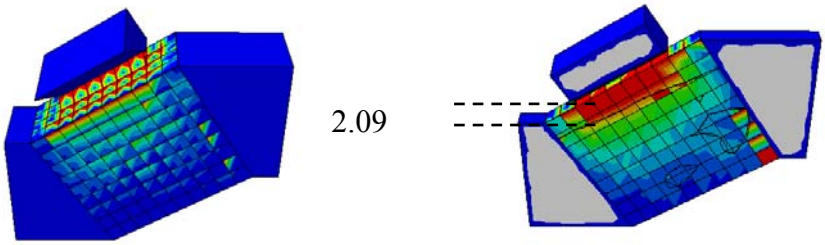

(c) Surface damage at 12μm half flaw size

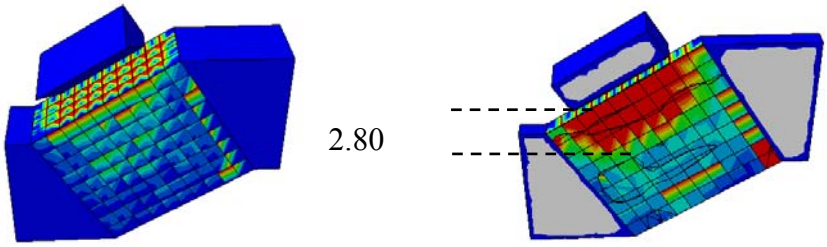

(d) Surface damage at 18μm half flaw size

Figure 3-16 Effect of flaw sizes on subsurface damage depth at 4μm depth of cut, 30mm/min feed rate, 60,000rpm spindle speed

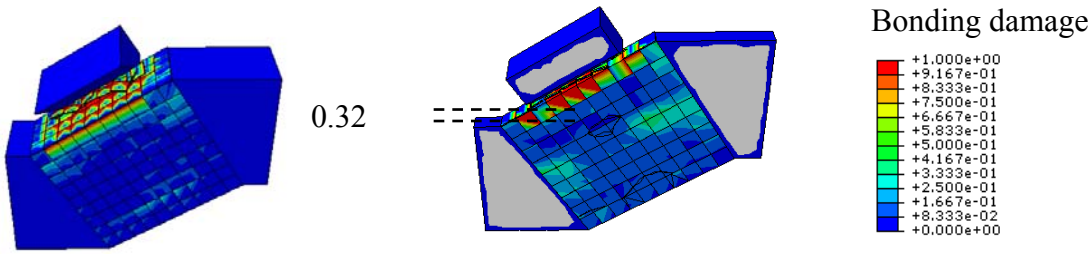

(a) Surface damage at 1μm half flaw size

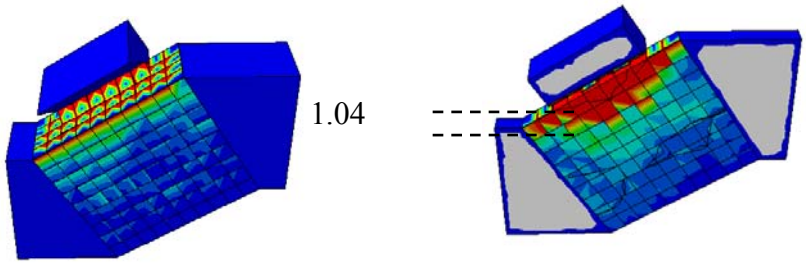

(b) Surface damage at 6μm half flaw size

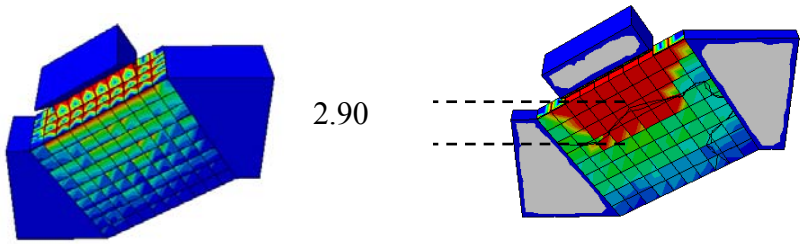

(c) Surface damage at 12μm half flaw size

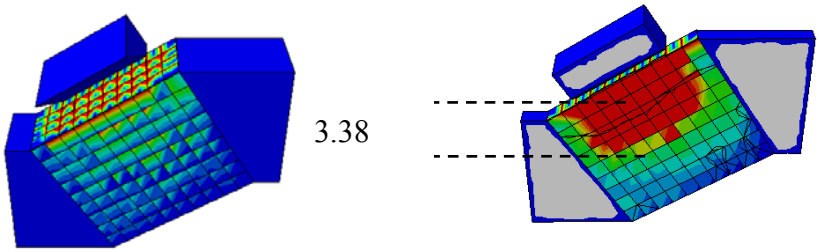

(d) Surface damage at 18μm half flaw size

Figure 3-17 Effect of flaw sizes on subsurface damage depth at 4μm depth of cut, 60mm/min feed rate, 60,000rpm spindle speed

3.6 Resultant Surface Generation and Experimental Verification

3.6.1 Methodology for resultant surface generation

To construct the resultant surface profile in microgrinding of ceramic materials, surface generation from both ductile flow mode grinding and micro-level fracture mode grinding is considered. The flow chart for this simulation procedure is shown in Figure 3-18. At beginning, the initial half flaw distribution is generated based on the fitted Weibull distribution from measurement. Individual half flaw is compared with the critical flaw size (C_R). If it is smaller than the critical flaw size, the grinding is conducted in ductile flow mode. The surface profile is calculated from pure trajectory analysis as shown in Figure 3-12. If the statistically generated flaw size is larger than the critical flaw size, it is assumed the grinding is conducted in fracture mode, and the fully damaged subsurface depth is taken for the surface chipping depth. The simulated surface profile from ductile flow mode trajectory and surface chipping is combined for final surface profile.

As there are multiple diamonds on a grinding tool, in trajectory analysis, diamonds that have higher protrusion are considered for surface generation. In fracture mode grinding, surface chipping is assumed to be an accumulated result from multiple diamonds, and the maximum fully damaged depth in one tool rotation is used.

Therefore, the major difference between the proposed surface chipping prediction from critical flaw size and the surface chipping prediction from critical depth of cut in Bifano's (1991) study lies in that this study assumes that size variation of the initial flaw in the workpiece determines the happening of the surface chipping at that particular location, while Bifano assumed that as long as the depth of cut is large enough, it will always cause surface chipping. The approach proposed in this study is more

chipping location focused, while Bifano's method focuses on whether chipping will happen instead of where and how much are the surface chipping.

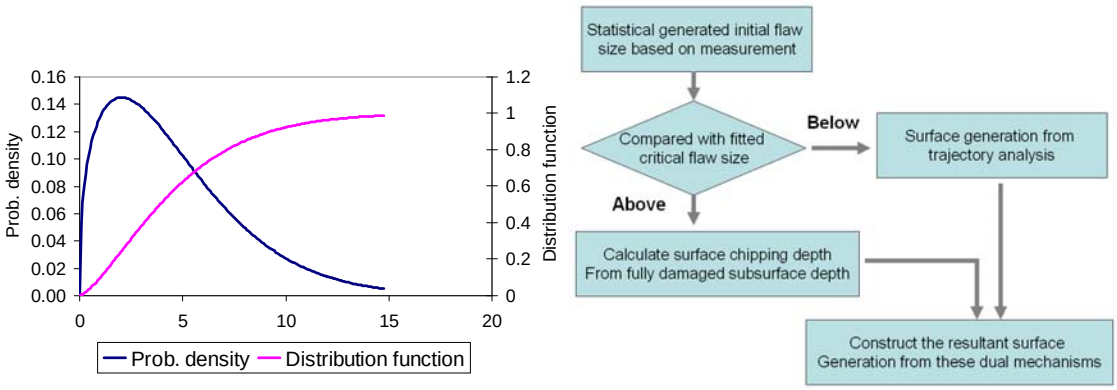

(a) Initial flaw distribution *(b) Surface finish generation*

Figure 3-18 Flow chart for numerical simulation for surface profile generation

3.6.2 Comparison of experimental and simulation results

The simulated surface profiles are compared with experimental results for different grinding conditions, as shown in Figure 3-19. The ground surface profile is measured by a Taylor-Hobson surface profilometer (Talysurf 50). The measurement is repeated for four times for average surface roughness. The actual surface profile is shown in Figure 3-19(a, c, e) for different grinding depths of cut at 90mm/min feed rate and 60,000rpm spindle speed. The corresponding simulated surface profile is shown in Figure 3-19(b, d, and f). As suggested by the measured surface profile, surface chipping depth increases with the grinding depth of cut. This is also reflected in the simulation result, in

which predicted surface chipping depth increases with the depth of cut. This also indicates the assumption that fully damaged subsurface depth determines surface chipping depth matches well with the actual grinding process.

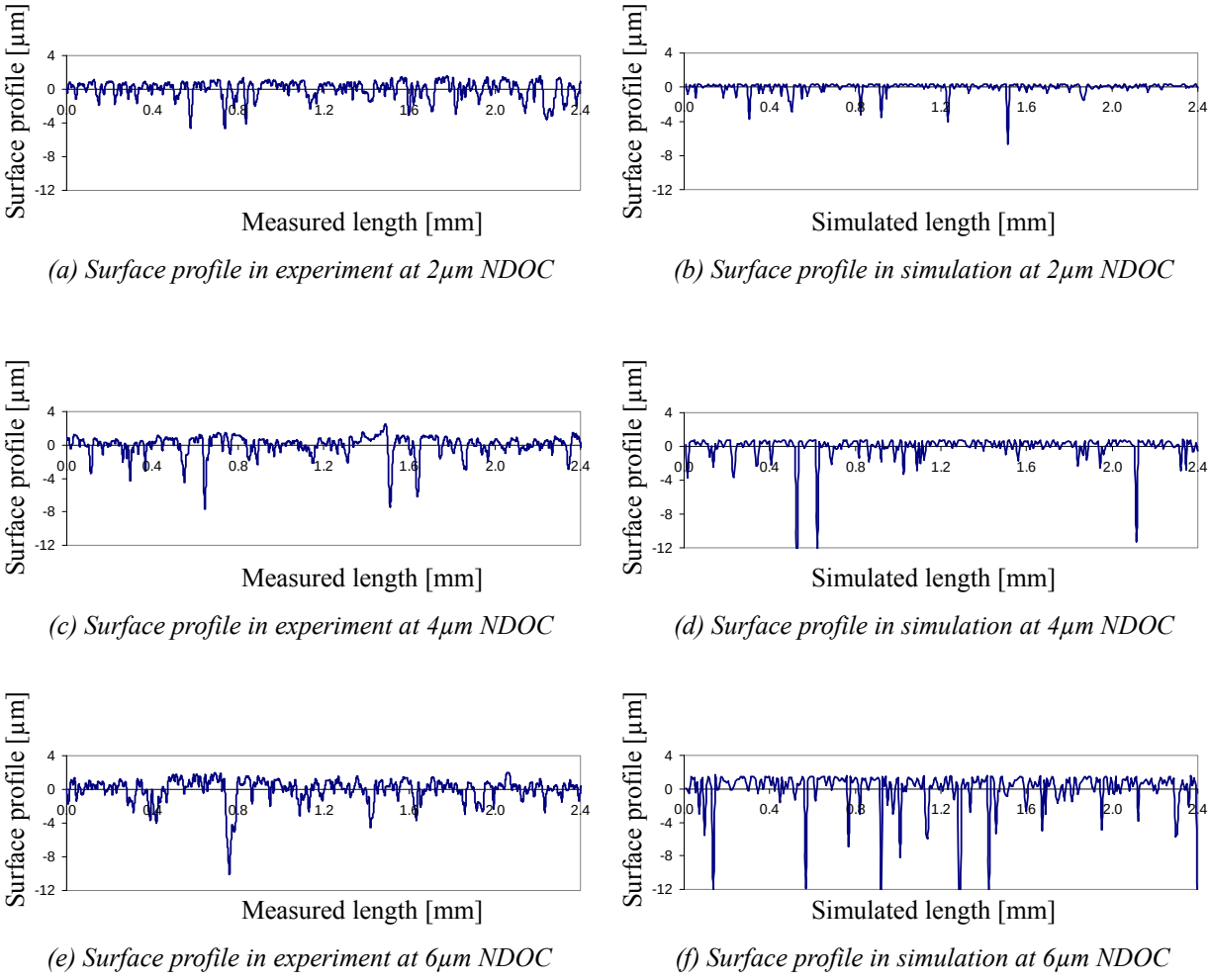

(a) Surface profile in experiment at 2µm NDOC

(b) Surface profile in simulation at 2µm NDOC

(c) Surface profile in experiment at 4µm NDOC

(d) Surface profile in simulation at 4µm NDOC

(e) Surface profile in experiment at 6µm NDOC

(f) Surface profile in simulation at 6µm NDOC

Figure 3-19 Comparison of surface profile in experiment and simulation at 90mm/min, 60,000rpm with different depths of cut

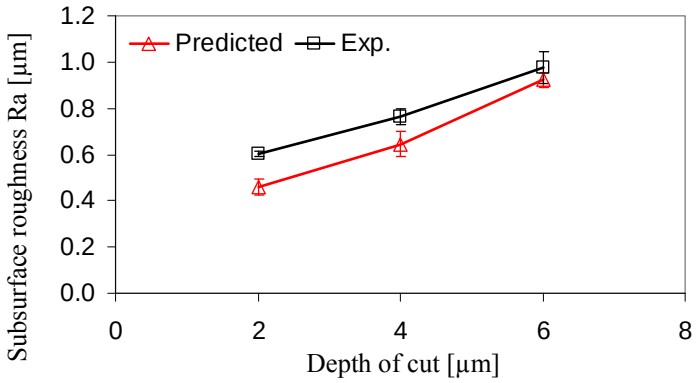

(a) Arithmetic average surface roughness (Ra)

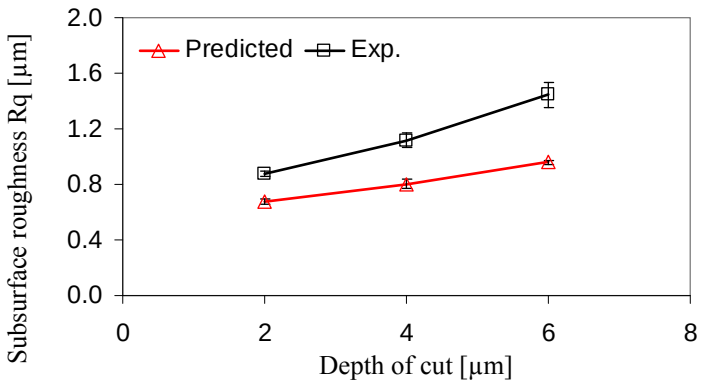

(b) Root means squared surface roughness (Rq)

Figure 3-20 Surface finish index in simulation and experimental results at different depths of cut at 90mm/min and 60,000rpm

The surface finish index: arithmetic average surface roughness (Ra) and root mean squared surface roughness (Rq) are also compared between experimental and simulated results, as shown in Figure 3-20. It is observed that the predicted arithmetic average surface roughness matches well the experimental result, while the prediction error in root mean squared surface roughness is relatively high. This could be attributed to the difference in these two surface roughness indexes. The arithmetic average surface roughness reflects the expected value of the surface profile, which is mainly influenced by the maximum surface chipping depth. However, the root mean squared surface

roughness is more a measurement of the magnitude of variation in surface profile. As shown in Figure 3-19, the actual surface profile is noisier than the simulated surface profile. This could be related to the vibration in actual grinding process, which increases variation in surface profile.

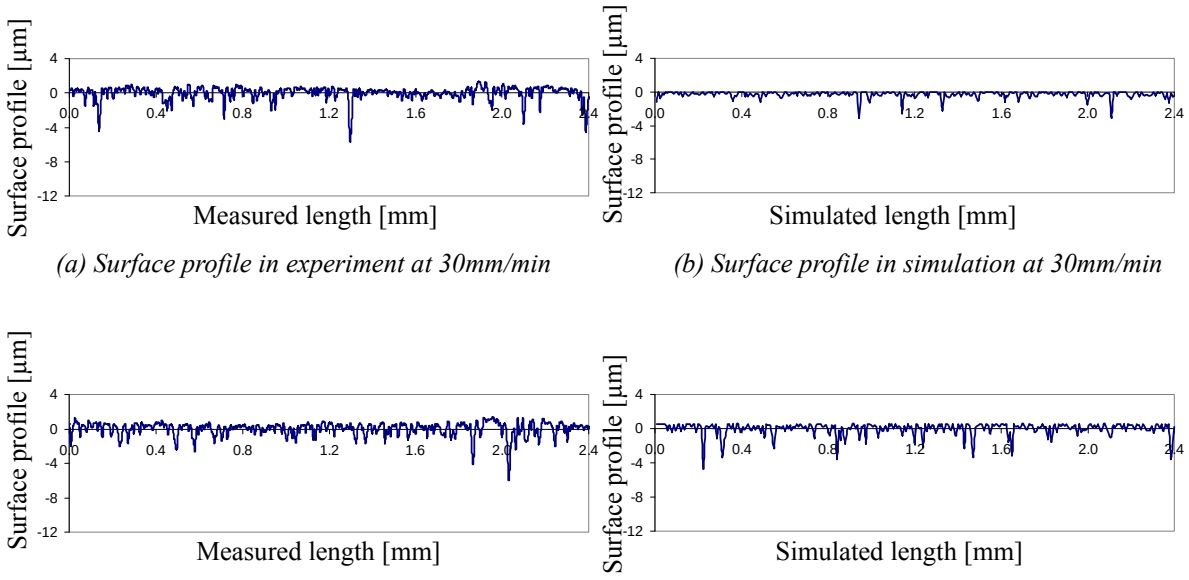

(a) Surface profile in experiment at 30mm/min

(b) Surface profile in simulation at 30mm/min

(c) Surface profile in experiment at 60mm/min

(d) Surface profile in simulation at 60mm/min

Figure 3-21 Comparison of surface profile in experiment and simulation at 4µm depth of cut, 60,000rpm at different feed rates

The simulated surface profiles are also compared with experimental result for different feed rates at 4µm depth of cut and 60,000rpm spindle speed. The corresponding experimental and simulation results are shown in Figures 3-19 (c, d) and 3-21. Similar surface chipping depth is also observed in the experimental and simulation results, which increases with feed rate. The predicted arithmetic average surface roughness (Ra) also matches well with the experimental result. For the root mean squared surface roughness,

the prediction error is relatively significant at high feed rate, while good match is observed at low feed rate: 30mm/min. This could be attributed to the low grinding vibration at low feed rate, as reflected in the smooth surface in Figure 3-21(a). This suggested that vibration in the grinding process could be the main error source for the proposed model for modeling surface finish in microgrinding of ceramic materials.

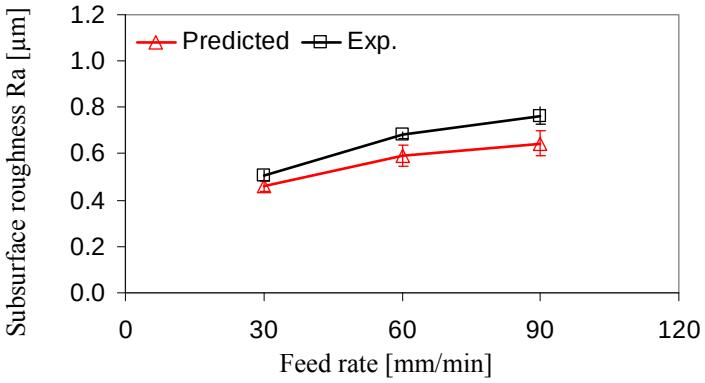

(a) Arithmetic average surface roughness (Ra)

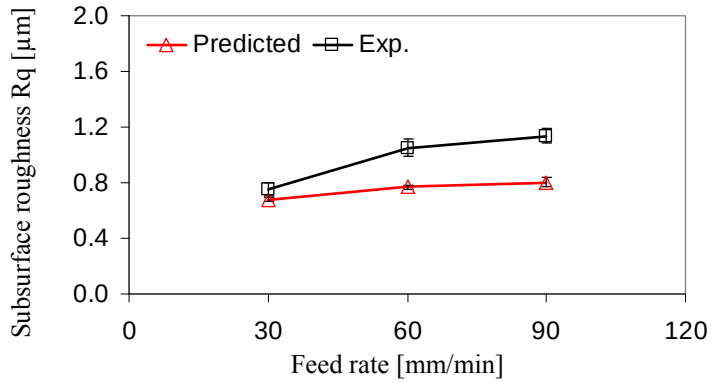

(b) Root mean squared surface roughness (Rq)

Figure 3-22 Surface finish index in simulation and experimental results at different feed rates at 4µm and 60,000rpm

3.7 Conclusion

In conclusion, this study investigates the modeling of surface generation in microgrinding of ceramic materials based on CZM based FEA. From the observation of ground surface texture in microgrinding, it is proposed to construct the surface generation in microgrinding based on trajectory analysis in ductile flow mode grinding and surface chipping depth in fracture mode grinding. The trajectory analysis is conducted based on the actual diamond protrusion on the microgrinding tool; while the surface chipping depth is predicted from the fully damaged subsurface depth in CZM based FEA, considering the flaw variation in the actual ceramic workpiece. By conducting CZM based FEA modeling for individual diamond, it is observed that there exists a critical flaw size beyond which no significant surface damage will be introduced into the workpiece for a specific grinding condition. This critical flaw value is used to distinguish the ductile flow mode grinding and fracture mode grinding in the surface generation. The predicted surface profiles are compared with the actual surface profile at different grinding conditions. It is observed that the predicted arithmetic average surface roughness matches well with the experimental result, while the error in predicting root mean squared surface roughness is relatively large. This could be attributed to the vibration in grinding process, which introduces more variation in surface profile at high feed rate. At small feed rate, when process vibration is not significant, good matching is observed in both arithmetic average surface roughness and root mean squared surface roughness.

CHAPTER 4

TOOL WEAR MECHANISM IN MICROGRINDING OF CERAMIC MATERIALS

4.1 Introduction

The significance of grinding tool wear is closely related to the precision requirement and the specific type of the grinding tool used in the process. In microgrinding, the influence of tool wear is expected to be significant, as it requires a high grinding precision to manufacture the micro-component. Moreover, as a microgrinding tool is small in profile and contains a small amount of abrasive cutting edges, its grinding performance could be easily affected by the tool topography change due to tool wear. Therefore, the grinding tool wear is not only an issue of manufacturing cost, but also one of the key limiting factors in achieving high grinding quality, including grinding accuracy and surface finish, in manufacture of ceramic micro-components.

In the past, many tool wear studies have been done in various conventional grinding processes for the tool wear mechanism, effects and status monitoring (Tao et al., 1997, Li et al., 1997, Li et al., 1996). However, a typical microgrinding tool is smaller than one millimeter in diameter, and its surface speed is very small (about 2m/s) in comparison to the conventional grinding (30 ~ 60 m/s). Therefore, it is questionable to

apply the knowledge gained in the conventional grinding directly to the microgrinding.

This study aims to study the tool wear in microgrinding of ceramic materials. By tracking individual diamond life cycles on a microgrinding tool, this study investigates the detail tool wear mechanisms in microgrinding of ceramic materials. By examining the surface generations in the tool wear process, the specific influences of the tool wear mechanisms are discussed in microgrinding. Based on these findings, the selection of proper coolant condition is discussed for tool life improvement in microgrinding. By analyzing the various process signals in microgrinding, including grinding force, grinding system vibration, acoustic emission signals and spindle load, this study also investigates the proper process signal selection for microgrinding tool wear monitoring.

4.2 Literature Review

The wear process of the grinding tool is very complex, as it usually involves both tool volume loss and the dulling of the abrasive grains, which is more a micro-level topography change than tool profile change. Therefore, it is important to understand the detail tool wear mechanisms to design a grinding process for the desired tool life and grinding quality.

It is generally accepted that there are three main tool wear mechanisms in the grinding process: attrition wear, abrasive grain fracture and bonding fracture (Malkin, 1989, Shaw, 1996). As shown in Figure 4-1(B), attrition wear refers to the dulling of the abrasive grains and the growth of wear-flats. Depending on the workpiece materials, the coolant condition and the tool properties, the attrition wear could involve both chemical

and mechanical interactions. Chemical effects are more dominant when the abrasive grain is much harder than the workpiece material, and they tend to occur at an elevated temperature in the grinding zone among the workpiece material, the abrasive grains, the surrounding atmosphere and the grinding fluid for coolant (Malkin, 1989). For abrasive grains that are made of diamonds, the attrition wear can be initiated by thermal load during grinding, which will result in diamond graphitization (Marinescu et al., 1998). Aside from the thermal and chemical effects, high mechanical impacts will also promote the attrition wear due to the abrasion on the abrasive grains.

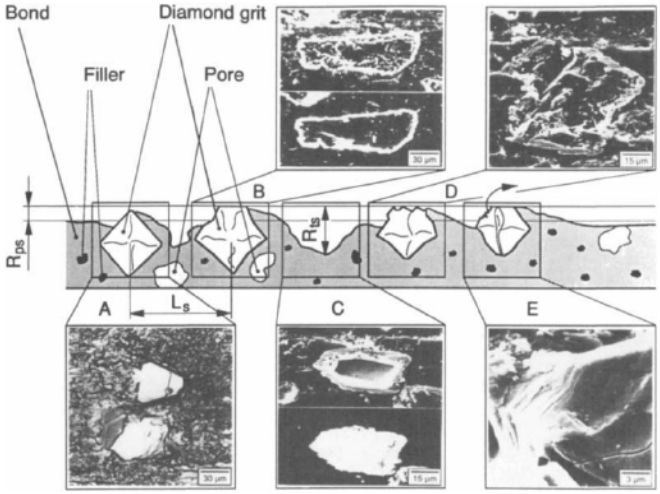

Figure 4-1 Tool wear mechanisms for the diamond grinding tool (Marinescu et al., 1998)

The abrasive grain fracture usually happens when they are undertaken high mechanical impacts. For diamond abrasive grains, these mechanical impacts will fracture the grain and form a secondary cutting edge (Figure 4-1(E)). Some diamonds are

relatively rigid and shaped like blocks. In this case, under a high mechanical impact, they might only partially fracture and create several smaller cutting edges (Figure 4-1(D)).

The fracture of the bonding material can cause the pullout of the abrasive grain (Figure 4-1(C)), it occurs when the grinding force on the abrasive grains is larger than the retention force provided by the bonding material, which is also related to the abrasive grain size, the particular bonding materials and the tool preparation process. For example, as the abrasive grains are more fragile with large grit size, bonding fracture is more likely to happen to the fine-grit grinding tool. Some studies suggested that bonding fractures are likely to happen in the initial grinding process, and this is mainly caused by mechanical damage introduced in the bonding materials during the tool conditioning process (Marinescu et al., 1998). As the grinding process becomes stable, the bonding fracture can also happen due to the different wear rates in the bonding materials and abrasive grains. When the bonding material wears faster than the abrasive grains, the abrasive grains tend to protrude higher and higher as the tool wears. Eventually, there are insufficient bonding materials to hold the abrasive grain, and the bonding fracture will happen and cause the abrasive pullout (Chen et al, 1998).

In order to determine the grinding tool wear mechanism, various techniques, including the direct inspection, the imprint technique (Liao et al., 2000) and the grinding debris analysis (Malkin, 1989), have been developed for the conventional grinding process. The direct inspection technique requires taking the microscope picture of the tool topography. By comparing the abrasive cutting edge profile change, it can determine the detail tool wear mechanism in the grinding process, but its efficiency is low when a large amount of abrasive grains requires inspection. The imprint technique captures the

grinding tool profile by pressing the grinding tool against a soft metal sheet, such as lead (Liao et al., 2000). By comparing the imprints at different tool wear stages, the grinding tool wear mechanism can be identified. However, as an indirect technique, the accuracy of the imprint could be influenced by several factors in the grinding tool, such as the porosity of the bonding material, the adhered grinding debris and the size of abrasive grains. Therefore, this imprint technique is more suitable for grinding tools with large grit size. The grinding debris analysis can identify the grinding tool wear mechanism by studying the composition in the grinding debris. This approach is developed based on the fact that the grinding debris are made of workpiece materials, abrasive grains and bonding materials, and their composition can approximately reflect the dominant tool wear mechanism (Malkin, 1989). However, it is difficult to apply this approach to microgrinding, as it only produces a very small amount of grinding debris.

Therefore, the direct inspection is most suitable for studying the microgrinding tool wear mechanism. Thanks to its small tool profile, all the abrasive grains on a microgrinding tool can be easily measured by a two-dimensional microscope or a three-dimensional white light interferometer. This enables a close tracking of individual abrasive grain wear process for the tool wear mechanisms. By using a similar approach, early studies on microgrinding tool wear have identified that the diamond pullout is the dominant tool wear mechanism for the electroplated microgrinding tool (Yin et al. 2003, Onikura et al. 2003). However, very few studies have investigated the tool wear mechanism of the metal-bonded microgrinding tool. As it has diamond mix inside, its tool wear process is expected to be different from the electroplated microgrinding tool due to the possible diamond protrusions.

In addition, as a new manufacturing process, very few studies have been done to explore the patterns of the process signals in microgrinding of ceramic materials, which are important for the tool wear monitoring in the practical application. In the past, various process signals have been investigated in the grinding process for tool wear monitoring, such as grinding force (Kwak et al., 2004), spindle load (Byrne et al., 1995), acoustic emission (AE) (Hwang et al., 2000), sound (Hosokawa et al., 2004) and structure vibration (Lezanski, 2001). Among these process signals, grinding force is always considered as the most important one for indirect and continuous monitoring of the grinding tool wear, as it generally increases monotonically as the tool wears. Spindle load signal has also been used for grinding tool wear monitoring, because the specific grinding energy will increase as the tool wears, the tool wear status can be monitored based on the spindle load, although it might have a low-pass filter characteristic due to the inert masses in a grinding system (Byrne et al., 1995). AE signal is widely used in tool condition monitoring for its fast response and high sensitivity. By attaching AE sensors directly onto the grinding tools, some studies indicate that it is possible to characterize the grinding tool profile change in the tool preparation process (Karpuschewski et al. 2000). However, despite these many studies in conventional grinding, the understanding of the process signals patterns is very limited in the microgrinding tool wear. To fulfill these gaps, it is necessary to conduct a comprehensive study in both tool wear mechanism and process signal patterns in microgrinding of ceramic materials.

4.3 Microgrinding Tool Wear Mechanism

4.3.1 Experimental procedure

A meso-scale grinding system, as shown in Figure 2-5, is used to conduct the microgrinding tool wear study. Its positioning accuracy, load capacity and spindle runout have been discussed in detail in the previous section (2.4). MgO partially stabilized Zirconia was used as the workpiece in the tool wear study. Its material properties are summarized in Table 4-1. Before the experiments, the zirconia workpiece was flattened by a ∅7.8 mm, 120 grit size metal-bonded diamond wheels at 70,000rpm.

Table 4-1 Properties of the zirconia workpiece

Property	
Elastic modulus [GPa]	200
Poisson's ratio	0.30
Hardness [GPa]	11.8
Tensile strength [MPa]	410
Fracture toughness K_{IC} [MPa·m$^{1/2}$]	8 -11

In the experiment, a series of micro-channels, which are 6.5mm in length, 0.85mm in width and 20μm in total depth, were ground onto the ceramic workpieces at 2μm depth of cut, 10mm/min feed rate and 60,000rpm spindle speed. At selected intervals, the microgrinding tool was inspected by Scanning Electron Microscopy (SEM) for the topography change. The surface roughness of the ground channels were measured by a white light interferometer in a sample surface of 1.5 × 0.3mm^2. The measurements

were repeated at three different locations in each channel for the average value.

4.3.2 Life cycle of diamonds in microgrinding

As shown in Figure 4-2, the detail diamond wear mechanisms can be identified by comparing the diamond profile changes at different tool wear stages. Different wear mechanisms, including diamond fracture, attrition wear, bonding material erosion and fracture, were observed in microgrinding of ceramic materials. Due to the end grinding configuration, there is a significant corner wear on the tool edge.

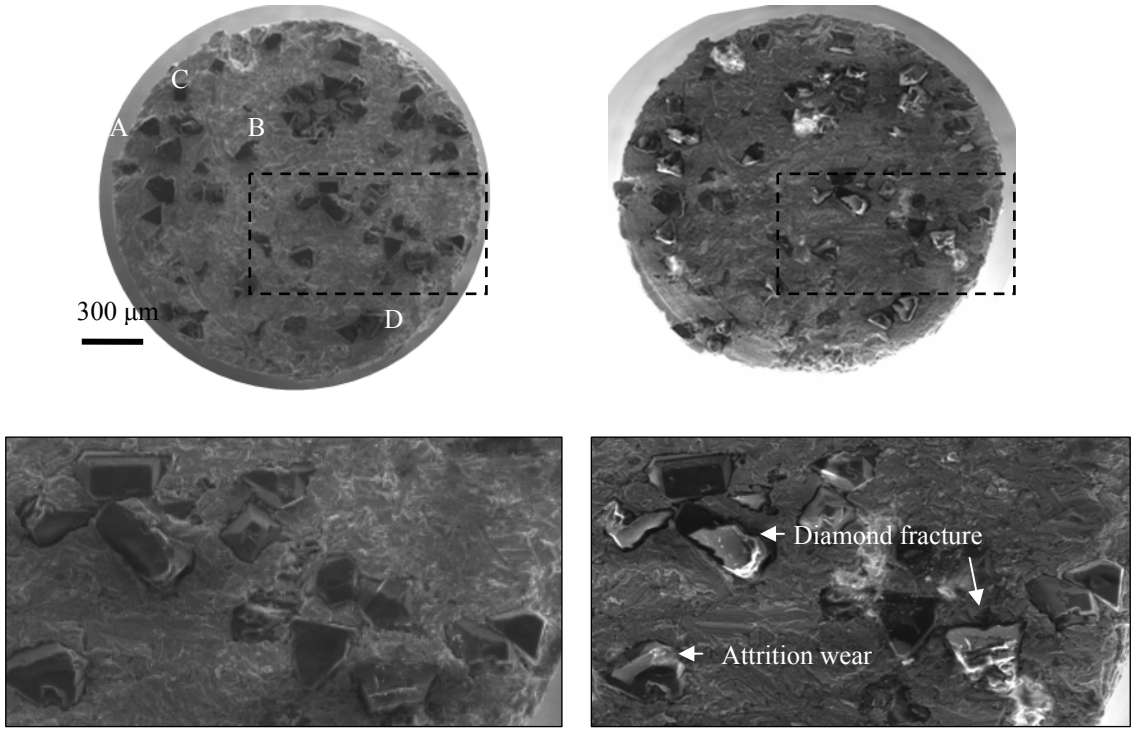

(a) After grinding one channel *(b) After grinding seven channel*

Figure 4-2 Comparison of the diamond profile for the detail tool wear mechanism

To quantify the different tool wear mechanisms in microgrinding, the wear mechanisms of every diamond were tracked and counted in the grinding process. As shown in Figures 4-2 and 4-3, diamonds could experience different wear mechanisms through their life cycles. For example, Diamond A first fractured at the corner after grinding two channels. Then, attrition wear caused some flat area. After grinding thirteen channels, it fractured again. After grinding nineteen channels, both the attrition wear and the fracture regions are visible on the diamond. However, Diamond B and D have only experienced attrition wear, and Diamond C mainly experienced fracture. Based on these observations, the tool wear mechanisms in microgrinding were grouped into attrition wear, fracture, attrition and fracture combined wear and diamond pullout.

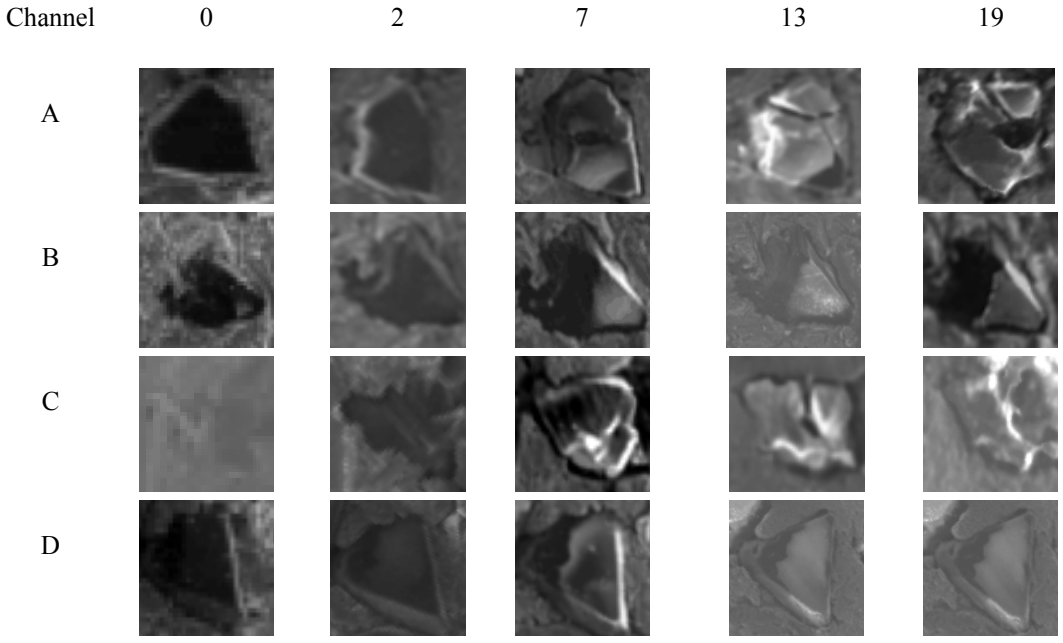

Figure 4-3 Life cycles of the diamonds in microgrinding

The total amounts of the diamonds worn out for different mechanisms at selected tool wear stages are shown in Figure 4-4. During the initial tool wear stage (channel 1), the microgrinding tool mainly experienced the diamond pullout. This could be related to the weakening of bonding materials during truing and dressing operations. After this period, diamond fracture increases (during channels 2~5). After this transition stage, the tool wear became relatively stable, and the attrition wear becomes the dominant wear mechanism. By further conducting microgrinding with the worn-out tool, it was observed that the total amount of diamonds increased. This was caused by protrusion of fresh diamonds when bonding materials were eroded away. Cumulatively, about 20% diamonds were newly protruded ones after nineteen channels.

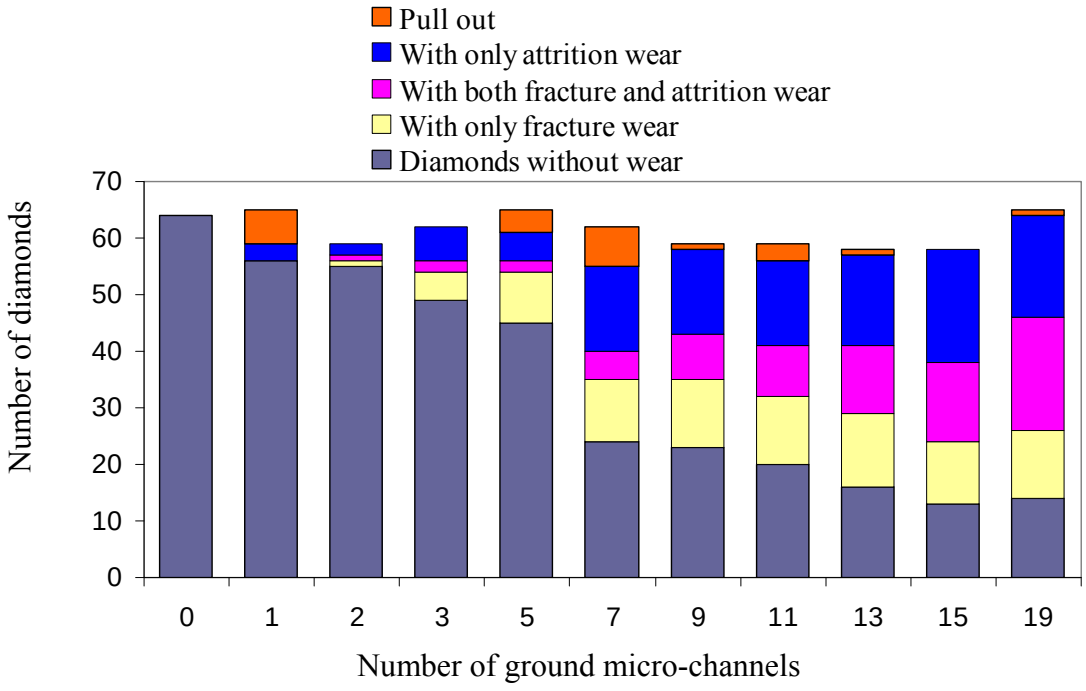

Figure 4-4 Tool wear mechanism in microgrinding of ceramic materials

Different from the side grinding process, in which the tool wear across the grinding tool is always uniform, the tool wear in end grinding is often non-uniform, since the surface speed varies from the tool center to its edge. To explore this regional effect in microgrinding, the diamonds are grouped into inner and outer region ones by half of the tool radius. The composition of the tool wear mechanisms are as shown in Figure 4-5. It can be observed that there are more diamond fractures in the outer region than the inner region. As these diamonds were responsible for cutting majority of the material, they are expected to take a higher mechanical impact. By contrast, the attrition wear is more dominant in the inner region. It is expected that these diamond were involved more in sliding than cutting, and this will promotes attrition wear.

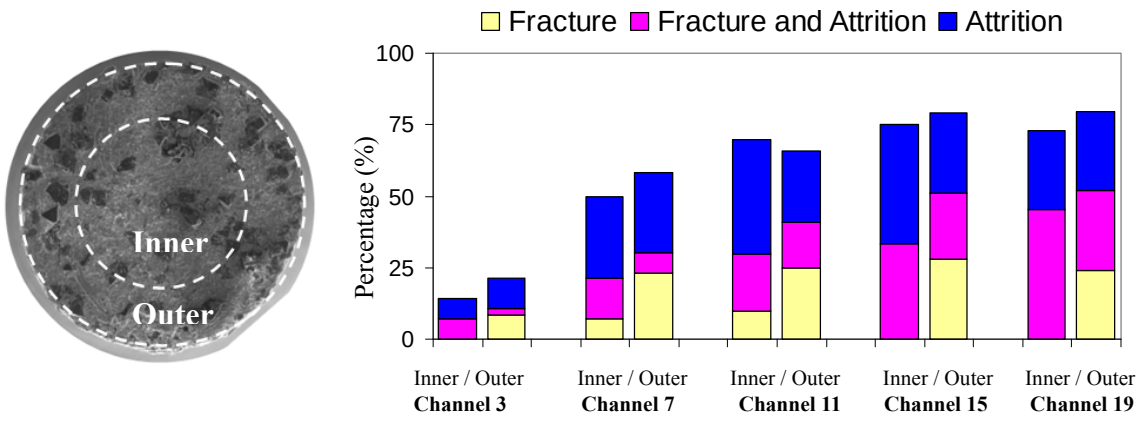

Figure 4-5 Effect of diamond location on their wear mechanisms

4.3.3 Influence of tool wear on the surface finish

The surface finish is the key quality index in grinding, and it is usually closely related to tool wear status (Malkin, 1989). In this study, the changes in surface generation were inspected by SEM and a white light interferometer, as shown in Figure 4-6. As the dominant tool wear mechanism varies in microgrinding, ground surface texture also changes correspondingly. During the initial tool wear stage (channels 1~5), clear cutting trajectories with a large spacing are observed on the ground surface, and this suggested a relative effective material removal and sharpness of the diamonds. As the tool wears, finer cutting trajectories were observed on the ground surface (channel 9). This could be related to the increasing diamond fracture, which has produced many fine secondary cutting edges. When the tool got further worn out (channels 13-15), more surface damage were observed on the ground surface. This is related to the dominant attrition wear on the microgrinding tool, which has caused a much ineffective material removal. By conducting microgrinding with the worn out tool, it was observed that surface fracture decreases as tool wears, and this is related to the new diamonds protrusion on the microgrinding tool, which has improved material removal.

The surface roughness (Ra) of the micro-channels is measured by a white light interferometer as shown in Figures 4-7. During the initial tool wear stage, it was observed that surface roughness is decreasing, and this could be related to increasing fine cutting edges on the microgrinding tool due to diamond fracture. As tool got severely worn out due to attrition wear, surface roughness increased sharply. This could be related the surface fracture from ineffective material removal, and it promotes the generation of surface fracture. As more fresh diamonds protruded, surface roughness decreased due to

the improved material removal. Through this tool wear study, it was revealed the actual tool wear mechanism has a direct influence on the surface quality in microgrinding. The diamond fracture tends to improve surface finish in microgrinding, while attrition wear will increase surface damage and result in poor surface finish.

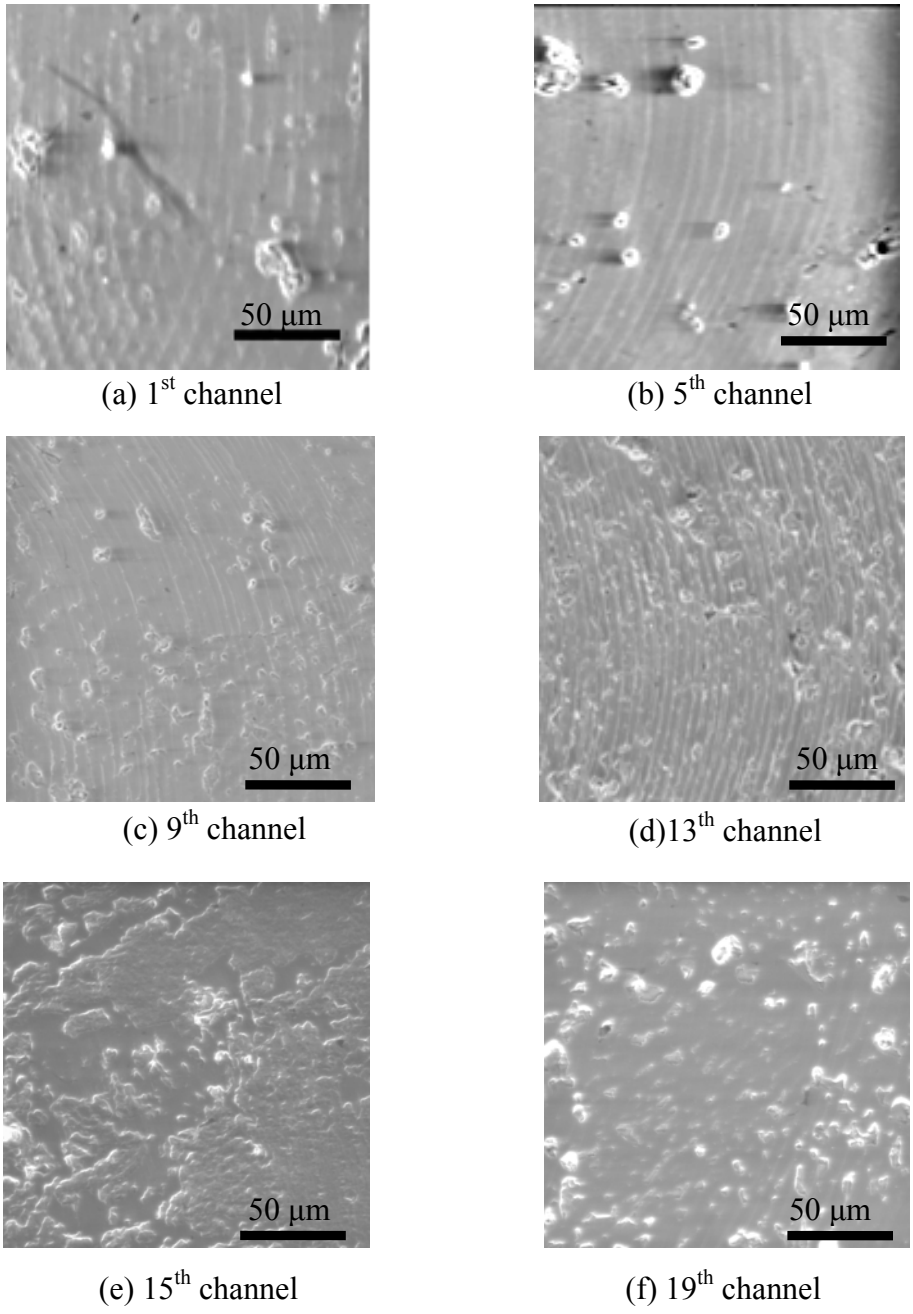

(a) 1st channel (b) 5th channel

(c) 9th channel (d)13th channel

(e) 15th channel (f) 19th channel

Figure 4-6 Variation of surface texture as the tool wears in microgrinding

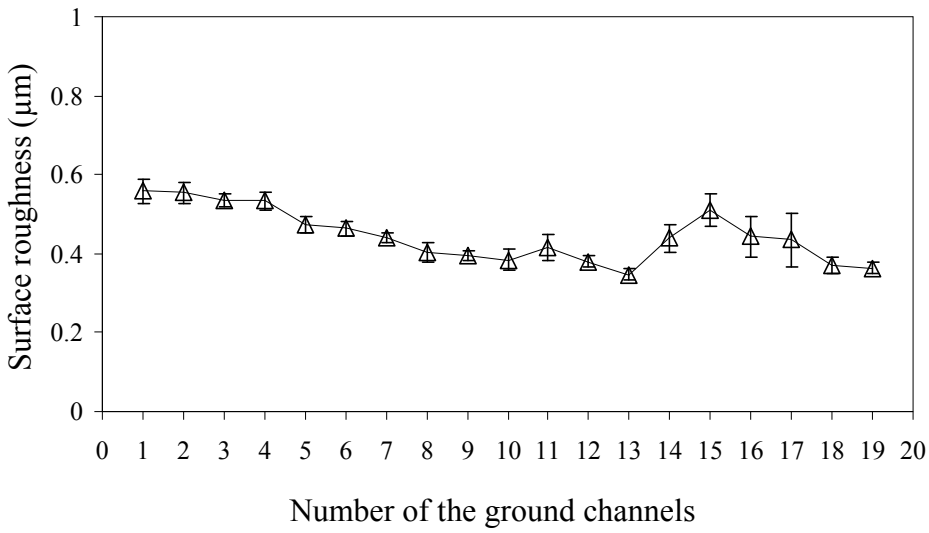

Figure 4-7 Surface roughness of the micro-channels as the tool wears

4.3.4 Influence of coolant on microgrinding tool wear

Based on the observed tool wear mechanism in the microgrinding, it is interesting to know how the coolant conditions could affect its tool wear. Most grinding fluids can be categorized as cutting oils and soluble oils. Cutting oils for grinding are mineral-oil-based fluids with additions of fatty materials for lubrications and wettability, and sulfur and/or chlorine for wear reduction. Soluble oils are water-based fluids contained oil emulsions and some ingredients which may include fatty materials, soaps, chloride for lubrication, surfactants for wetting and rust inhibitors. In the conventional grinding process, cutting oils are generally found to be better lubricants than soluble oils, as evidenced by higher G-ratio. Early studies suggested that this could be related to presence of water in the soluble oils, which have an adverse effect on the strength of the abrasive grain and the binder, thereby promoting the fracture wear with water-based

fluids (Malkin, 1989). However, the water based soluble oils has the advantage of control temperature in the grinding process, which would not only reduce the thermal damage in the workpiece but also the possible attrition wear at an elevated temperature.

In order to determine the proper coolant condition for microgrinding of ceramic materials, different coolant conditions, including water coolant, cutting oil coolant and soluble oil coolant (8% oil in water), were applied to the microgrinding. To assess their influence on the tool wear, the microgrinding tool profile was imprinted by grinding a flattened plastic plate before and after the grinding operation (as shown in Figure 4-8). These imprint profiles are then measured by a profilometer for the actual tool wear. The grinding was conducted at 3μm depth of cut, 30mm/min feed rate and 60,000rpm spindle speed for a total material removal of 1.66 mm^3 in grinding zirconia.

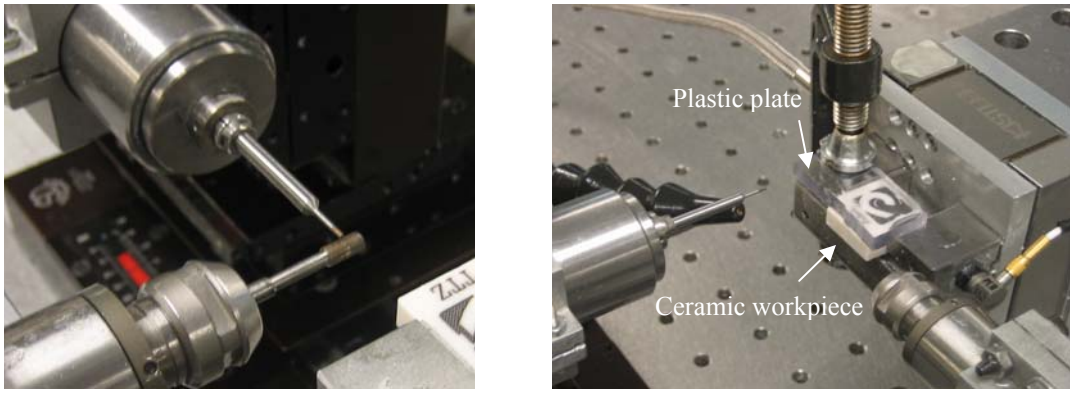

(a) Truing operation (b) Imprint for tool profile

Figure 4-8 Experimental procedure for measuring microgrinding tool wear

By comparing the tool profile changes in different coolant condition (Figures 4-9~4-11), it can be observed the water coolant and soluble oil coolant can reduce the tool

wear in microgrinding of ceramic materials. This could be related to the better cooling effects provided by the water based coolant in microgrinding, which has hindered the attrition wear of the diamond due to high temperature in the grinding zone.

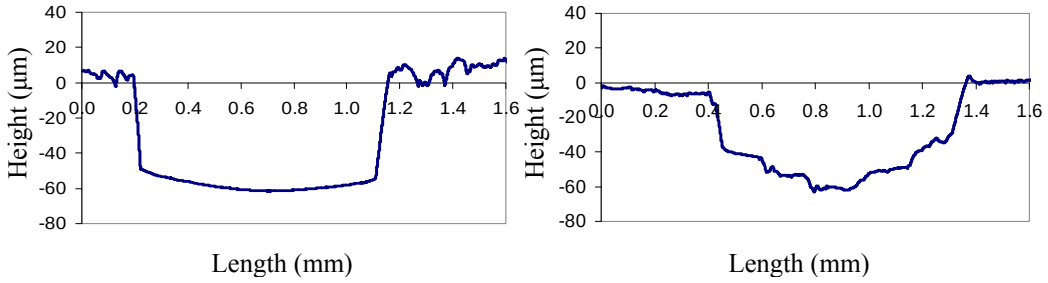

(a) Before grinding (b) After grinding

Figure 4-9 Microgrinding tool wear with water coolant

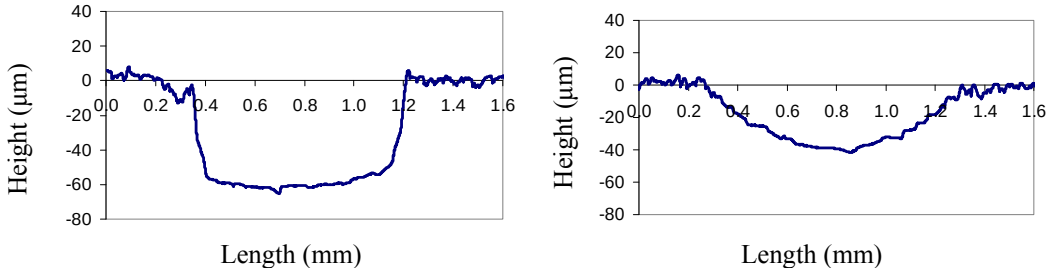

(a) Before grinding (b) After grinding

Figure 4-10 Microgrinding tool wear with cutting oil coolant

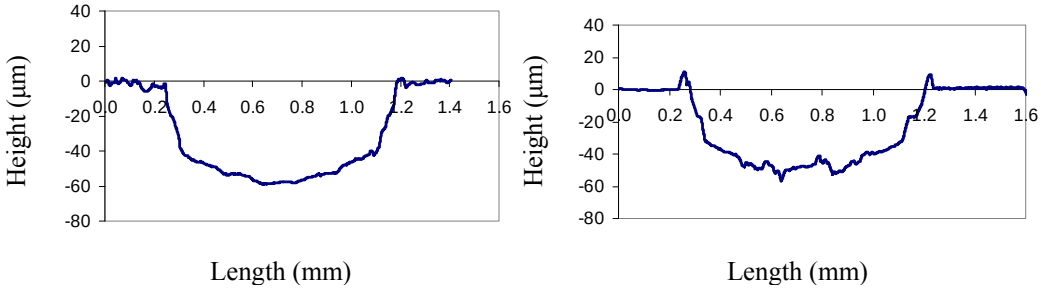

(a) Before grinding (b) After grinding

Figure 4-11 Microgrinding tool wear with soluble oil coolant

4.4 Patterns of Process Signals in Microgrinding

4.4.1 Collection of process signals

In order to understand the patterns of the process signals in microgrinding of ceramic materials, the grinding force, the grinding system vibration, the AE signals and the spindle load were monitored by a dynamometer, two accelerometers, an AE sensor and a spindle load meter in the tool wear process, as shown in Figure 4-12(a). The dynamometer (Kistler 9256C1) has a threshold value of 0.002N. Two accelerometers (PCB ICP-typed 352 A21) are used to measure vibrations on the workpiece and the fixture. Their working frequency is 1~10,000Hz. The spindle load meter is integrated inside the spindle controller (NSK NE147-800). A Physical Acoustics Corp. AE sensor (Micro80) is used to collect the AE signal on the workpiece. Its working frequency is 170~1,000KHz, and the AE signal is collected at 5MHz sampling rate by the oscilloscope. The grinding force, the spindle load, the acceleration on the workpiece and the fixture are sampled at 17,500Hz.

A series of micro-channels were ground onto one single workpiece, as shown in Figure 4-12(b). The microgrinding was conducted at 3μm depth of cut, 30mm/min feed rate and 60,000rpm spindle speed. Seven grinding passes were applied to each micro-channel for a total depth of cut of 21μm. As the microgrinding tool wears, it is expected these micro-channel will decrease in the actual depth of cut, not only due to tool profile change, suggested by Figure 4-13, but also because of the increasing grinding force, which will cause more tool deflection. The actual grinding depths were measured by a white light interferometer at 0.1nm vertical resolution and 0.825μm horizontal resolution. As shown in Figure 4-14, the micro-channels become shallower due to the tool wear.

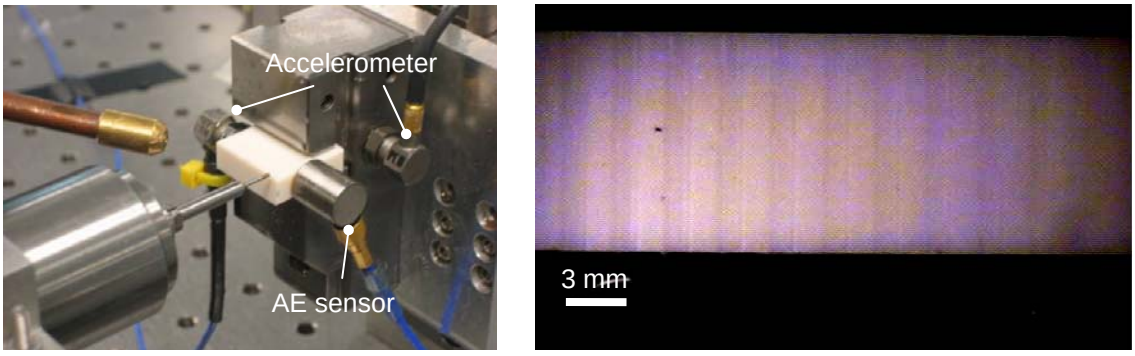

(a) Grinding configuration *(b) Ground micro-channels*

Figure 4-12 Process signals collection in the microgrinding tool wear study

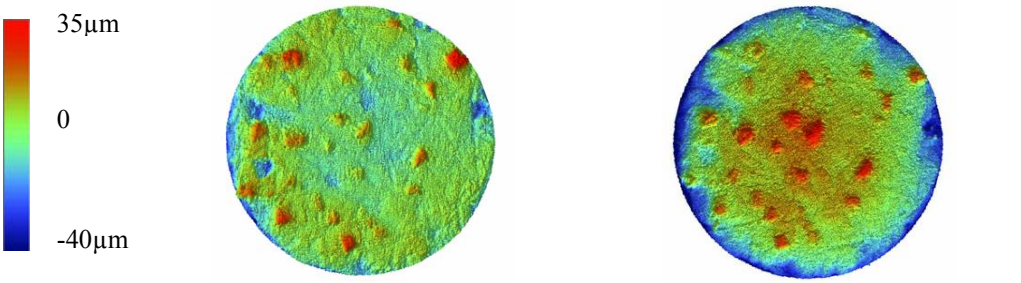

(a) Tool before grinding *(b) Tool after grinding in 11th channel*

Figure 4-13 Microgrinding tool topography change as the tool wears

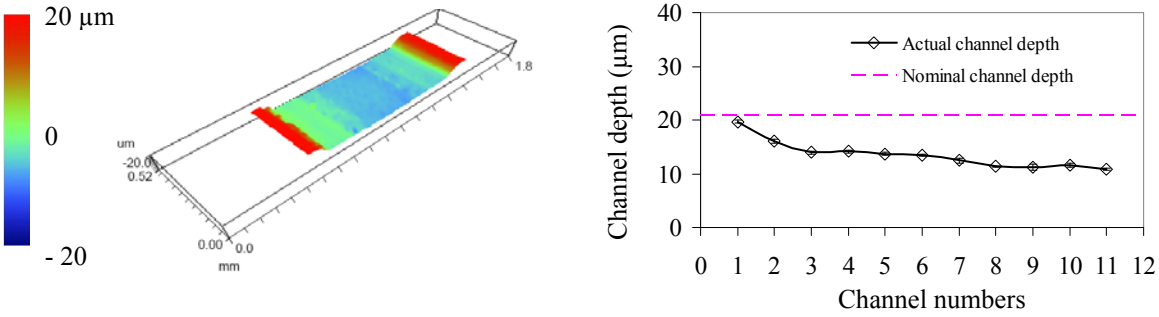

(a) 3D measurement of the channel *(b) Effect of tool wear on grinding accuracy*

Figure 4-14 Measurement of actual depth for the micro-channels

4.4.2 Process signals in a microgrinding tool wear process

As shown in Figure 4-15, in addition to the tool wear influence, the grinding force will also increase as the microgrinding tool machines deep into the workpiece. This is related to the low tool stiffness in microgrinding, which causes a significant tool deflection. As the tool grinds deeper into workpiece, these tool deflections accumulated and added to the actual depth of cut, and consequently, increases the grinding force. This increasing trend, which is caused by both tool wear and tool deflection, is also observed in the average and root mean square (RMS) value of the grinding force in normal, feed and tangential directions, as shown in Figure 4-16.

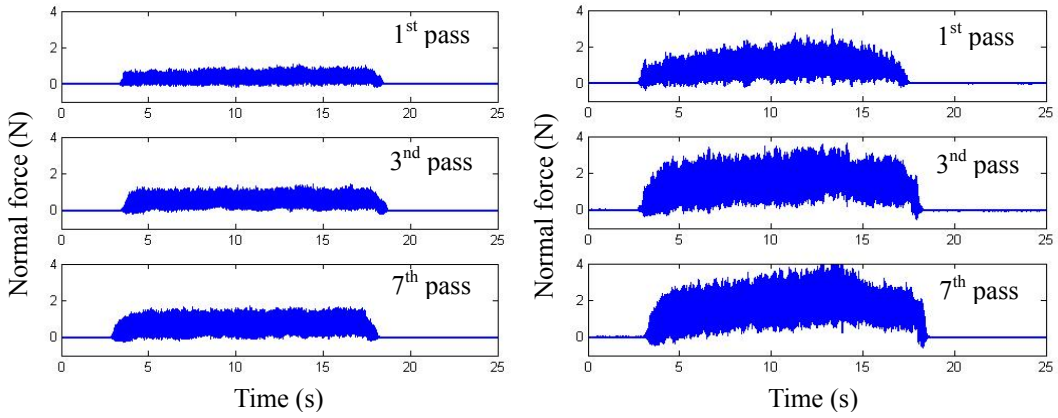

(a) Force signal in 1st channel *(b) Force signal in 11th channel*

Figure 4-15 Normal forces signals in microgrinding

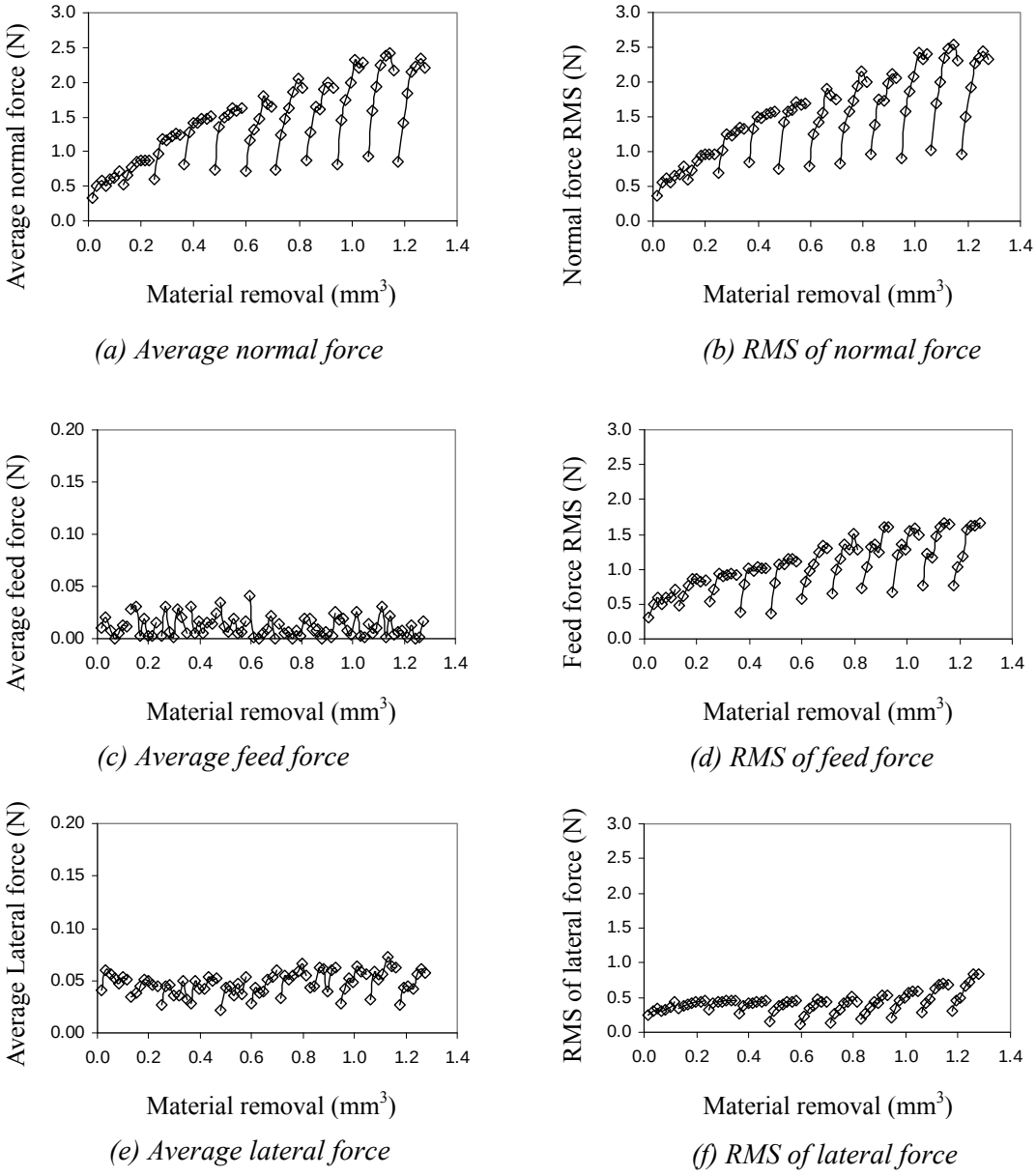

Figure 4-16 Statistical values of force signals vs. material removal

The average and root mean square (RMS) values of the workpiece and fixture vibration, AE signals and spindle load are also analyzed in this tool wear study, as shown in Figure 4-17. As statistical process signals, they also reflect the characteristic trends in

the time domain, and they follow a similar increasing trend as the grinding force. Different from conventional grinding, the spindle load in microgrinding only displays small deviation as tool wears. This is mainly due to the small scale of microgrinding, which only consumes a very small amount of grinding energy. Hence, the major characteristic of the process signals in microgrinding lies in its low tool stiffness, which has a significant influence on the grinding force signals varying with the ground features.

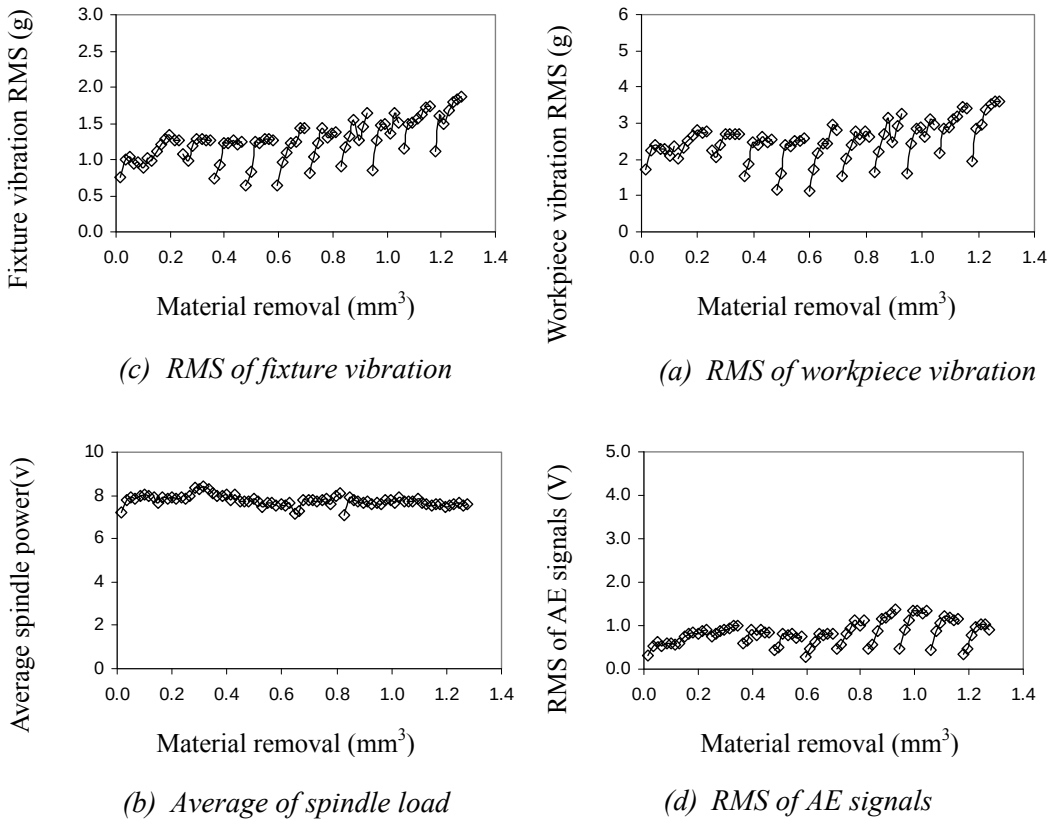

(c) RMS of fixture vibration

(a) RMS of workpiece vibration

(b) Average of spindle load

(d) RMS of AE signals

Figure 4-17 Statistical values of other process signals vs. material removal

4.5 Conclusion

This study investigates the tool wear mechanism in microgrinding of ceramic materials with metal-bonded microgrinding tools. By tracking the wear process of every diamond on a microgrinding tool, it was observed that individual diamonds would experience different wear mechanisms through their life cycles, and these wear mechanisms have a specific influence on the surface generation. By applying different types of coolants, it was observed that water based coolant can reduce tool wear in the microgrinding. This could be related to the better cooling effect of the water based coolant, which hinders the attrition wear. By monitoring the various process signals in microgrinding, it was observed that both tool wear and tool deflection have influences on the various process signals.

CHAPTER 5

SUMMARY AND CONTRIBUTIONS

5.1 Summary

This research contributes to the understanding of ceramic microgrinding process, with emphasis on force prediction, surface generation modeling and tool wear mechanism study.

5.1.1 Force Modeling and Prediction in Microgrinding of Ceramic Materials by Cohesive Zone Based Finite Element Method

Grinding force is crucial for the grinding accuracy and surface generation in the microgrinding process. Based on the cohesive zone finite element analysis, this study investigates grinding force modeling and prediction in microgrinding of ceramic materials. The chip generation is explicitly simulated in this study based on actual diamond profiles. The predicted grinding force matches well with the experimental result at different depths of cut and feed rates. It was observed that the low microgrinding tool stiffness and ceramic-diamond contact properties have a significant influence on the force

prediction accuracy.

5.1.2 Numerical Modeling of Surface Generation in Microgrinding of Ceramic Materials

The numerical simulation of surface generation is investigated in microgrinding of ceramic materials. Surface generation from both ductile grinding and surface chipping is modeled in this process. The surface generation from ductile mode grinding is modeled by trajectory analysis. The surface generation from surface chipping is estimated from the subsurface damage depth in microgrinding from cohesive zone based FEA simulation. The simulation result matches well with the experimental result at different feed rates and depths of cut. Relatively large prediction error is observed in root mean squared surface roughness. This could be related to vibration in grinding process at high feed rate.

5.1.3 Tool Wear Mechanism in Microgrinding of Ceramic Materials

The microgrinding tool wear mechanism was investigated in this study. Each diamond on a microgrinding tool was tracked in this study to understand the detail wear mechanisms. As the microgrinding tool wore out, it was observed that different wear mechanisms were involved in the tool life cycle, and they have specific influences on the surface generation. At initial tool wear stage, it was observed that the diamond fracture is significant. During the steady wear process, it was observed that attrition wear is more dominant. By applying water-based coolant, the tool wear can be reduced in

microgrinding of ceramic materials. In addition, it was observed that low stiffness of the microgrinding tool has a significant influence on the process signals in microgrinding, and this is mainly related to tool deflection in this process.

5.2 Contributions

The major contributions of the dissertation may be summarized as follows.

1. This study demonstrates the feasibility of force prediction in microgrinding of ceramic materials by CZM based FEA. The major challenge for accurate force prediction in machining ceramic materials lies in the difficulty to account for the highly nonlinear ceramic chip generation process, which involves both ductile flow and micro-level fracture. The application of the CZM based FEA not only enables an explicit modeling of the micro-level fracture, but also avoids the singularity problem in modeling fracture by conventional FEA. In addition, it is identified that the tool stiffness, ceramic-diamond contact properties and chip profile model are important for the force prediction accuracy in microgrinding.

2. This study addressed the influence of both ductile flow and surface chipping on the surface generation in microgrinding of ceramic materials. The surface chipping profile is estimated from the fully-damaged subsurface depth in microgrinding of ceramic materials. By developing a hybrid surface generation model, this study demonstrates that the surface roughness can be accurately predicted in microgrinding of ceramic materials.

3. By tracking the wear process of individual diamonds on a microgrinding tool, this study investigates the diamond wear mechanisms and their life cycle in microgrinding of ceramic materials. By inspecting the detail surface texture produced by microgrinding, the specific influence of the tool wear mechanism is addressed in this study. In addition, it was observed that water based coolant can improve the tool life in microgrinding of ceramic materials. The low stiffness of the microgrinding tool has a significant influence on the process signals in the tool wear process.

5.3 Recommendations for the Future Work

The dissertation investigated microgrinding of ceramic materials in the force modeling and prediction, surface generation and tool wear mechanism study. The following topics are recommended for the future work.

5.3.1 Modeling of dynamic microgrinding process

Based on the force modeling and prediction investigated in the previous chapter, it is possible to develop a dynamic model for the microgrinding process. By considering the vibration effect, this dynamic process model could improve the accuracy in the force prediction and surface generation modeling in microgrinding of ceramic materials at high depths of cut and feed rates. However, in order to build a dynamic model, it also requires

precision characterization of the dynamic response of the microgrinding tool system.

Conventionally, the dynamics response of a system can be characterized by a Transfer Function (TF), which is derived from either finite element analysis (FEA) or experimental modal analysis (EMA). EMA usually provides more accurate TF than FEA, but it requires impact tests to measure the dynamic response. This is not suitable for a microgrinding tool due to its miniature profile. To solve this problem, it is recommended the future study to utilize the receptance coupling method to capture the dynamic response of a microgrinding tool. This method allows calculation of the resultant dynamic response of a system from combined FEA and EMA. The FEA study can be apply to the microgrinding tool for its dynamic properties, and impact tests can be applied to the rest of the system. With this advantage, the actual response at the microgrinding tool tip can be determined, and this allows modeling the microgrinding process from a dynamic perspective.

Moreover, as the metal-bonded grinding tool contains not only bonding materials, but also diamond grains and porosities, it is interesting to know how their size, density, distribution will affect the tool dynamics and balancing in microgrinding. This study can be conducted by numerical simulations as well as experiments through measuring tool composition. The findings from this study will improve the design of the microgrinding tool for better vibration properties and the desired dynamic response.

5.3.2 Study of microgrinding tool dressing by electrical discharge machining

The dressing process exposes the abrasive grains on the grinding tool by

removing the bonding material, and it is critical for the overall tool life and the grinding quality. In the past, very few studies have been published in the microgrinding tool dressing, and this has hindered the application of microgrinding in industry. In the future work, it is recommended to investigate the microgrinding tool dressing by using electrical discharge machining for better dressing efficiency and quality. In conventional grinding process, electrical discharge machining has proven an effective method to dress the metal-bonded grinding tools. As the bonding materials are mainly removed by vaporization in high temperature in the electrical discharging, high form accuracy can be maintained in this dressing process. This is particular suitable for the microgrinding tool, which has a low tool stiffness. However, the high temperature in the electrical discharge machining could also cause some thermal effect in the microgrinding tool, such as degradation in the abrasive grains or the bonding materials. These thermal effects could be more significant in a microgrinding tool due to its small profile. Hence, in the future work, it is recommended to study the detail correlations among the electrical discharging condition, the grinding performance and the microgrinding tool life for optimal selection of the dressing condition. The finding from this study could provide useful guidance in applying electrical charge machining in the microgrinding tool dressing.

5.3.3 Study of subsurface damage in microgrinding of ceramic materials

In the previous chapter, the surface generation has been modeled by considering the surface chipping in microgrinding of ceramic materials. In addition to the surface quality, the strengths of the ground micro-components are also critical in various

applications. In grinding of ceramic materials, the strength of the ground components can be influenced by the subsurface damage introduced in the grinding process due to the micro-level fracture related material removal. Hence, it is necessary to characterize these subsurface damages when the ground components are used for high reliability applications. By understanding the scale, the level and the mechanism of these subsurface damages, it is possible to optimize the microgrinding process to reduce the subsurface damage.

In the future work, it is recommended to use design of experiment method to determine the major factors that influence strength of the ground ceramic components in the microgrinding. By determining the major factors that affect the strength of the ceramic micro-components, detail study can be conducted to inspect the possible crack generations inside the workpiece for the degradation mechanism. The findings from this study will provide useful guidance in grinding condition selection in ceramic microgrinding to reduce the subsurface damage.

APPENDIX

APPENDIX

Derivation of Cohesive Zone Based Finite Element Model

In cohesive zone based finite element analysis, the continuum is characterized by two constitutive relations: a volumetric constitutive law that relates stress and strain; and cohesive constitutive relation between the tractions and displacement jumps across the specified set of cohesive surfaces, which are interspersed through the continuum.

The principle of virtual work for a deformable body can be used for deriving the cohesive zone based finite element model. For a finite deformable body, with length of dx, volume of dV, under body force f and traction of F_A and F_B, as shown in Figure A-1, the net work done by the body force can be calculated by Equation (A-1).

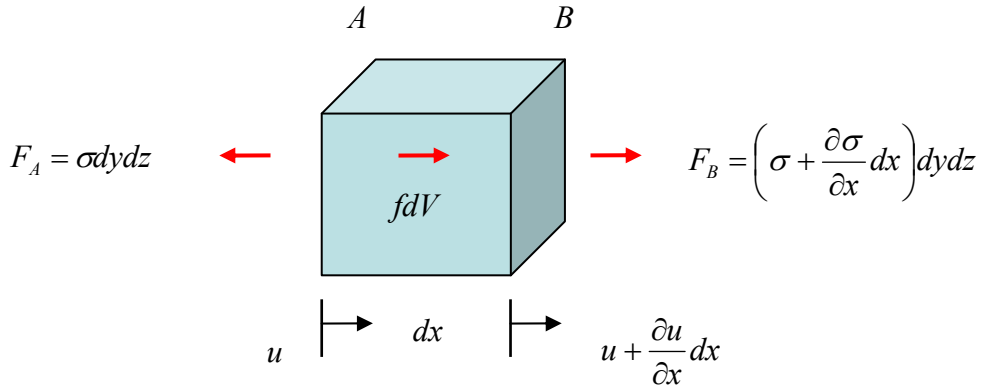

Figure A-1 Free body diagram for a finite cube

$$F_B\left(u+\frac{\partial u}{\partial x}dx\right)-F_A u \approx \frac{\partial u}{\partial x}\sigma dV + u\frac{\partial \sigma}{\partial x}dV = \varepsilon\sigma dV - ufdV \tag{A-1}$$

By integrating these finite cubes over the whole body, the total virtual work done by the surface traction T and body force f can be calculated by Equation (A-2).

$$\int_S T\cdot\delta u dS + \int_V \delta u\cdot f dV = \int_V \delta\varepsilon\cdot\sigma dV \tag{A-2}$$

where δu and $\delta\varepsilon$ are virtual displacement and strain

For cohesive zone based finite element model, as shown in Figure A-2, the total virtual work can be calculated by considering the displacement jump Δ across the cohesive surface, the stress tensor s and deformation gradient P and acceleration of the body, as shown in Equation (A-3).

$$\int_V s:\delta P dV - \int_{S_{\text{int}}} T\cdot\delta\Delta dS = \int_{S_{ext}} T\cdot\delta u dS - \int_V \rho\frac{\partial^2 u}{\partial t^2}\cdot dV \tag{A-3}$$

where P is the deformation gradient $\frac{\partial u}{\partial x}$, $A:B$ denotes $A^{ij}B_{ji}$, and s is the stress tensor, V, S_{ext} and S_{int} are the volume external surface area and internal cohesive surface area and internal cohesive surface area. The density of the material in the reference configuration is ρ, and T is the surface traction vector.

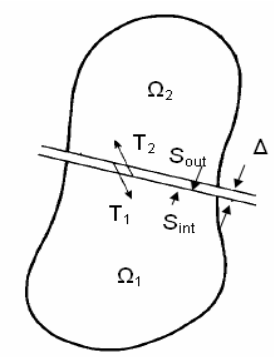

Figure A-2 Free body diagram with cohesive surfaces (Camacho et al., 1996)

The traction inside body can be calculated in the reference configuration with normal v based on stress tensor by Equation (A-4).

$$T = v \cdot s \tag{A-4}$$

The traction across the cohesive interface can be calculated by the cohesive energy ϕ and the corresponding displacement jump across the cohesive surface, as shown in Equation (A-5).

$$T = \frac{\partial \phi}{\partial \Delta} \tag{A-5}$$

As the fracture process is a transient process with dynamic nature, transient dynamic analysis or the time-history analysis is more suitable for the cohesive zone based finite element model for simulating the fracture process. This requires calculating the time varying displacements, velocities and accelerations at each time

step which can be used to calculate strains, stresses and force in the structure at each time step.

The basic equation for transient dynamic analysis is given by Equation (A-6). The transient dynamic analysis here mainly referred to dynamic process in the workpiece. The vibration of tool is not considered in this study.

$$[M][a]+[C][v]+[K][d]=[F] \tag{A-6}$$

where $[M]$, $[C]$, and $[K]$ is the global mass matrix, global damping matrix and global stiffness matrix. $[d]$, $[v]$ and $[a]$ denote the global displacement, velocity and acceleration arrays, and $[F]$ is the time dependent load vector

By writing Equation of (A-3) in an explicit integration form at time t:

$$Ma_{n+1} = F_{n+1}^{ext} - F_{n+1}^{\text{int}} \tag{A-7}$$

where M is the lumped mass matrix, a is the global acceleration vector and F_{n+1}^{int} is the internal force array arising from the current state of stress, and F_{n+1}^{ext} is the external force array including body force and surface traction.

The explicit second-order accurate central difference scheme can be used to discretize Equation (A-7) in time as shown in Equation (A-8). Based on this equation, the cohesive zone based finite element model can be used to simulate the dynamic

fracture process.

$$
\begin{aligned}
d_{n+1} &= d_n + \Delta t v_n + \frac{1}{2}\Delta t^2 a_n \\
a_{n+1} &= M^{-1}\left(F_{n+1}^{ext} - F_{n+1}^{\text{int}}\right) \\
v_{n+1} &= v_n + \frac{1}{2}\Delta t\left(a_{n+1} + a_n\right)
\end{aligned}
\tag{A-8}
$$

$$F_{N+1}^{ext} = \int_S N_S^T T dS \quad \text{for interface element}$$

$$F_{N+1}^{\text{int}} = \int_V B^T s dV \quad \text{for internal element}$$

where d, v and a denote the displacement, velocity and acceleration arrays, and B is the shape function

BIBLIOGRAPHY

BIBLIOGRAPHY

Barenblatt, G. I., "Mathematical Theory of Equilibrium Cracks", *Advances in Applied Mechanics, Academic Press*, pp. 55–125, 1962.

Bifano, T.G., Dow, T.A. and Scattergood, R.O., "Ductile-regime Grinding: A New Technology for Machining Brittle Materials", *Journal of Engineering for Industry, Transactions of the ASME*, vol. 113, no. 2, pp. 184-189, 1991.

Brinksmeier, E., Preuß, W. and Schmütz, J., "Manufacture of Microstructures by Ultrasonic Lapping", *13th Annual Meeting of the ASPE*, pp. 169-172, 1998.

Brinksmeier, E., Aurich, J.C., Govekar, E., Heinzel, C., Hoffmeister, H.-W., Klocke, F., Peters, J., Rentsch, R., Stephenson, D.J., Uhlmann, E., Weinert, K., Wittmann, M., "Advances in Modeling and Simulation of Grinding Processes", *CIRP Annals - Manufacturing Technology*, v55(2), pp. 667-696, 2006.

Burmeister, J.J., Pomerleau, F., Palmer, M., Day, B.K., Huettl, P., and Gerhardt, G.A., "Improved Ceramic-based Multisite Microelectrode for Rapid Measurements of L-glutamate in the CNS", *Journal of Neuroscience Methods*, pp. 163-171, 2002.

Byrne, G., Dornfeld, D., Inasaki, I., Ketteler, G., Konig, W., Teti, R., "Tool Condition Monitoring (TCM) - the Status of Research and Industrial Application", *CIRP Annals - Manufacturing Technology*, vol. 44, no. 2, pp. 541-567, 1995.

Cai, G.Q., Feng, B.F, Jin, T., Gong, Y.D, "Study on the friction coefficient in grinding", *Journal of Materials Processing Technology*, vol. 129, no. 1-3, pp 25-29, 2002.

Camacho, G.T., Ortiz, M. "Computational Modeling of Impact Damage in Brittle Materials", *International Journal of Solids and Structures*, vol. 33, no. 20-22, pp. 2899-2938, 1996.

Chen, W.K., Kuriyagawa, T., Huang, H. and Yosihara, N., "Machining of Micro Aspherical Mould Inserts", *Precision Engineering*, vol. 29, no.3, pp. 315-323, 2005.

Chen, X., Allanson, D.R., and Rowe, W.B., "Life Cycle Model of the Grinding Process", *Computers in Industry*, vol. 36, no.1-2, pp. 5-11, 1998.

Choi, Y., Narayanaswami, R., Chandra, A., "Tool Wear Monitoring in Ramp Cuts in End Milling Using the Wavelet Transform", *Intentional Journal of Advance Manufacture Technology*, vol. 23, pp. 419–428, 2004.

Denkena, B., Hoffmeister, H.-W., Reichstein, M. and Illenseer, S., "Process Development in Machining of Micro guideways", *Microsystem Technologies*, vol. 10, no. 3, pp 257-260, 2004.

De Borst, René, "Numerical Aspects of Cohesive-zone Models", *Engineering Fracture Mechanics*, vol. 70, no. 14, pp. 1743-1757, 2003.

Erdogan, E. "Fracture Mechanics", *International Journal of Solids and Structures*, vol. 27, pp. 171–183, 2000.

Espinosa, H.D., Zavattieri, P.D., "A Grain Level Model for the Study of Failure Initiation and Evolution in Polycrystalline Brittle Materials. Part I: Theory and Numerical Implementation", *Mechanics of Materials*, vol. 35, no. 3-6, pp. 333-364, 2003.

Espinosa, H.D., Zavattieri, P.D., "A Grain Level Model for the Study of Failure Initiation and Evolution in Polycrystalline Brittle Materials. Part II: Numerical Examples", *Mechanics of Materials*, vol. 35, no. 3-6, pp. 365-394, 2003.

Feng, J, Kim, B.S., Ni, J, "Modeling of ceramic Microgrinding by Cohesive zone Based finite element method", *Proceedings of the ASME 2009 International Manufacturing Science and Engineering Conference*, 2009.

Fraunhofer Institute for Ceramic Technologies and Systems, www.ikts.fraunhofer.de

Green, D.J., An Introduction to the Mechanical Properties of Ceramic, Cambridge, 1998.

Hakulinen, M., "Residual Strength of Ground Hot Isostatically Pressed Silicon Nitride", *Journal of Materials Science*, vol. 20, no. 3, pp. 1049-1060, 1985.

Hecker, R.L. and Liang, S.Y., "Predictive Modeling of Surface Roughness in Grinding", *International Journal of Machine Tools and Manufacture*, vol. 43, no. 8, pp. 755-761, 2003.

Hosokawa, A., Mashimo, K., Yamada, K., Ueda, T., "Evaluation of Grinding Wheel Surface by Means of Grinding Sound Discrimination", *JSME International Journal, Series C*, vol. 47, no. 1, pp. 52–58, 2004.

Hwang, T.W., Whitenton, E.P., Hsu, N.N., Blessing, G.V., Evans, C.J., "Acoustic Emission Monitoring of High Speed Grinding of Silicon Nitride", *Ultrasonics*, vol. 38, pp. 614–619, 2000.

Imasu, J., Fudouzi, H., Sakka, Y., "Micro-scale Patterning of Ceramic Colloidal Suspension by Micro Molding in Capillaries (MIMIC) with Assistance of Highly Infiltrating Liquid", *Journal of the Ceramic Society of Japan*, vol. 114, no. 1332, pp. 725-728, 2006.

Irwin G "Analysis of stresses and strains near the end of a crack traversing a plate", *Journal of Applied Mechanics*, vol. 24, pp. 361–364, 1957.

Griffith, A.A., “The Phenomena of Rupture and Flow in Solids”, *Philosophical Transactions of the Royal Society of London, Series A, Containing Papers of a Mathematical or Physical Character*, vol. 221, pp. 163-198, 1920.

Goller, M., Lutz, N. and Geiger, M., “Micromachining of Ceramics with Excimer Laser Radiation”, *Journal of the European Ceramic Society*, vol. 12, no. 4, pp. 315-321, 1993.

Karpuschewski, B., Wehmeier, M., Inasaki, I., “Grinding Monitoring System Based on Power and Acoustic Emission Sensors”, *CIRP Annals - Manufacturing Technology*, vol. 49, no. 1, pp. 235-240, 2000.

Kwak, J.-S., Ha, M.-K., “Detection of Dressing Time Using the Grinding Force Signal Based on the Discrete Wavelet Decomposition”, *International Journal of Advanced Manufacturing Technology*, vol. 23, pp. 87–92, 2004.

Law, S.S. , Wu, S.M., “Simulation Study of the Grinding Process”, *Transactions of the ASME. Series B, Journal of Engineering for Industry*, vol. 95, no. 4, pp. 972-978, 1973.

Lawn, B.R., Evans, A.G., Marshall, D.B., “Elastic/plastic Indentation Damage in Ceramics: The Median/radial Crack System”, *Journal of the American Ceramic Society*, vol. 63, no. 9-10, pp 574-581, 1980

Lawn, B.R., Evans, A.G., Marshall, D.B., “Elastic/plastic Indentation Damage in Ceramics: The Median/radial Crack System”, *Journal of the American Ceramic Society*, vol. 63, no. 9-10, pp 574-581, 1980.

Lezanski, P., “An Intelligent System for Grinding Wheel Condition Monitoring”, *Journal of Materials Processing Technology*, vol. 109, pp. 258–263, 2001.

Li, K., Fang, G..P., Liao, T. W., J.E. Jr. Mayer, “Effect of Wheel Wear in Grinding of Structural Ceramics”, *Technical Paper - Society of Manufacturing Engineers. MR*, pp. 4, 1996.

Li, K., Liao, T.W., O'Rourke, L. J., “Wear of diamond wheels in creep-feed grinding of ceramic materials. II. Effects on process responses and strength”, *Wear*, vol. 211, no. 1, pp. 104-112, 1997

Li, L., Fu, J., “Study of Grinding Force Mathematical Model”, *Annals of the CIRP*, vol. 29, no. 1, pp. 245-249, 1980.

Liao, T. W., Li, K., McSpaddenJr., S. B., “Wear Mechanisms of Diamond Abrasives During Transition and Steady Stages in Creep-feed Grinding of Structural Ceramics”, *Wear*, vol. 242, no. 1, pp. 28-37, 2000.

Liao, T. W., Li, K., McSpaddenJr., S. B., O'Rourke, L. J., “Wear of Diamond Wheels in Creep-feed Grinding of Ceramic Materials. *Wear*, vol. 211, no. 1, pp. 94-103, 1997.

Licht, V. , Ernst, E. and Huber, N., “Simulation of the Hertzian Contact Damage in Ceramics”, *Modeling and Simulation in Materials Science and Engineering*, vol. 11, no. 4, pp. 477-486, 2003.

Liu, Xianbing and Zhang, Bi, “Machining Simulation for Ceramics Based on Continuum Damage Mechanics”, *Journal of Manufacturing Science and Engineering, Transactions of the ASME*, vol. 124, no. 3, pp. 553-561, 2002.

Maksoud, T.M.A., Mokbel, A.A., Morgan, J.E., “Evaluation of Surface and Sub-surface Cracks of Ground Ceramic”, *Journal of Materials Processing Technology*, vol. 88, no. 1-3, pp 222-243, 1999.

Malkin, S., Hwang, T.W., “Grinding Mechanisms for Ceramics”, *CIRP Annals - Manufacturing Technology*, vol. 45, no. 2, pp. 569-580, 1996.

Malkin, S., Grinding Technology: Theory and Applications of Machining with Abrasives, 1989.

Marinescu, I. D., Tonshoff, H. K., Inasaki, I., Handbook of Ceramic Grinding and Polishing, William Andrew, 2000.

Marshall, D.B., Lawn, B.R., Evans, A.G., “Elastic/plastic Indentation Damage in Ceramics: the Lateral Crack System”, *Journal of the American Ceramic Society*, vol. 65, no. 11, pp 561-566, 1982.

Marshall, D.B., “Geometrical Effects in Elastic/plastic Indentation”, *Journal of the American Ceramic Society*, vol. 67, no. 1, pp 57-60, 1984.

MARUWA co., Ltd, www.maruwa-g.com

Nikumb, S.K. and Islam, M.U., “Laser Depth Controlled Precision Machining of Advanced Ceramics”, *Proceedings of the SPIE - The International Society for Optical Engineering*, vol. 2991, pp. 176-182, 1997.

Onikura, H., Inoue, R., Okuno, K. and Ohnishi, O., “Fabrication of Electroplated Micro Grinding Wheels and Manufacturing of Microstructures with Ultrasonic Vibration”, *Key Engineering Materials*, 238-239, pp. 9-14, 2003.

Ramesh, K., Huang, H., Yin, L. and Zhao, J., “Microgrinding of Deep Micro Grooves with High Table Reversal Speed”, *International Journal of Machine Tools and Manufacture*, vol. 44, no. 1, pp. 39-49, 2004.

Ren, C.Z., Guo, X.J., Yuan, L.W., "A Study on the Mechanism of the Electrolytic In-process Dressing (ELID) Grinding Using Molecular Dynamics (MD) and Finite Element (FE)", *Key Engineering Materials*, vol. 329, pp. 123-130, 2007.

Rice, J. R., "A Path Independent Integral and the Approximate Analysis of Strain Concentration by Notches and Cracks", *Journal of Applied Mechanics*, vol. 35, pp. 379-386, 1968.

Salmon, S.C., Modern Grinding Process Technology, McGraw-Hill, pp. 41, 1992.

Shaw, M. C., Principles of abrasive processing, Oxford Science Publication, New York, pp. 70–73, 1996.

Shet, C., Chandra, N., "Effect of the Shape of T-δ Cohesive Zone Curves on the Fracture Response", *Mechanics of Advanced Materials and Structures*, vol. 11, no.3, pp. 249-275, 2004.

Suresh, S., Shih, C.F., "Combined mode I-mode II and mode I-mode III fracture of brittle materials", *Scripta Metallurgica et Materialia*, vol. 25, no. 5, pp. 991-996, 1991.

Thomas, H.C., Mechanical Behavior of Materials, McGraw-Hill, pp.380-432, 2000.

Tonshoff, H.K., Peters, J., Inasaki, I., and Paul, T., "Modeling and Simulation of Grinding Processes", *CIRP Annals*, vol. 41, no. 2, pp. 677-688, 1992.

Vogler, Michael P., DeVor, Richard E., Kapoor, Shiv G., "Microstructure-level Force Prediction Model for Micro-Milling of Multi-phase Materials", *Journal of Manufacturing Science and Engineering, Transactions of the ASME*, vol. 125, no. 2, pp 202-209, 2003

Warner, D., Molinari, J., “Micromechanical Finite Element Modeling of Compressive Fracture in Confined Alumina Ceramic”, *Acta Materialia*, vol. 54, no. 19, pp. 5135-5145, 2006.

Wensink, H., Berenschot, J.W., Jansen, H.V. and Elwenspoek, M.C., “High Resolution Powder Blast Micromachining”, *Proceedings IEEE Thirteenth Annual International Conference on Micro Electro Mechanical Systems*, pp. 769-774, 2000.

Wu, Y.B., Fan, Y.F. and Kato, M., “A Feasibility Study of Microscale Fabrication by Ultrasonic-shoe Centerless Grinding”, *Precision Engineering*, vol. 30, no.2, pp. 201-210, 2006.

Yin, L., Jahanmir, S. and Ives, L.K., “Abrasive Machining of Porcelain and Zirconia with a Dental Handpiece”, *Wear*, vol. 255, no. 7-12, pp. 975-989, 2003.

Yoshikawa, H. and Sata, T, “Simulated Grinding Process by Monto-Carlo Method”, *CIRP Annals - Manufacturing Technology*, vol. 16, pp. 297-302, 1968.

Zarudi, I. and Zhang, C., “On the Limit of Surface Integrity of Alumina by Ductile-mode Grinding”, *Transactions of the ASME. Journal of Engineering Materials and Technology*, vol. 122, no. 1, pp. 129-134, 2000.

Zavattieri, P.D., Raghuram, P.V., Espinosa, H.D. “A Computational Model of Ceramic Microstructures Subjected to Multi-axial Dynamic Loading”, *Journal of the Mechanics and Physics of Solids*, vol. 49, no. 1, pp 27-68, 2001.

Zeng, D.W., Li, K., Yung, K.C., Chan, H.L.W., Choy, C.L., and Xie, C.S. “UV Laser Micromachining of Piezoelectric Ceramic Using a Pulsed Nd:YAG Laser”, *Applied Physics (Materials Science Processing)*, vol. 78, no.3 , pp. 415-421, 2004.

Zhang, B. and Howes, T. D., “Material-removal Mechanisms in Grinding Ceramics”, *CIRP Annals*, vol. 43, no. 1, pp. 305-308, 1994.

Zhang, B., “An Investigation of the Effect of Machine Loop Stiffness on Grinding of Ceramics”, *CIRP Annals - Manufacturing Technology*, vol. 50, no. 1, pp. 209-212, 2001.

Zhang, C., Ohmori, H., Li, W., “Small-hole Machining of Ceramic Material with Electrolytic Interval-dressing (ELID-II) grinding”, *Journal of Materials Processing Technology*, vol. 105, no. 3, pp. 284-293, 2000.

Zhang, C., Brinksmeier, E. and Rentsch, R., “Micro-USAL Technique for the Manufacture of High Quality Microstructures in Brittle Materials”, *Precision Engineering*, vol. 30, no. 4, pp. 362-372, 2006.

Zhang, C., Ohmori, H. and Li, W., “Small-hole Machining of Ceramic Material with Electrolytic Interval-dressing (ELID-II) grinding”, *Journal of Materials Processing Technology*, vol. 105, no. 3, pp. 284-293, 2000.

Zhang, C., Rentsch, R. and Brinksmeier, E., “Advances in Micro Ultrasonic Assisted Lapping of Microstructures in Hard-brittle Materials: A brief Review and Outlook”, *International Journal of Machine Tools and Manufacture*, vol. 45, no. 7-8, pp. 881-890, 2005.

Zhong, Z.W., “Ductile or Partial Ductile Mode Machining of Brittle Materials”, *International Journal of Advanced Manufacturing Technology*, vol. 21, no. 8, pp. 579-585, 2003.

Zhou, X. and Xi, F., “Modeling and Predicting Surface Roughness of the Grinding Process”, *International Journal of Machine Tools & Manufacture*, vol. 42, pp. 969-977, 2002.